TÉCNICO LISBOA

Mechanical Behaviour of friction stir butt welded joints under different loading and temperatures conditions

Lucas Rodrigues Pinto

Thesis to obtain the Master of Science Degree in

Mechanical Engineering

Supervisors: Prof. Virgínia Isabel Monteiro Nabais Infante
Prof. Catarina Isabel Silva Vidal

Examination Committee

Chairperson: Prof. Luís Filipe Galrão dos Reis
Supervisor: Prof. Virgínia Isabel Monteiro Nabais Infante
Members of the Committee: Prof. Miguel Araújo Machado
Dr. Gonçalo Filipe Pina Cipriano

November 2021

Aos meus pais e à Joana. Obrigado por estarem sempre a meu lado.

Agradecimentos

A realização deste trabalho não teria sido possível sem o auxílio e sem a contribuição de diversas pessoas. Como tal, gostaria de agradecer a todos aqueles que estiveram envolvidos, direta ou indiretamente no desenvolvimento desta tese, em especial:

À Professora Virgínia Infante, minha orientadora, pela confiança demonstrada nas minhas capacidades, toda a tutoria e apoio oferecido ao longo destes últimos meses, que tornaram possível conduzir este projeto a bom porto.

À Professora Catarina Vidal, da FCT NOVA, minha coorientadora, um sincero obrigado por todo o auxílio prestado no momento da realização dos ensaios não-destrutivos assim como ao tempo dedicado ao esclarecimento de todas as questões que me foram surgindo ao longo deste processo.

Ao Gonçalo Cipriano expresso também um profundo obrigado por toda ajuda prestada a nível da realização dos diversos cordões de soldadura, ensaios de tração e ensaios de fadiga. Agradeço ainda todos os conhecimentos e conselhos por ele partilhados que contribuíram em muito para a escrita e desenvolvimento desta tese.

Ao professor Miguel Machado, da FCT NOVA, agradeço todo o empenho e dedicação colocados na realização dos ensaios não-destrutivos assim como toda a sua disponibilidade para responder a qualquer dúvida relativa ao procedimento adotado e posterior análise de resultados.

Ao Senhor Daniel Jesus, do laboratório de caracterização de materiais do IST, agradeço toda a orientação no momento de lixar e polir amostras a fim de proceder à análise metalográfica das mesmas sob o microscópio ótico assim como pela facultação de todo o material necessário para poder realizar as tarefas supramencionadas.

Ao Senhor Pedro Teixeira e Senhor João Vicente, técnicos do LTO, agradeço todo o auxílio prestado na realização de todas as tarefas oficinais.

A todos os engenheiros do LENOF, agradeço a brevidade na produção dos provetes necessários para realização dos ensaios de tração e de fadiga assim como pela qualidade irrepreensível dos mesmos.

E por fim, mas não menos importante, numa nota mais pessoal, um enorme obrigado aos meus pais, sem os quais me seria impossível estar a escrever estas palavras, à Joana por ter sido o meu maior suporte nesta longa caminhada, assim como à Lara, Marcos e Renato por todo o apoio, amizade e companheirismo.

Abstract

Friction Stir Welding is a process that has led to an increase in the use of aluminum and its alloys in different industries, since, as an autogenous, solid-state welding process, it allows to obtain significantly lighter structures that benefit from the absence of melting of the base materials.

The work developed within the scope of this thesis was focused on the analysis of the mechanical behavior of AA7075-T651 friction stir butt welded joints, of 4 mm thickness, under different loading and temperature conditions.

A selection process was put into place in order to assure that appropriate welding parameters were being used to produce the welds from which fatigue specimens would be manufactured from.

The welds from which those specimens were manufactured from were submitted to non-destructive tests in order to assess the presence of welding defects.

Fatigue tests were carried out, under a constant amplitude loading regime, at two different stress ratios (0.05 and 0.5) and two different temperatures: 23 ºC and 150 ºC.

The results obtained by the fatigue tests point to a higher fatigue life of the specimens when the highest stress ratio was employed (for the maximum stress applied) for both loading temperatures.

Regarding the stress range, the contrary was found to be true: the lower stress ratio resulted in a higher fatigue life.

Room temperature was also found to result in a significantly better fatigue performance.

A Scanning Electron Microscope was used in order to characterize the fatigue fracture surfaces.

Keywords

Friction Stir Welding; Fatigue Testing; Stress Ratio; Temperature; AA7075-T651

Resumo

O processo de Soldadura por Fricção Linear tem permitido um aumento do número de possíveis aplicações para o alumínio e as suas ligas, uma vez que, sendo um processo de soldadura autogéneo e que decorre no estado sólido, permite obter estruturas mais leves e que beneficiam da ausência de fusão dos materiais de base.

O trabalho desenvolvido no âmbito desta tese focou-se na análise do comportamento mecânico de juntas topo a topo de AA7075-T651, com 4 mm de espessura, sob diferentes condições de carregamento e de temperatura.

Foi estabelecido um processo de seleção para assegurar que um conjunto adequado de parâmetros de soldadura seria utilizado para produzir os cordões a partir dos quais seriam manufaturados os provetes de fadiga.

Esses cordões foram submetidos a ensaios não-destrutivos de forma a avaliar a presença de defeitos.

Os ensaios de fadiga foram realizados sob um regime de amplitude de tensão constante, utilizando-se 2 razões de tensões (0.05 e 0.5) e 2 temperaturas distintas: 23 ºC e 150 ºC.

Os resultados obtidos da realização dos ensaios de fadiga apontam para uma maior vida à fadiga dos provetes quando aplicada a maior razão de tensões (considerando a tensão máxima dos ensaios) para as duas temperaturas.

O contrário foi verificado quando considerada a gama de tensão: a menor razão de tensões resultou em uma maior vida à fadiga.

Observou-se também que a temperatura ambiente resultou num desempenho, em fadiga, significativamente superior.

Um Microscópio Eletrónico de Varrimento foi utilizado de forma a caracterizar as superfícies de fratura de fadiga.

Palavras-Chave

Soldadura por Fricção Linear; Fadiga; Razão de Tensões; Temperatura; AA7075-T651

Contents

List of Figures

List of Tables

Abbreviations and Symbols

α	FSW Tool Tilt Angle
ΔK	Stress Intensity Factor Range
$\Delta\sigma$	Stress Range
σ_a	Stress Amplitude
σ_m	Mean Stress
σ_{max}	Maximum Stress
σ_{min}	Minimum Stress
Ω	Tool Rotational Speed
a	Crack length
AA	Aluminium Alloy
AS	Advancing Side
BM	Base Material
DXZ	Dynamically Recrystallized Zone
DEMI	Departamento de Engenharia Mecânica e Industrial
EBW	Electron Beam Welding
EDS	Energy Dispersive Spectroscopy
EU	European Union
EV	Electric Vehicle
FCT	Faculdade de Ciências e Tecnologia
FSW	Friction Stir Welding
H_2O	Water
HAZ	Heat Affected Zone
HCl	Hydrochloric Acid
HF	Hydrofluoric Acid
HNO_3	Nitric Acid
ISO	International Organization for Standardization
IST	Instituto Superior Técnico
LBW	Laser Beam Welding
LTO	Laboratório de Técnicas Oficinais
MIG	Metal Inert Gas
N	Number of cycles
NDT	Non-Destructive Testing
NOF	Núcleo de Oficinas
R	Stress Ratio
RS	Retreating Side
SEM	Scanning Electron Microscope
SMAW	Shield Metal Arc Welding

SZ	Stir Zone
TIG	Tungsten Inert Gas
TMAZ	Thermo-Mechanically Affected Zone
TWI	The Welding Institute
UTS	Ultimate Tensile Strength
v	Tool travel speed

Chapter 1

Introduction

The first chapter intends to give a brief overview of this thesis dissertation. The scope and motivations of the work that was developed are brought up and the structure of the entire dissertation is presented, with the content of each one of its chapters being briefly summarized.

1.1. Scope

Aluminum and its alloys have seen their applications in multiple industries increase over the last years as a result of the emergence and development of a joining process that allows to obtain aluminum welds with excellent mechanical properties: Friction Stir Welding (FSW).
FSW is a solid-state welding process during which melting of the base material does not occur which allows aluminum alloys that were considered to be difficult to weld, to be welded.

As for its working principle, a non-consumable, rotating, hardened steel tool, with a cylindrical shape constituted by a pin and a shoulder, is driven into the weld joint until the pin has completely penetrated the joint and the shoulder is in contact with the surface of the workpieces. Then, the tool is traversed along the joint line, at a constant transverse speed (welding/travel speed).

Additionally, since it is an autogenous welding process, no filler material is required in order to achieve the joining of the materials thus, it is possible to obtain lighter structural parts, which is of special interest for the aerospace and automotive industries, due to the possibility of reducing fuel consumptions. Moreover, lighter structural parts lead to lower emissions, which is important taking into account that the transport industry is accountable of 25% of EU's total greenhouse gas emissions [1].
Current efforts are being made in order to move towards a more sustainable form of mobility, as established by the EU's Green Deal (a growing strategy that aims among other things (Figure 1.1), to reduce the emissions of the transport industry, by 90%, by the year of 2050) and EU's Horizon Europe funding program that addresses climate changes with one of its pillars focusing in mobility [1], [2].
Therefore, taking into account the previously mentioned properties of the FSW process, it may play an important role in EU's mission.

The majority of structural parts must undergo fluctuating loads, dynamic loads (loads that vary with time) therefore, fatigue failure is of major interest as it is the most probable failure mechanism.

In fact, fracture induced by fatigue is the principal cause of failure in joints obtained by means of FSW [3].

The loading temperature and stress ratio (R), which indicates the ratio between the minimum and maximum stress applied, are some of the factors that influence the fatigue crack growth rate and consequently play an important role in the fatigue performance of the welds.

Taking that into account, the work developed within the scope of this thesis will focus in evaluating the impact of different loading and temperature conditions over joints obtained by means of FSW.

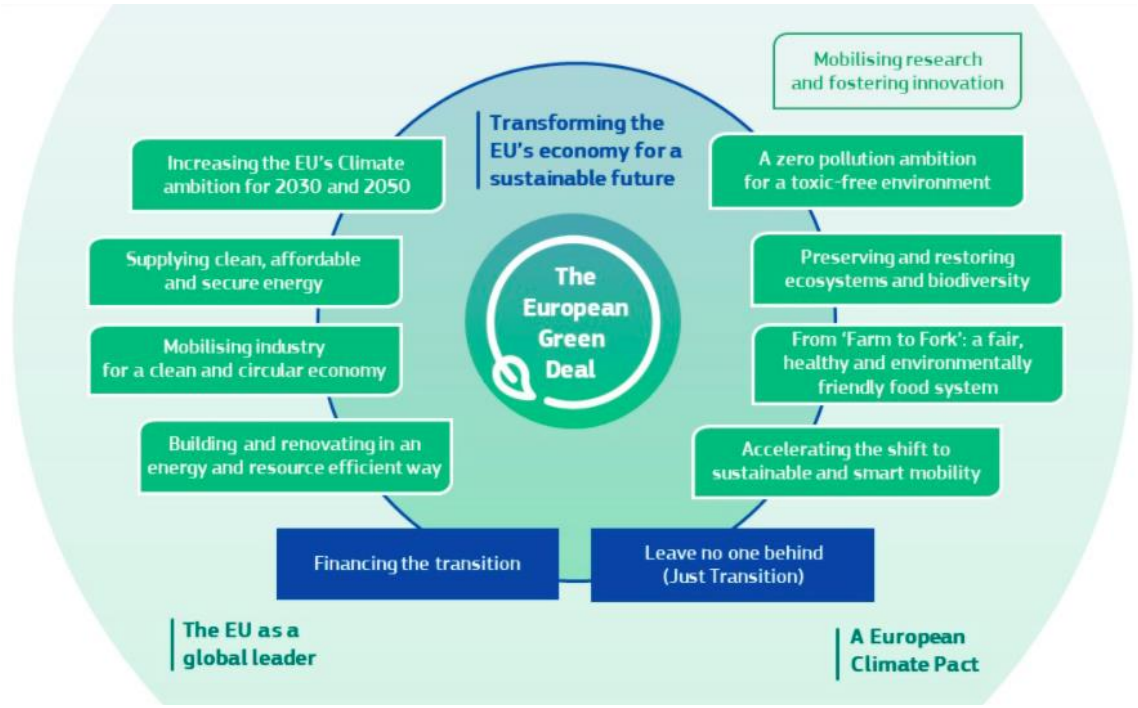

Figure 1.1- Elements of the EU's Green Deal [1].

1.2. Objectives

The main objective that was established for this thesis was to evaluate the mechanical behavior of friction stir butt welded joints under different loading and temperature conditions.

In order to accomplish that, the following objectives, that need to be achieved, were outlined:

- Establish a selection process that would allow to select appropriate welding parameters, in order to produce the required welds, taking into account the base material being used and the thickness of the plates being welded.
- Characterize, through the use of non-destructive tests (Eddy Current Testing), the welds that were produced.
- Characterize the welds through the use of destructive techniques such as metallographic analysis, hardness testing and uniaxial quasi-static tensile testing.
- Examine the effect of welding defects (that were detected during the execution of non-destructive tests) over the microstructure and hardness profile of the welds.
- Perform fatigue tests under different loading ($R = 0.05$ and $R = 0.5$) and temperature (room temperature and 150 ºC) conditions and access the impact of this conditions over the fatigue performance of the fatigue specimens.
- Evaluate the fatigue fracture surface of the specimens.

1.3. Structure of Thesis

This dissertation is divided in 5 different chapters, including this one, which main goal is to expose the scope and objectives of the experimental work that was developed, as well, as previously mentioned, introducing the different chapters that make up this dissertation.

In the second chapter, State of the Art, the results of the bibliographic research that was carried out are reported. Chapter 2 is divided in 3 main sections. Along the first one, an introduction to aluminum and its alloys is made. Some of the topics covered include an analysis of the classification system used for this type of material and aluminum weldability problems. In the following section, different matters related to FSW are explored such as: the working principles, the temperature distribution and peak temperature reached during the production of FS welds, the process parameters and correspondent effect on the resulting welded joints. The third and last section of this chapter is related to a well-known failure mechanism: fatigue. Fatigue's basic concepts are presented as well as the fatigue properties of friction stir welds.

Chapter 3, Materials and Methods, is divided in 7 sections, through which the mechanical and metallographic characterization of the base material used in the experimental work (AA7075-T651) is carried out, all the equipment used in order to produce the required friction stir welds is presented, the selection process that was followed in order to determine the appropriate welding parameters is thoroughly reported and so are the procedures followed to execute the desired inspections and mechanical tests.

Chapter 4, one of the most relevant ones, Results and Analysis, is divided into seven sections, each one being dedicated to presenting and discussing the results obtained from the different analysis that were carried out, which include, in order of appearance, the metallographic examination of the welds, hardness testing, uniaxial quasi-static tensile testing, fracture surface analysis of tensile specimens, fatigue testing, fatigue fracture surface analysis and lastly, fatigue fracture surface characterization by SEM.

In the fifth and last chapter of this dissertation, the most relevant results obtained throughout the execution of the experimental work are summarized and final conclusions are established.
Future work developments proposals can also be found in Chapter 5.

Chapter 2

State of the Art

The present chapter aims to provide a comprehensive overview of the FSW process and its fundamentals, as well as introducing diverse topics of high relevance regarding the experimental work that was developed within the scope of the thesis. In order to do so, a literature review was performed for a more in-depth analysis and relevant works developed by other authors are cited whenever possible with the purpose of illustrating, with concrete examples, the subjects being addressed. In conclusion, the current state of the art concerning the scope of the work is presented.

2.1. Aluminum Alloys

2.1.1. Historical context and Properties

Although being the most abundant metallic element of Earth's crust, accounting for approximately 8% of its weight and only surpassed by oxygen and silicon, aluminum does not occur in its metallic form in nature, due to its chemical properties. Nevertheless, those chemical properties are the reason why it is possible to combine aluminum with other elements, obtaining in this way, the different aluminum alloys that have been developed over the last years and that are widely used nowadays [4].

The name aluminum was attributed by Humphry Davy in the early 1800s, who discovered that aluminum might potentially be produced by electrolytic reduction (from alumina, an aluminum oxide, Al_2O_3). However, Humphry was not capable to isolate aluminum from his experiments [5].

Hans Christian Ørsted was capable to put into practice the theory of Humphry and in 1825 was capable to produce aluminum (what was really produced was an aluminum-potassium alloy). The first time that pure aluminum was produced was in 1827, by Friedrich Wöhler, which carried out the work developed by Ørsted. However, the quantity of aluminum that was produced in these experiments and others, later developed by Wöhler, was very low, consequently making it rare. At that time, aluminum was considered to be an elite material, used mainly in luxury items and its price even surpassed gold's. The transition to the industrial production of aluminum was made possible by Henri Étienne Sainte-Claire Deville, in 1854, due to its efforts to improve the process developed by Wöhler [5].

Charles Hall and Paul Héroult found that by the reduction of alumina, melted in cryolite, aluminum could be produced in a more cost-effective way, which lead to a decrease in the aluminum price and an increase in its production. Nowadays, this process is still used in the aluminum production process along with the Bayer process, that applied to bauxite allows alumina to be extracted from it. Bauxite is a clayey rock, highly rich in alumina, that was discovered in 1821, by Pierre Berthier. The name derives from the French city in which it was discovered: Les Baux [5], [6].

Aluminum is fully recyclable and can be recycled many times without any pernicious effects over its mechanical properties. It is a non-magnetic material (making it suitable for electrical applications such as electrical shielding and magnetic housing), non-toxic (making it appropriate to be used, for example, in kitchen appliances and utensils), a good reflector (thus used in reflectors such as rescue blankets), a good sound absorber, lightweight, with a density that is roughly one third of the one presented by steel (good strength to weight ratio), corrosion resistant (due to its high affinity with oxygen, aluminum is prone to form an oxide layer, that works as a protective layer, avoiding further damage to surfaces), and an excellent heat and electricity conductor (leading to its use in applications such as power transmission lines)
It is a very ductile, malleable and easily machined material with an UTS ranging from 80 to 572 MPa, depending on the type of alloy considered [7].

The classification system employed for aluminum alloys is explained in the next section of this dissertation.

2.1.2. Alloys Classification

Aluminum alloys are divided in two main categories: wrought aluminum alloys and cast aluminum alloys. Only the former will be addressed in detail in the course of this chapter. Both these types of aluminum alloys can be subdivided, into two categories, taking into consideration the strengthening process. As a result, aluminum alloys are furtherly categorized as heat-treatable or non-heat-treatable.

Regarding the classification system employed for wrought aluminum alloys, four digits are used, as established by the International Alloy Designation System. The first digit refers to the alloy group. It indicates the primary alloying element which has been added. Alloys with the same first digit are said to be part of the same series.

For example, the 7075 aluminum alloy, which was used as base material in the experimental work carried out in the scope of this thesis, is part of the 7XXX series. The 7XXX series encompasses all the aluminum alloys that that have as main alloying element zinc. The second digit indicates modifications made to the original alloy or impurity limits. The last 2 digits (third and fourth) are used to identify a specific alloy within a certain series or indicate the aluminum purity.

Wrought aluminum alloys, as mentioned before, can be classified considering their strengthening process. The strength of the alloys is initially set by alloying aluminum with different elements. The non-heat-treatable alloys improved strength is a result of a process designated by strain

hardening (a process through which the strength of the material is improved by means of plastic deformation) while the heat-treatable alloys can be furtherly strengthened by thermal treatments.

Table 2.1 summarizes the different wrought aluminum alloys series, that are defined taking into account their primary alloying element. The strengthening process of each series is also indicated. The designation of a wrought aluminum alloy can be extended by the use of a series of letters and numbers that are part of the temper designation system.

The temper designation follows the alloy designation (which was described previously), separated by a hyphen, and its use has the purpose of indicating the treatment that the respective alloy has undergone. The basic temper designations are outlined in Table 2.2.

Table 2.1- Aluminum alloys series categorized by alloying element and strengthening process [7].

Series	Primary alloying element	Strengthening Process
1xxx	Unalloyed (99% Al)	Non- Heat-Treatable
2xxx	Copper	Heat-Treatable
3xxx	Manganese	Non- Heat-Treatable
4xxx	Silicon	Heat-Treatable and Non-Heat-Treatable
5xxx	Magnesium	Non-Heat-Treatable
6xxx	Magnesium, Silicon	Heat-Treatable
7xxx	Zinc	Heat-Treatable
8xxx	Other elements	Heat-Treatable and Non-Heat-Treatable
9xxx	Unused series	-

Table 2.2- Basic tempers designation system for aluminum alloys [7].

Designation	Meaning
F	As fabricated. No control over the strain hardening or thermal conditions.
O	Annealed. Treatment that allows to obtain the best ductility and lowest strength temper.
H	Strain Hardened. The strain hardening process can be followed by supplementary thermal treatment that leads to a strength reduction. The H is always followed by two or more digits which meaning is explained in Table 2.3.
W	Solution Heat-Treated. Only applicable to alloys that have aged spontaneously at room temperature after solution heat-treatment.
T	Thermally Treated. Treatment used to obtain stable tempers other than F, O or H. The T is always followed by one or more digits, which meaning is explained in Table 2.4.

Table 2.3- Strain-hardening designation system for aluminum alloys [7].

First digit after the H indicates a basic operation	
Designation	**Meaning**
H1	Only strain hardened.
H2	Strain hardened and partially annealed.
H3	Strain Hardened and Stabilized by low temperature treatment
H4	Strain hardened and Lacquered or Painted
Second digit after the H indicates the degree of strain hardening	
Designation	**Meaning**
HX2	Quarter Hard
HX4	Half Hard
HX6	Three-Quarters Hard
HX8	Full Hard
HX9	Extra Hard

A third digit can be used in order to identify some eventual changes that are made in the treatments that are represented by the two previous digits. In that scenario the designation assumes the following form: Hxyz with x, y and z being digits.

Table 2.4- Thermal treatment designation system for aluminum alloys [7].

Designation	Meaning
T1	Naturally aged after cooling from an elevated temperature shaping process to a stable condition.
T2	Cold worked after cooling from an elevated temperature shaping process to a stable condition and then naturally aged.
T3	Solution heat treated followed by cold work and then naturally aged to a stable condition.
T4	Solution heat treated followed by natural aging to a reasonable stable state.
T5	Artificially aged after cooling from an elevated temperature shaping process.
T6	Solution heat treated followed by artificial aging.
T7	Solution heat treated followed by stabilization (overaged).
T8	Solution heat treated followed by cold work and then artificially aged.
T9	Solution heat treated followed artificial aging and then cold worked.
T10	Cold worked after cooling from an elevated temperature shaping process and then artificially aged.

Additional digits can be added following the designation presented in Table 2.4, in order to indicate some difference from the treatments described. For example, additional digits can be used to indicate stress relief: TX52 or TXX52, which indicates that following the treatment X/XX a process of stress relieving, by compressing, was carried out.

2.1.3. Aluminum Weldability

Aluminum is the most abundant metallic element on Earth and became an economic competitor in engineering applications by the end of the 19th century.

It is one of the most welded metals worldwide (second to steel), which can be justified by the fact that it combines good mechanical properties with availability, low price and low weight.

As mentioned previously, one mechanical property that characterizes this material is its high electrical conductivity. This property can be an inconvenient in the selection of a fusion welding process since, as a result, only processes that have high welding speeds and can deliver high energy inputs are suitable. Only a few of these processes meet the aforementioned requirements, being the most used the TIG (Tungsten Inert Gas) and MIG (Metal Inert Gas) processes.

Before the TIG and MIG processes were developed, fusion welding aluminum alloys was mainly restricted to the Shielded Metal Arc Welding (SMAW) process and the results were not very satisfying.

The TIG process was developed in the early 1940's and is still widely used to weld aluminum alloys nowadays. The development of this process allowed aluminum to be considered in applications that required welds of high quality to be used in critical applications, such as cryogenic pressure vessels.

The TIG process was developed earlier than the MIG process (first patented in the USA in 1949 [8]) and a transition to the latter occurred, as it was developed, for many applications, essentially due to the increased welding speed and deposition rates (of filler material) that it offered comparatively to the former, thus increasing productivity.

Welding aluminum alloys by means of fusion welding processes can also be a challenging task due to the defects that may arise. The most characteristic defects that may arise as a result of the use of such type of joining processes to weld aluminum and its alloys are solidification cracking, porosity, inclusions, softening of the heat-affected zone (HAZ) and poor weld bead profile.

Solidification cracking, also known as hot cracking, is an inter-dendritic type of cracking. It is related to the formation of cracks during the process of solidification of the weld. It is a result of high residual stresses (which are a result of the aluminum high thermal conductivity) and the presence of low melting point phases in inter-dendritic regions of the solidifying weld. Minimization is possible through the use of ductile filler materials or by planning the weld sequence in order to reduce the residual stresses. Another crack-related imperfection that may arise is liquation cracking: it occurs in the HAZ when low melting point films are formed at the grain boundaries. Heat-treatable alloys are more susceptible to this type of defect.

Concerning porosity, the most frequent form of porosities encountered are hydrogen induced. The main cause behind this type of defect is the absorption of hydrogen by the weld pool. The presence of hydrogen can be a result of improper surface cleaning (hydrocarbons and moisture from contaminants on the base material), moisture in the electrode, or even the presence of hydrogen in the shielding gas atmosphere.

Regarding inclusions, an inclusion can be described as any undesired foreign element present in the weld. The most common type of inclusion is a result of the high affinity of aluminum with

oxygen. As it reacts with oxygen, instantly the formation of an adherent oxide layer, alumina (which has a higher melting point than aluminum and is insoluble in solid and liquid aluminum) occurs. This oxide layer must be destroyed during the welding process. If it gets trapped in the weld bead, alumina inclusions will act as stress concentration points. The necessity of these layer to be eliminated, leads to higher heat affected zones and higher welding pools, which can also be problematic.

The softening of the HAZ always occurs, independently of the type of aluminum alloy that is being welded. This softening disrupts the improved mechanical properties of the alloys but is more severe for alloys that have their mechanical properties improved by means of work hardening (strain-hardened aluminum alloys). Low heat inputs can minimize this loss of mechanical properties as annealing is reduced.

Lastly, the poor weld bead profile can occur due to the high thermal conductivity of aluminum alloys. Obtaining a weld bead profile that is acceptable is possible by using appropriate welding parameters.

Overall, the quality of aluminum welds is highly dependent in the use of the correct welding parameters/process, operator capability (if the weld is done manually), filler material, pre/post welding treatment procedures and surfaces preparation. Although the arrival and development of the MIG process allowed aluminum alloys to be welded with higher quality, precision and speed, it still remains a fusion welding process and therefore some of the addressed defects may still appear.

In the past, some aluminum grades have commonly been considered as non-weldable (or at least not recommended to join through this type of processes, as for example the 7XXX series), since they were more prone to the formation of welding defects which presence resulted in unacceptable welds from either a mechanical or even an aesthetic point of view.

Nowadays, the Friction Stir Welding (FSW) process is seen as a solution to obtain aluminum welds of higher quality and with high repeatability while also allowing those aluminum grades to be easily welded. FSW is a solid-state welding process, meaning that the materials do not undergo fusion during the joining operation, as a result of the lower energy inputs used. Therefore, fusion welding characteristic defects' do not arise.

As mentioned previously, aluminum and aluminum alloys are materials with high thermal conductivities. When welding, this mechanical property can lead to the distortion of the workpieces. Since FSW uses lower energy inputs comparatively to fusion welding processes, lower residual stresses are registered in friction stir welds and consequently lower degrees of distortion of the workpieces are observed. As a consequence, the range of applications for aluminum and its alloys has increased, with the introduction and development of the FSW process.

2.2. Friction Stir Welding

2.2.1. FSW Process Fundamentals

Friction welding covers solid-state welding processes that lead to the joining of materials under the influence of heat generated by the mechanically sliding motion between surfaces (mechanical friction), which causes the material to plastically deform.
The friction welding process most commonly used in order to weld aluminum alloys is known as Friction Stir Welding (FSW).

FSW was conceived and patented by TWI (The Welding Institute), at Cambridge, in the United Kingdom, in 1991 [9]. It is an autogenous process, as it does not require the use of any type of filler material.

As for the working principle, a non-consumable, rotating, hardened steel tool, with a cylindrical shape constituted by a pin (also designated in the literature as probe) and a shoulder, is driven into the weld joint until the pin has completely penetrated the joint and the shoulder is in contact with the surface of the workpieces. Then, the tool is traversed along the joint line, at constant transverse speed (welding/travel speed).

The rotating tool generates enough heat (by interfacial and internal friction dissipation) and plastic deformation to weld the workpieces together (the tool is responsible for mechanically mixing and joining the workpieces). The major component of the heat generated results from the contact of the workpieces with the tool shoulder. As the tool moves along the weld line, the material is stirred by the pin being moved from the front of the tool into the trailing edge, where it is posteriorly forged, and the weld is then obtained.

Figure 2.1 shows a schematic illustration of the FSW process. From Figure 2.1 it is possible to notice that the weld can be divided into two different zones: the advancing side of the weld (AS), which corresponds to the half of the weld where the rotational direction of the tool is coincident with the welding direction and the retreating side of the weld (RS), where the welding direction is opposite to the tool's rotational direction.

The workpieces are clamped in order to avoid any spread or lift during the welding process. The different joint configurations that can be employed with the FSW process are presented in Figure 2.2. For both butt and lap joints there is no need for significant joint and surface preparation procedures'.

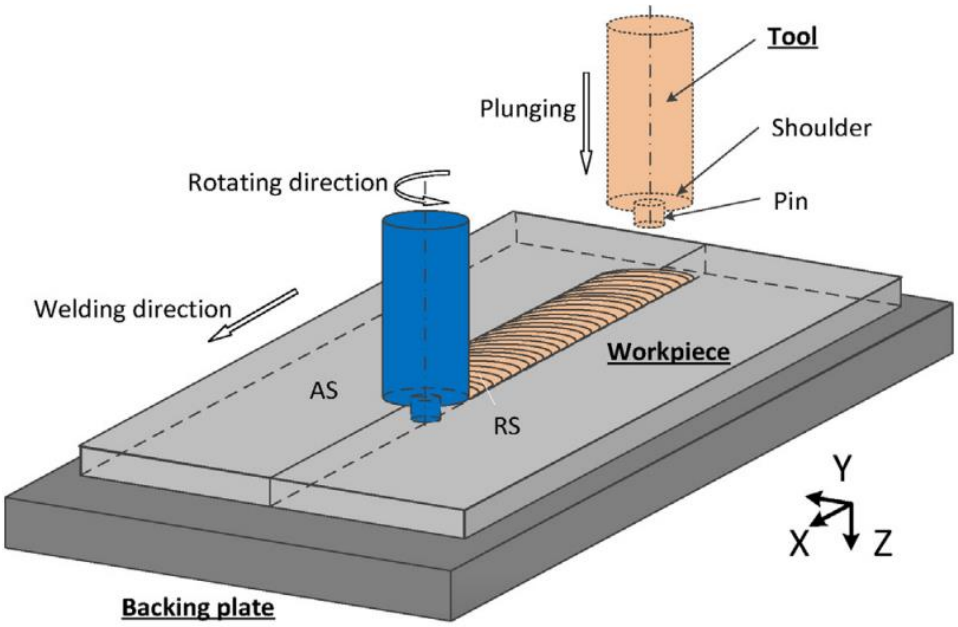

Figure 2.1- Schematic illustration of the FSW process.

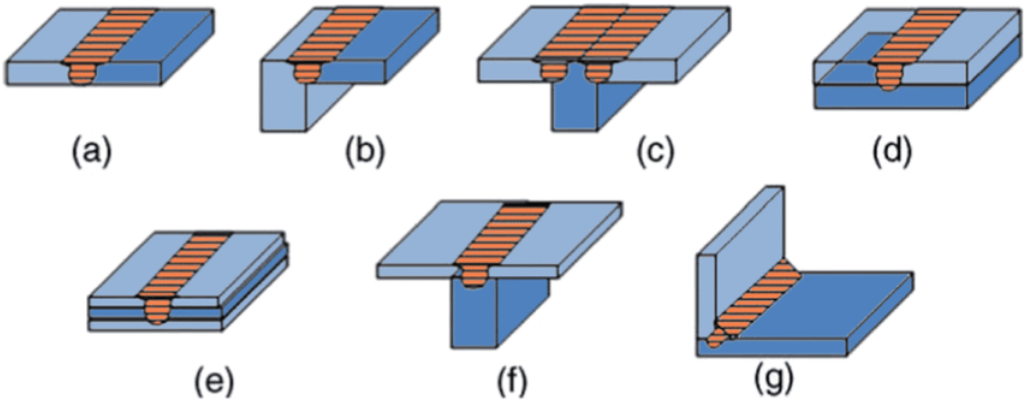

Figure 2.2- Some of the possible joint configurations to be used with FSW: a) square butt, b) edge butt, c) T butt joint, d) lap joint, e) multiple lap joint, f) T lap joint, g) fillet joint [10].

The FSW process can be divided into four main stages which are represented in Figure 2.3 and described in more detail next.

- Plunging: The first stage of the welding process consists in pressing the tool pin against the workpieces until the shoulder is also in contact with them.
- Dwelling: Following the plunging phase, the tool position remains the same as the temperature increases until the appropriate welding temperature is reached.
  At that moment the part of the process in which the workpieces are indeed welded can begin. This stage of the process allows both the temperature and material flow profiles to become uniform.

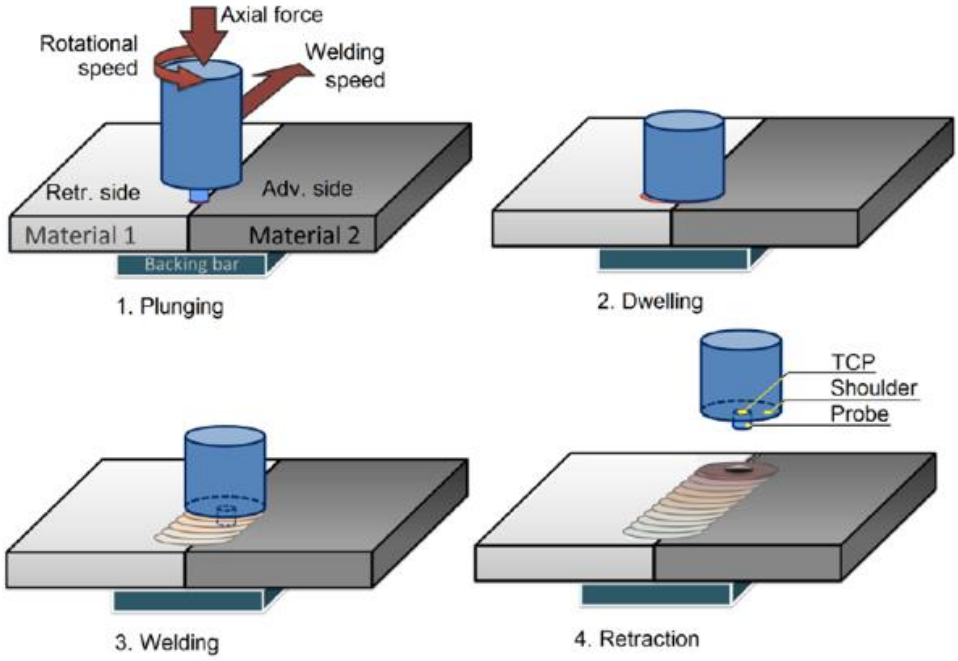

Figure 2.3- Representation of the FSW process main stages [11].

- Welding: As mentioned previously when the desired welding temperature is reached the welding starts. The rotation of the tool is combined with a transverse movement along the joint line and the weld is created.
- Retraction: In order to conclude the FSW process, the welding tool must be removed. The retraction stage consists in a complete removal of the pin from the weld joint. Depending on the tool design, an exit hole may be left on the workpiece.
  To avoid obtaining a final workpiece with an exit hole, two options emerge: using run off plates or machining the workpiece in order to remove the exit hole.

A good understanding of the material flow during the FSW process is critical in order to obtain/select optimal tool designs, selecting appropriate welding parameters and thus controlling the quality of the welds. Taking this into account, different methods have been employed in order to evaluate the material flow characteristics. An example of a technique that is used for this purpose is the tracer by marker technique in which a certain material, that is different from the one that is going to be welded, is used as a form to track the material flow. Finite element formulations are also employed to accurately trace the material flow throughout the FSW process [12].
Nevertheless, the material flow in FSW remains a complex matter that will not be approached in further detail as it falls out of the scope of the present work.

Another important aspect of the FSW process is related to, as mentioned previously, the fact that it is a solid-state welding process. This is a result of the peak temperature reached during the

operation. A brief introduction to the temperature distribution in welds obtained by FSW is presented next.

2.2.2. FSW Temperature Distribution

Understanding the temperature distribution in welds obtained by friction stir welding is important, since it has a direct impact in the microstructure of the weld (a topic that is covered later on, in the present chapter) thus impacting the resulting mechanical properties of the welded joint.

In order to evaluate the temperature distribution of this welds, there is a need to take temperature measurements during the welding process. Usually, temperature sensors such as thermocouples are used for that effect. Another method consists in the evaluation of the microstructure of the different weld regions (Section 2.2.4) since taking into account the microstructural changes that the material undergoes during the welding process, the temperature distribution can be inferred.

The maximum temperature reached during the FSW process was found to be within the interval of 70 to 90% of the melting temperature, for a wide range of aluminum alloys [12] as a result of the energy input of the process. As a consequence, and as explained previously, the base materials do not meld when joined through FSW therefore, comparatively to conventional fusion welding processes it is possible to obtain welds with lower distortions and residual stresses as a direct result of the lower energy inputs.

Verma et al. [13] collected data on the available literature regarding previous works that were developed concerning the temperature distribution in friction stir welds and thermal modeling of FSW. One of the conclusions that was withdrawn is that, as observed by many researchers, the temperature distribution is not symmetric: the temperatures attained in the retreating side of the weld are lower comparatively to the ones obtained in the advancing side of the weld. The same observation was made during the experiments carried out by Verma et al. [13], who, aimed to analyze the temperature distribution of welds obtained by FSW, in AA6082 plates with a thickness of 6.35 mm.

Tang et al. [14] were able to register the temperature distribution on friction stir welds made of AA6061-T6. One of the motivations of the work was to investigate not only the way that the temperature varied respectively to the distance to the weld center but also the temperature distribution behavior as a function of the distance to the top surface of the weld. For this purpose, holes were made in the plates that were going to be welded (which had a thickness of 10 mm) across 3 different horizontal lines located at 1.59, 3.18 and 4.76 mm from their top surfaces.

The results obtained for a certain value of the tool rotational and transversal speed are shown in Figure 2.4 (400 rev/min and 120 mm/min respectively).

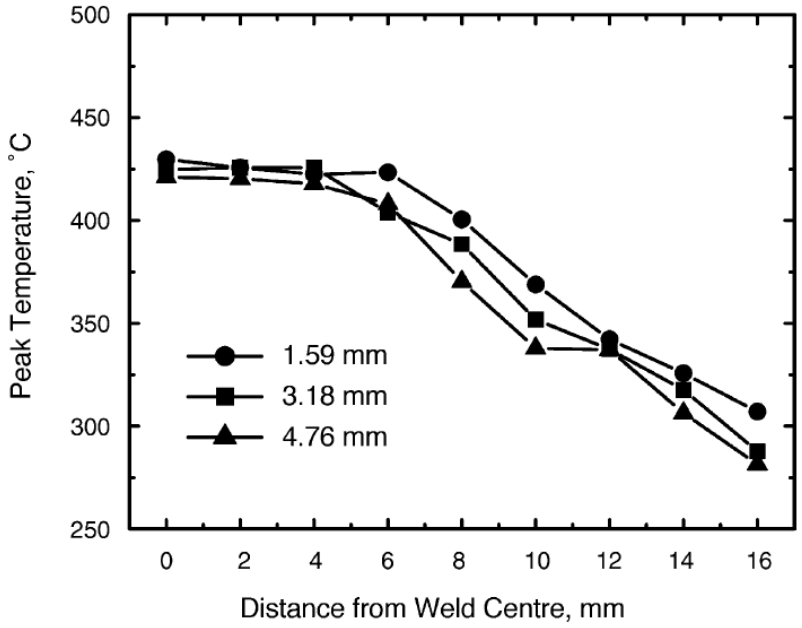

Figure 2.4- Variation of the peak temperature relatively to the distance to the weld center and the depth effect in AA6061-T6 joints obtained by FSW [12].

Figure 2.4 shows that for each line, the respective peak temperature was reached at the weld center and remained approximately constant up to approximately 5 mm. From there, the temperatures decreased as the distance to the weld center increased.

Regarding the temperature profile along the different distances to the top surface of the weld (depth effect over the temperature distribution), it is possible to notice that the variation of the peak temperature reached during the welding process with the distance to the top surface of the weld is not very significant for the regions closer to the center. For the adjacent areas, the depth effect becomes noticeable (a maximum variation of 40 ºC was registered) with the highest temperatures being registered closer to the top surface of the welds.

Experiments were also conducted in the same work in order to evaluate the effect of the tool rotational speed in the temperature distribution. From their research, Tang et al. [14] were able to conclude that the peak temperature reached during the weld varies with the tool rotational speed in the following manner: increased tool rotational speeds lead to higher peak temperatures. However, it was observed that the transversal speed of the tool had a different impact in the peak temperature: higher transversal speeds, lead to lower maximum temperatures. This effect of both the tool rotational and travel speeds is related with the impact that these process parameters have in the heat generated during the FSW process.

Other process parameters should also be taken into account regarding this matter. Considering the fact that the temperature distribution, as mentioned previously in this section, has an impact in the mechanical properties of the welded joint, it is very important that those process parameters are correctly set.

2.2.3. FSW Process Parameters

Some of the most pertinent process parameters that control the FSW process as well as the effects that they might have in the weld if not correctly regulated are described next. It is important to mention that as FSW equipment gets more sophisticated, as the years go by, the capacity to quantify the effect and control diverse process parameters also increases.

- Tool rotational speed (Ω, rev/min): The tool rotational speed has a direct impact in the temperatures generated during the welding process, since it dictates the degree of friction heating involved. As mentioned, an increase in the tool rotational speed will lead to an increase in the temperatures reached in the weld. The temperatures attained during the process are important since they impact the level of plasticity of the material: if the temperatures are not high enough, defects may arise and if the temperatures are too high, then the stir zone may collapse. The tool can rotate either on the clockwise or in the counterclockwise direction.

- Tool travel/transversal speed (v, mm/min): Also known as welding speed, the tool travel speed also has a direct impact in the temperatures generated during the FSW process. As mentioned previously, high travel speeds will lead to lower energy inputs, meaning that lower temperatures are registered during the welding process. The tool transversal speed is a function of other process parameters and factors such as the tool rotational speed, joint type, alloy being welded and the penetration depth [15].
  The correlation between the two aforementioned speeds (known as the Ω/v factor) dictates the dynamics that regulate not only the heat generated during the welding process but also its plastic material flow. Based on this correlation, the FSW operation can be classified into Hot and Cold. Different material flows and heat generations are associated with each classification. As it will be discussed in next section of this chapter, a different macrostructure is obtained considering the use of a hot or cold process.

- Tool geometry: The tool geometry, which includes the geometry and design of both the pin and shoulder, is one of the most important process parameters due to its effect over the final properties of the weld.

  It affects the material flow as well as the heat generated during the operation. For example, greater shoulder diameters intensify the heat generated as a result of an increase in the friction area [16]. The key geometric parameters are the pin and shoulder geometry as well as the shoulder diameter and pin length.

  The shoulder has as primary function containing the flow of material that is being extruded and forged around the tool pin. For this purpose, different shoulders configurations can be employed. Two of them are shown in Figure 2.5.

Different pin profiles that can be used in a FSW tool are shown in Figure 2.6. The geometries of the pin can be divided into two major categories: axisymmetric and non-axisymmetric. Under each category different configurations are available.

The material used in construction of the tool must have good mechanical properties at the temperatures generated during the process (specially wear resistance).

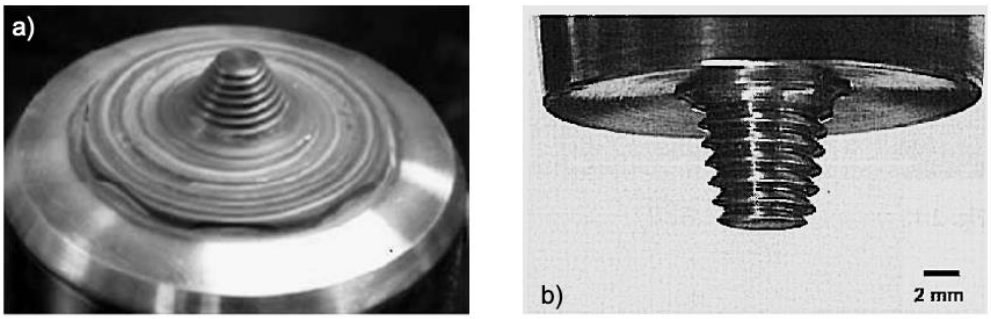

Figure 2.5- Shapes of the FSW tool shoulder: a) convex and scrolled [17], b) concave [18].

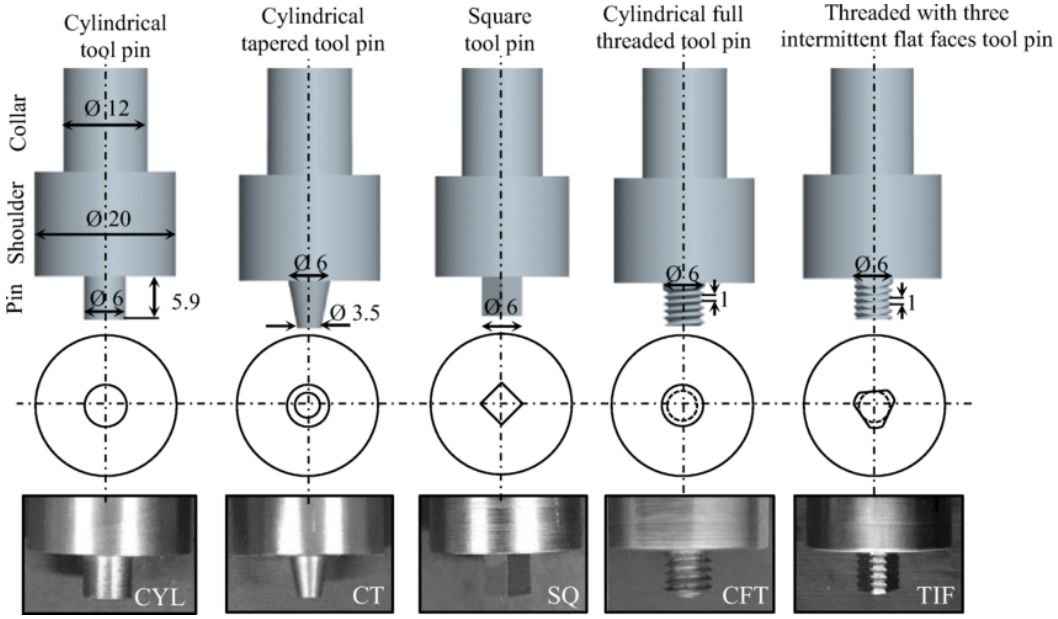

Figure 2.6- Different tool pin profiles that can be used in FSW (dimension in millimeters) *[19]*.

- Tool tilt (α, º): The tool tilt angle can be described as the inclination of the tool rotational axis. The tool tilt has an influence in the appearance of the weld. An adequate tool tilt guarantees that the shoulder of the tool holds the stirred material and that the material is moved efficiently from the front to the back of the pin. The tool tilt is generally small and is set in such a way that the rear of the tool is lower than the front (as shown in Figure 2.7). In this way, the forging process of the material located behind the tool is facilitated.

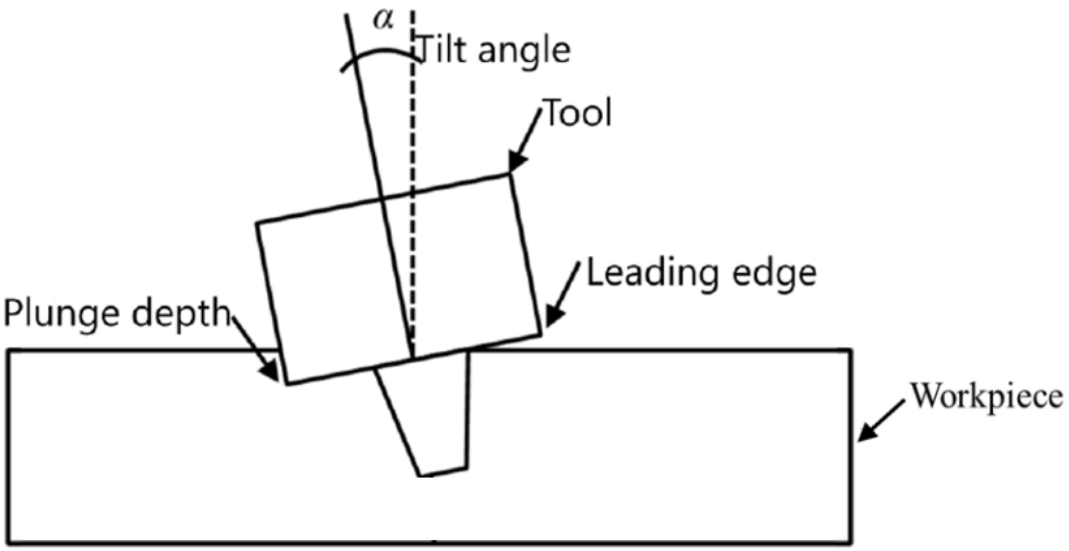

Figure 2.7- Illustration of the FSW tool plunge depth and tilt angle (adapted from Dialami et al. [20]).

- Tool plunge depth: The plunge depth consists in the penetration depth of the shoulder surface into the workpiece surface. It is important in order to obtain flawless welds, to provide the necessary axial force and to obtain appropriate weld penetration. The tool plunge depth is represented in Figure 2.7.
- Tool plunge speed: The tool plunge speed is the speed at which the tool is inserted into the weld joint.
- Axial force: In order to perform a FSW operation a force perpendicular to the workpieces (z axis of Figure 2.1) is applied by the tool shoulder. The axial force assures that the welding tool remains in contact with the workpiece. The process friction coefficient, which as mentioned previously is the primary heat generation source of the operation, is also set by this force.

  If the pressure exerted by the tool is too low, there won't be enough heat generated, resulting in lack of bonding and defects may arise. On the other hand, if the said pressure is too high, distortion of the workpieces can occur. The tool plunge depth is a direct result of the axial force. The axial force can be increased by an increase in the plunge depth, which leads to higher heat generation. On another hand, a reduction in the plunge depth results in lower axial forces thus leading to a lower heat generation.

  The welding operation can be conducted with position control, which means that the axial force will vary along the process. This may result in joints of lower quality.

- Preheating: Pre-heating operations can be used for materials that have high melting points in order to facilitate the material flow.

The non-optimization of the aforementioned process parameters can result in welding defects which may compromise the structural integrity of the weld. For this purpose, optimization techniques, such as the Taguchi method, can be employed in order to determine their optimal value.

2.2.4. Joint Metallography Characterization

For friction stir welds, from a microstructural perspective, usually four microstructurally different regions can be identified (in the weld cross section): the stir zone (SZ, also known and referred in the literature as weld nugget), the thermo-mechanically affected zone (TMAZ), the heat affected zone (HAZ) and the base Material (BM) (also designated unaffected material or parent material).

The schematic representation of the listed regions is shown in Figure 2.8.

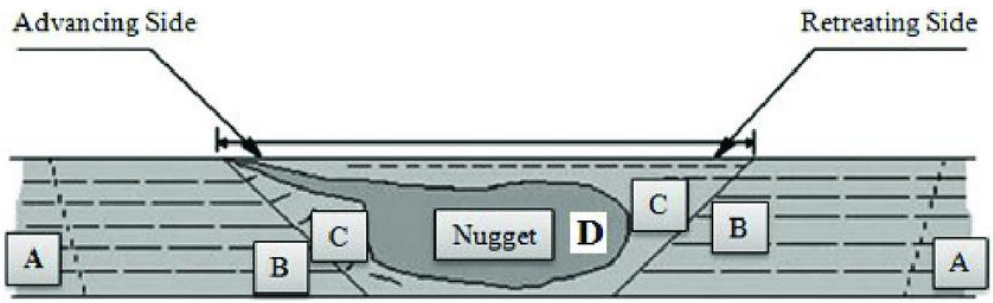

Figure 2.8- Schematic representation of the typical microstructural regions of a weld obtained by FSW: A- base material, B- heat affected zone, C- thermo-mechanically affected zone, D- stir zone [21].

These regions are divided taking into account the different microstructural properties that they present. The intense plastic deformation that the material undergoes combined with the different temperature gradients generated during the welding process are factors responsible for this difference, resulting in each one of the regions possessing their own distinguishing structure.

The microstructure of the aforementioned regions has a major impact over the mechanical properties of the welded joint, making it a research topic for many investigators. Their main characteristics are listed below:

1. Stir Zone (SZ): This region is characterized by a dynamically recrystallized microstructure with a fine and equiaxed grain structure that is a result of the extreme plastic deformation and frictional heat that the material is subjected to during the FSW process, in this region. Therefore, this region is also known as the dynamically recrystallized zone (DXZ). The center of the SZ regularly presents a circular pattern, the so-called “onion rings”. Krishnan

[22] found that the formation of this feature is mainly due to geometric effects. The onion rings do not present a different microstructure comparatively to the rest of the nugget. The “onion ring” pattern is characteristic of welds of aluminum alloys.

The process parameters not only control the size of the aforementioned recrystallized grain structure but also control the shape of the SZ. Regarding its shape, the stir zone can be categorized as elliptical or basin. In Figure 2.9, an example of each type of this shapes can be observed.

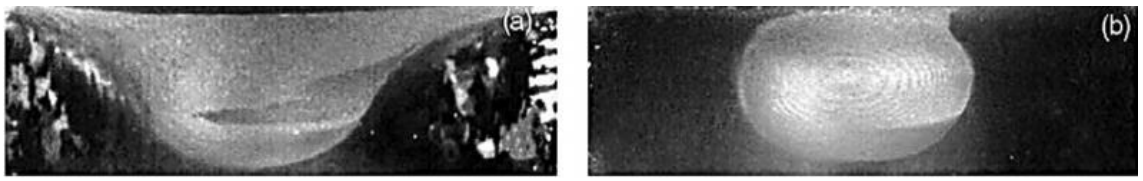

Figure 2.9- Types of stir zone shapes obtained by FSW: a) Basin [12], b) Elliptical [23].

In this region, the grain size varies between 2-15 μm depending on the material that is being welded as well as the welding parameters set for the process. The density of dislocations in the SZ is lower than the one presented by the parent material.

Significant grain refinement occurs in this region. An increase in the welding speed, or lowering the rotational speed of the tool, will, as mentioned in the previous section, lead to lower energy inputs, thus resulting in higher cooling rates which by their turn will lead to a higher degree of grain refinement. This is supported by the observations made by Ahmed et al. [24] who were able to observe, from their experimental work, that as the welding speed increased, the grain size of the SZ was continuously lowering. These observations were made for AA7075 and AA5083 similar friction stir welded joints.

2. Thermo-mechanically affected zone (TMAZ): The TMAZ corresponds to a thin transition region located between the SZ and the heat affected zone (HAZ). Regarding its structure, the TMAZ possesses a deformed (to a great extent) and non-homogeneous one.

   Contrasting with the SZ, the material of the TMAZ has not undergone a full and distinct recrystallization process. Despite the occurrence of plastic deformation, caused by the FSW tool, it is lower and not as severe as the one experienced by the material of the stir zone thus the strain energy is not sufficient to lead to a distinct recrystallization. It is commonly accepted that this region is characteristic of friction stir welds of aluminum alloys, since other materials may present a fully recrystallized TMAZ and a distinction between the TMAZ and the stir zone is not clear, in those cases. Partial dissolution of precipitates can occur depending on the type of material and thermal cycles that the region experiences. Usually, the transition between the stir zone to the thermo-mechanically affected zone is relatively smooth in the retreating side of the weld. On the other hand, the transition to the TMAZ is more distinguished/clearer in the advancing side

of the weld. This is a result of the different direction that the tool rotational speed takes relatively to the tool travel speed on both sides of the weld.

3. Heat Affected Zone (HAZ): The HAZ is a region that is not mechanically affected (plastic deformation does not occur), hence only affected by heat, although to a lower extent comparatively to the previous region and the SZ (as it is verified in fusion welding processes). Nevertheless, the precipitate structure can present changes comparatively to the base material's. Coalescence or dissolution of precipitates may occur, in the HAZ, depending on the base material used, its treatment and the proximity to the region where the FSW tool imposes plastic deformation, as well as grain recovery or growth.

4. Base Material (BM): This region can experience thermal cycles, but despite the temperature variations that the material undergoes its microstructure is not remarkably altered as a consequence, ergo, the mechanical properties remain the same. Generally, the region is also characterized by an elongated grain morphology that points out the rolling direction.

As mentioned previously, according to the welding parameters that are set, more precisely the tool rotational and transversal speed, the FSW operation can be classified into hot or cold depending on if the material is welded under hot or cold-welding conditions. Regarding the former, it results in a wider heat affected zone as a result of the increase of visco-plastic material flow concentration around the tool pin. Cold welding conditions result in a wider thermo-mechanically heat affect zoned and a smaller heat affected zone. This effects are summarized in Figure 2.10.

As mentioned previously, the resulting microstructure of the welds has a major impact over their mechanical properties. During the next section of the present chapter, the most common types of welding defects will be listed, and their causes analyzed.

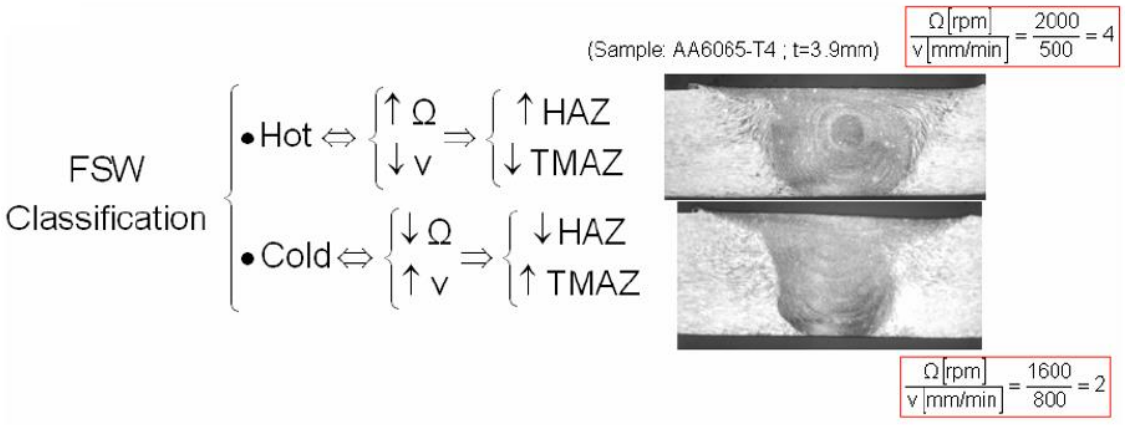

Figure 2.10- FSW classification and effect over the size of the HAZ and TMAZ [25].

2.2.5. FSW Process Defects

Despite the excellent weld quality that is commonly obtained via friction stir welding, it is unlikely that all welds obtained with this process are completely free of defects. As mentioned, FSW is a solid-state welding process thus the defects that are characteristic of fusion welding processes do not occur nevertheless, other type of defects may arise.

The defects are usually a result of improper process parameters selection/setting. The most common FSW defects that may form when welding aluminium and aluminium alloys are summarized in Table 2.6. In it, information regarding the causes of each type of defect as well as their location is also provided. Other FSW defects than the ones listed in Table 2.5 may appear during the welding process (as for example cracks or porosities) but not as frequently.

Through Figures 2.11 to 2.13 examples of some of the welding defects that are listed in Table 2.5 are provided.

Another relevant aspect worth mentioning is that although the tool is non-consumable as mentioned in the beginning of this chapter, wear of the tool will occur as it is being used. This will result in dimensional changes which may also lead to the formation of weld defects. As a result of the tool wear some inclusions of the tool material can exist in the weld, which can have a detrimental effect over its mechanical properties.

Nevertheless, the FSW process offers many advantages not only relatively to other welding processes but also in comparison to other mechanical joining processes.

Along the next section of this chapter, the benefits and limitations of the process will be looked over.

Table 2.5- Common defects of the FSW process [11], [26], [27], [28], [29], [30].

Defect	Description	Location
Tunnel	Tunnel defects are a volumetric type of defect which are caused by deficient material flow around the tool pin during the welding process. The deficient material flow around the tool pin is a result of improper material stirring and mixing instigated by low energy inputs. The mechanical properties of the welds are highly affected when this type of defect arises.	Advancing side of the weld, between the TMAZ and the stir zone.
Kissing Bonds (Figure 2.11)	Kissing bonds are characterized by two adjacent surfaces being in close contact, but with no metallic bond formed. It is a type of defect that is hard to detect since the surfaces are in contact at a molecular level. It is caused by insufficient stirring of the material and an inadequate pressure which leads to an improper material deformation. This inefficient material deformation may result in entrapped oxides from the base material. The oxide inclusions can take the form of a zigzag line and in those scenarios this defect is named Zigzag defect. This defect is of special interest when welding aluminum and its alloys due to their high affinity with oxygen thus rapidly forming an alumina (oxide) layer.	Root of the weld, weld joint interface.
Voids	Also known as wormhole defect, it is a volumetric defect which results from unusual material flow during the welding process. It occurs when the stirred material cools and loses its capability to fill the region left behind the tool. Voids are more prone to be formed when high welding speeds are used in the welding process. The use of high welding speeds lead to lower energy inputs and thus faster cooling rates. A low forging pressure can also contribute to the formation of this type of defect as well as an incorrect clamping of the workpieces (the joint gap should not be very substantial)	Advancing side of the weld or underneath the weld's top surface.
Incomplete Root Penetration (Figure 2.12)	It occurs when material located at the root of the weld remains unstirred and unconsolidated. Some of the factors that may contribute to the formation of such a type of defect include inadequate clamping forces, an incorrect tool design or the use of low energy inputs.	Root of the weld
Hooking	This defect is characteristic of a lap joint configuration. It is related to the bending of the interface between two workpieces, as a result of the upward movement of the material from the bottom workpiece as it is being stirred.	TMAZ of both advancing and retreating side of the weld.
Flash (Figure 2.13)	This defect arises when during the welding process, material is dislocated into the edge of the weld and is then accumulated. It occurs due to the use of energy inputs that are too high (extreme plastic deformation occurs) leading to a softening of the material nearby the tool shoulder, which is posteriorly expelled. Although being undesirable, the formation of flash can be used as an indicator regarding the use of a correct tool plunge for a certain welding operation: if the plunge depth is too high, excessive flash will be formed.	Outer edges of the weld joint.
Joint line remnants	Two variations of this defects have been observed [31]: one in which the interface between the workpieces is not totally disrupted and therefore their interfaces can still be identified in the weld cross-section, leading to lower tensile and fatigue properties of the welds. The other variation is the result of the formation of an approximately dispersed continuous oxide layer located inside the stir zone of the weld. Inadequate cleaning of the workpieces prior to the welding process, setting an erroneous plunge depth or having an improper alignment of the tool regarding the joint line are some of the most common causes of the joint line remnant defect.	Root of the weld with the possibility to be extended up to the stir zone.

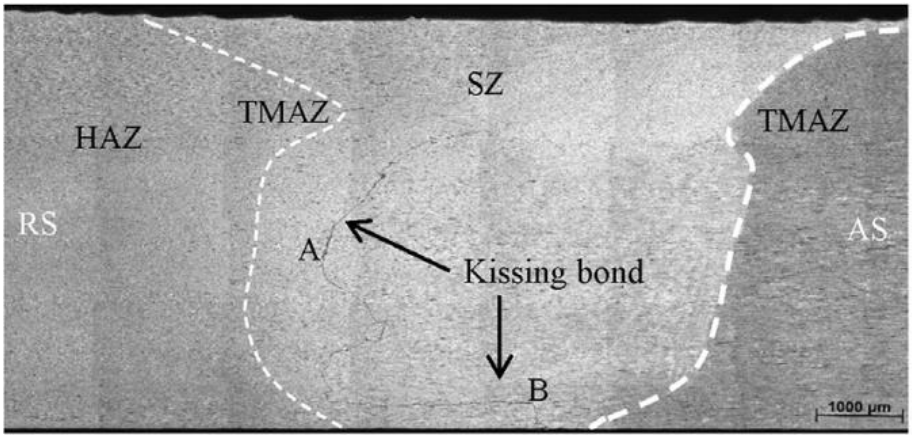

Figure 2.11- Macrograph of a weld with a kissing bond highlighted [32].

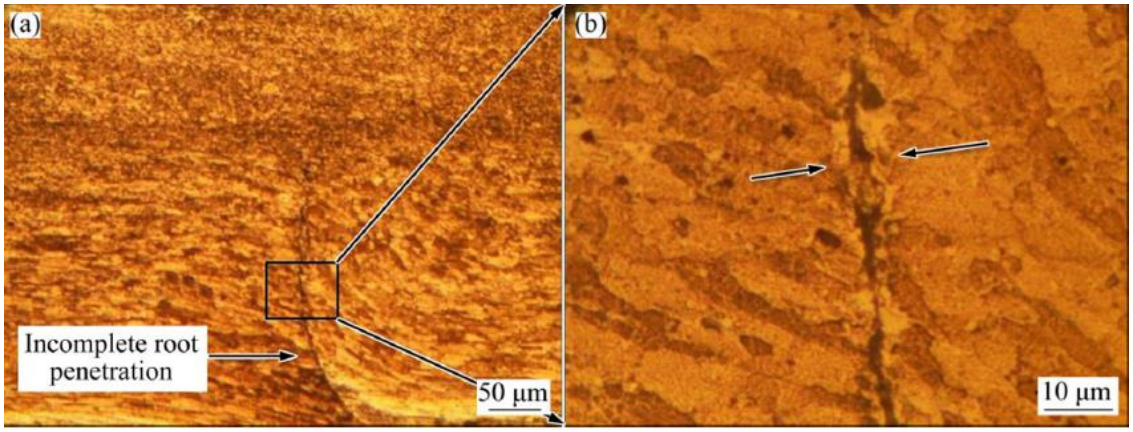

Figure 2.12: Friction stir weld with incomplete root penetration [29].

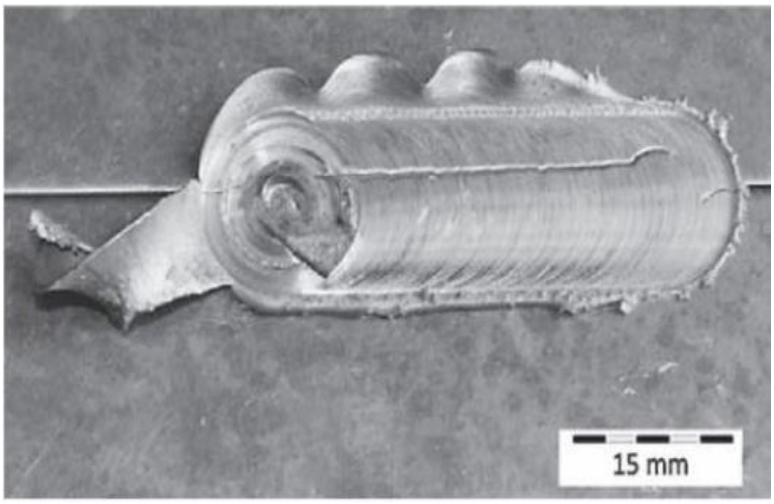

Figure 2.13- Weld with excessive flash on the outer edges of the surface [33].

2.2.6. Benefits and Limitations of FSW

Throughout the present chapter of this document, the fact that FSW is a solid-state process, and thus the formation of fusion welding characteristic defects does not occur, has been mentioned on a few occasions. Nevertheless, the benefits of the FSW process extend beyond that and most of them can be divided into four major categories: metallurgical, environmental, energy and costs related, as shown in Table 2.6, which summarizes the fundamental properties of the FSW process that can be translated into benefits.

Other benefits that come from the use of the FSW process include the production of seamless welds with excellent aesthetics, the feasibility of welding aluminum alloys considered difficult to weld through the use of other welding processes (for example the alloys of the 7XXX series), the possibility to use multiple joint configurations and the process safety level.

However, some limitations regarding FSW can be encountered:

- One disadvantage of the process is related to the retraction stage which was presented previously. At the end of the welding process. when the tool is pulled away from the workpiece it generally leaves a hole in it, depending on the tool design. The hole is, in most of the cases, removed leading to material waste. In other situations, the hole is sealed by resorting to other processes. Although not difficult to remove, the formation of an exit-hole remains one of the biggest disadvantages of FSW.
- Another disadvantage is related to the process welding speed (tool travel speed). It is rather low when compared to other welding processes such as laser beam welding (LBW) and electron beam welding (EBW) thus resulting, in comparison, in lower productivities.
- Since the axial forces exerted by the FSW tool can be very high, a powerful and robust clamping system is required in order to maintain the workpieces in the correct position during the operation. This can lead to high clamping forces which may have a detrimental effect over the mechanical properties of the resulting welded joint.
- The FSW equipment requires a high initial investment making it sometimes not the best economical solution for low productivities. The transportation of the equipment is also an inconvenient when compared to other welding processes, as for example, SMAW (shielded metal arc welding), which equipment is rather easy to transport.

Despite the aforementioned downsides of using the FSW process, it is still a widely used welding process across various industries. The next section of this chapter will be dedicated to presenting two of those industries in detail as well as concrete products in which FSW was used throughout their manufacturing process.

Table 2.6- FSW metallurgical, environmental, energy and costs related benefits [26], [30], [34].

Metallurgical Benefits	Environmental Benefits	Energy Benefits	Costs Benefits
• FSW is a solid-state welding process leading to low residual stresses and low distortion of the workpieces. • A fine and recrystallized microstructure is obtained. • During the welding process, low temperature gradients are registered which results in more ductile welds. • No variation in the alloying content of the workpieces. • Excellent mechanical properties of the welds. • Good dimensional stability and repeatability. • No solidification defects (solidification cracking for example). • Possibility to obtain welds of good quality for joints of dissimilar aluminum alloys.	• No harmful emissions since there is no need for shielding gases. • FSW allows materials savings since no filler material or other consumables are used. • FSW noise level is low. • Process free from wastes (as for example grinding wastes). • Minimal (or even no) surface cleaning required. • Comparatively to other welding processes, FSW requires less energy.	• FSW allows to obtain structures that are more lightweight since no filler material is used, leading to lower fuel consumption in the automotive, aerospace and ship industries. • Compared to other processes the energy requirements are lower as well as the energy losses.	• Minimal to no surface cleaning required. • The process repeatability and the fact that it can be fully automated allow to boost productivity. • Operation cost is lower as a result of being a process free of consumables. • No skilled workers required. • FSW offers the possibility to obtain products in the condition ready-to-use: no post-welding treatments are not necessary, • Minimum maintenance of the equipment is required.

2.2.7. FSW Applications

Friction Stir Welding applications are very diverse regarding both the components for which the process can be employed as well as in regard to the industries in which the process is adopted. The purpose of the companies that make use of this process is to take advantage of the multiple benefits offered by FSW, that have been previously depicted in Table 2.6.

The fact that FSW is a welding process that allows aluminum welds with excellent mechanical properties to be easily obtained is also very appealing, considering the fact that aluminum and its alloys are very appreciated due to their inherent characteristics such as availability, low price and high strength-to-weight ratio thus being used in diverse industries.

The use of FSW in the aerospace and automotive industry is analyzed in more detail throughout this section, as these are two of the industries that have benefited the most from the use of this process.

- Aerospace Industry Applications

  In the past, structures used in the aerospace industry were mainly joined by means of mechanical joining processes such as riveting. The use of such processes was mainly due to the fact that high-strength aluminum alloys (such as the 2XXX and 7XXX series) which are the materials usually employed in aerospace structures like fuselages, fuel tanks and wings [12], are materials that are prone to solidification cracking thus not suitable to be welded by fusion welding processes.

The development of FSW has proven to be a great advantage making it possible to obtain the mentioned structures with a lower weight, at a lower price and manufacturing time while not abdicating of the weld quality. For example, Boeing used this process in the manufacturing process of a rocket fuel tank. The fuel tank was welded by means of the TIG in previous models and the transition to FSW allowed the company to reduce the welding costs in approximately 99%. Another example that translates this costs savings regards the Eclipse Aerospace company that used FSW in the manufacturing process of their 500 and 550 series business jets. The use of FSW allowed to eliminate more than 60% of the riveted joints, contributing to a substantial decrease in the materials used (which resulted in an overall weight reduction), the manufacturing time (around 10 times faster than by using rivets). The use of FSW also allowed this business jets to have their service life duplicated as a result of the improved strength granted by the process comparatively to the one offered by means of riveting [26], [27].

More recently, SpaceX used the FSW process in their Falcon vehicles (Figure 2.14) in order to manufacture the propellant tank walls [35].

Figure 2.14- Friction stir welds on the propellant tank walls of the Space X Falcon 9 [35].

- Automotive Industry Applications

  Nowadays, awareness regarding our CO_2 footprint on Earth is becoming a critical matter in order to promote and ensure the sustainability of the planet. In this context, FSW can play an important role since, as stated in the previous section, being a welding process that does not require the use of filler material (autogenous process), FSW allows to obtain structures that are more lightweight, leading in this way to lower fuel consumptions and therefore to lower emissions (for non-EVs) and at the same time it allows to obtain

aluminum welds with excellent mechanical properties, free from solidification defects and with good aesthetics.

In this century, many car manufacturers have already made use of this process. Audi for the R8 Spyder B-pillar, Mazda for the RX-8 rear doors and hood and Maclaren for some of the Maclaren 12 C structural parts [36]. Other examples, that portray the diversity of the application of FSW within the automotive industry include the production of aluminum wheels (that can be found in Volvo's cars) and heat exchangers (for BMW and Chrysler car models).

Regarding the use of FSW in the manufacturing process of electric cars, TRAC- Industrie, in 2012, became the first company to employ the FSW process, in a production series, in France, in order to manufacture the battery tray for the Renault Zoe [37]. More recently, Tesla announced that the Model Y battery box was manufactured by using the FSW process, as well as the Octovalve, a component that is responsible for cooling some critical components of the car, such as batteries and the motor. The FSW process has also been used in other vehicles besides passenger vehicles: for example, it has been adopted in the manufacturing process of battery cooling plates for E-trucks [36].

The employment of FSW within the aforementioned industries is expected to grow in the future, as a result of the EU's Green Deal and Horizon Europe funding program, that aim to promote a more sustainable future, by tackling the emissions of the transport industry, which accounts for about 25% of the total emission of greenhouse gases, in the EU [1], [2].

FSW has also found applications in other industries such as the ship, marine, armor and railway industries [38].

The process has also been implemented in electronic equipment. In 2012, Apple used FSW in the manufacturing process of the iMac which made it possible to obtain a product 40% thinner comparatively to previous models [39].

2.3. Fatigue

2.3.1. Fatigue Properties

Historically, fatigue effects over different type of structures and equipment have been observed and documented for a long period of time. It was in the 1800's, driven by the industrial revolution, that the first fatigue experiments/investigations were carried out to better understand its mechanisms.

Fatigue is a failure mechanism that can only occur when cyclic, dynamic loads are applied to materials (this means that it requires loads that fluctuate with time). This type of failure can take place at stress levels that are inferior to the materials' yield strength which can be quite challenging since it can occur at stress levels that are apparently safe, well below the materials' limits. Fatigue failure can take up to, generally, 10^3 to 10^7 cycles to occur and typically takes place in three stages: crack initiation**,** crack propagation and the final fracture [40].

The stress-life method is one of three main approaches that exist and that are available in order to evaluate and analyze when a certain material is expected to fail when submitted to this sort of loads. The other two approaches are the stress-life and fracture mechanics methods.
Each one of them is different, as they focus on different aspects of this failure mechanism.
Although being the least accurate, the stress-life method is the most commonly used when assessing the fatigue behavior of materials. This can be explained by the fact that it is an approach that is relatively easy to implement, for which there is currently a lot of data available for a wide range of materials.
This approach is based in the use of S-N curves, also known as Wöhler curves, that are built taking into account the number of cycles registered for failure to occur at a certain stress level.
It is suitable to be used when the applied stresses are in the range of the elastic behavior of the material and therefore, it has a long cyclic life (High Cycle Fatigue). If the applied stresses are in the range of the plastic behavior of the material, the strain-life method is more suitable, taking into account that the material would have a short cyclic life (Low Cycle Fatigue).
Regarding the fracture mechanics approach, it focuses in evaluating the fatigue crack growth and propagation mechanism [40], [41].

As mentioned previously, for fatigue failure to occur a certain material must be submitted to cyclic loads.

Cyclic loads can be quantified through the use of some parameters, being the most important ones the stress range, $\Delta\sigma$, the stress amplitude, σ_a, (both serve as indicators of the magnitude of the cycles) and the mean stress, σ_m. These parameters are represented in Figure 2.15.

The values of the aforementioned parameters can be determined through the use of Equations 2.1, 2.2 and 2.3 respectively.

The mean stress value can also be quantified through the stress ratio, R, which by its turn is defined by Equation 2.4.

The stress ratio can take any value within the -∞ to 1 interval ($R \in [-\infty, 1]$).

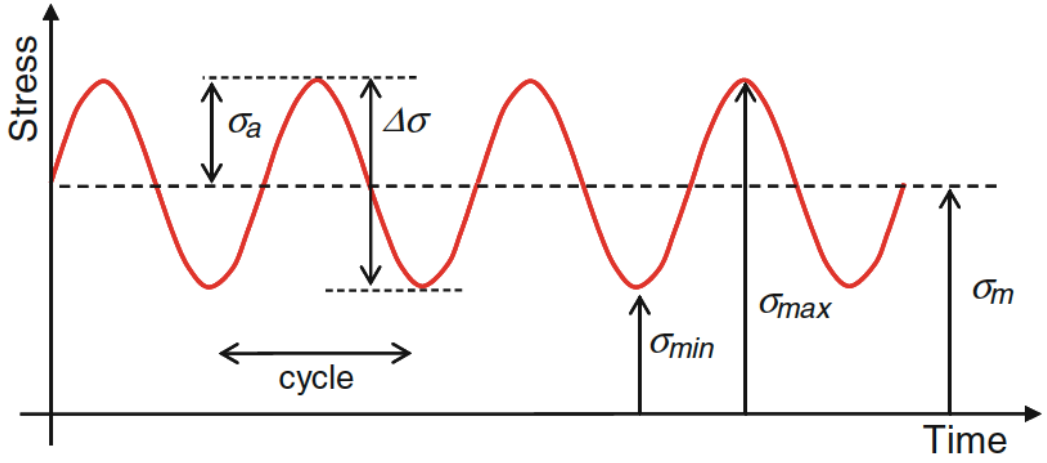

Figure 2.15- Representation of the parameters used to characterize cyclic loads [40].

$$\Delta\sigma = \sigma_{max} - \sigma_{min} \tag{2.1}$$

$$\sigma_a = \frac{\Delta\sigma}{2} = \frac{\sigma_{max} - \sigma_{min}}{2} \tag{2.2}$$

$$\sigma_m = \frac{\sigma_{max} + \sigma_{min}}{2} \tag{2.3}$$

$$R = \frac{\sigma_{min}}{\sigma_{max}} \tag{2.4}$$

The stress ratio plays an important role in fatigue life of materials has it influences the fatigue crack growth: an increase of the stress ratio, leads to higher crack growth rates for the same stress intensity factor range, as shown in Figure 2.16.

The occurrence of crack closure is usually assumed to be the cause of the different crack growth rates when different stress ratios are applied.

Regarding the effect of R over S-N curves, lower stress ratios result in the curves moving upwards in the stress-life diagrams when taking into account the stress amplitude of the cycling load, as shown in Figure 2.17, which indicates an increase in the fatigue life.

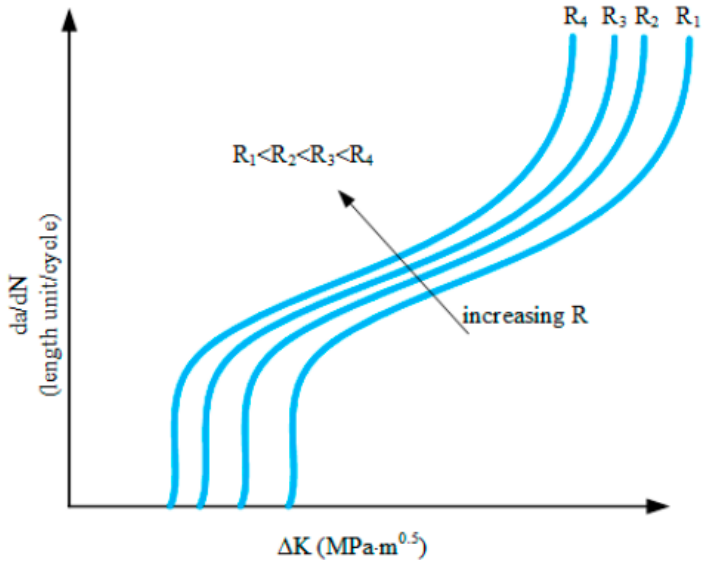

Figure 2.16- R and ΔK influence over the fatigue crack growth rate [42].

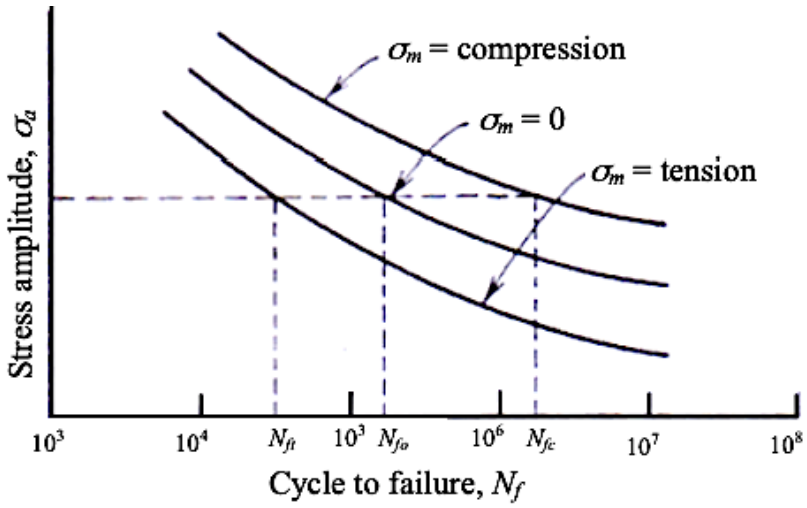

Figure 2.17- Influence of different mean stresses over the fatigue life [43].

There are other parameters that also have an important effect in what regards the materials' fatigue life, such as the loading temperature.

As a general rule, the fatigue life decreases with an increase in temperature. This phenomenon can be explained by the fact that higher temperatures facilitate the process of crack nucleation and lead to an increase in the fatigue crack growth rate, being the growth rate significantly higher as the temperature increases.

Also, the crack nucleation occurs at a lower number of cycles for increased temperatures. From research, it was found that for AA6061, the number of cycles until failure at 300 ºC was reduced in about 99% when compared to the number of cycles required to produce the same effect at room temperature [10].

2.3.2. Fatigue Properties in FSW

In a previous section of the present chapter, some different industrial applications, in which FSW has proven to be useful, were discussed and some real examples were mentioned. As seen, the applications are miscellaneous varying from aerospace structures to vehicles' components.

Throughout their service life, a great part of those parts are subjected to fluctuating loads which explains the reason why the principal failure mechanism and failure mode of joints obtained by FSW are fatigue and fatigue fracture respectively [3]. If we take as an example the use of FSW in the aerospace industry, more precisely in the manufacturing process of an aircraft wing, fatigue failure can have a tremendous economic impact over the manufacturing company and may even put in danger human lives, as it is one of the most fundamental structures of any aircraft. Therefore, understanding the fatigue mechanisms of friction stir welds is of extreme importance in order to allow developments and improvements in what regards the fatigue life of the aircraft wing. This applies to all components/parts in which FSW is or might be employed. Different factors can impact the fatigue performance of FSW joints.

The effect of residual stresses, loading temperatures among other factors are discussed in more detail in the course of this section.

- Residual Stresses

  The mechanical properties of a weld are highly influenced by the existence of residual stresses. Residual stresses, as explained previously, have a detrimental effect over fatigue properties. This is also verified for welds obtained by FSW. Although being a solid-state welding process characterized by low energy inputs, residual stresses will still develop in friction stir welds and will negatively affect the fatigue crack growth process and thus the fatigue life of the welds as observed by John et al. [44].

  One major source of residual stresses in this type of welds are the high clamping forces required in order to fix and keep the workpieces in contact, during the operation. These clamping forces introduce a degree of restraint, restraining the stir zone and HAZ during the cooling process, leading to the introduction of residual stresses.

  This type of welds present different residual stresses distributions along the longitudinal and transverse directions. Peel et al. [45] investigated the longitudinal and transverse residual stress distributions of AA5083 friction stir welds. The results that were obtained are shown in Figure 2.18. By analyzing Figure 2.18, it is possible to infer that the longitudinal residual stress distribution follows an M pattern, with the maximum values observed in the HAZ. On another hand, the transverse residual stress distribution has its maximum close to the weld center. From Figure 2.18, it is also possible to verify that the longitudinal stress distribution is asymmetric, since the stresses are slightly higher in the advancing side of the weld in comparison with the residual stresses presented at the retreating side of the weld. The maximum residual stress in the longitudinal direction is

higher than the one showed in the transverse direction and both values' magnitude is inferior to the yield strength of the material.

Tensile residual stresses have a more detrimental effect over the fatigue properties of the welds comparatively to the effect of compressive residual stresses, as the latter cause crack arrest, a phenomenon in which the fatigue crack growth rate is significantly lowered. In both distributions, the residual stresses present oscillations, oscillations between compressive and tensile residual stresses can be observed as the distance to the weld line varies. In both directions the weld zone is in a tensile state therefore the fatigue crack growth rates are expected to be higher in this region. Peel et al. [45] verified that the tool transverse speed plays an important role in respect to the longitudinal residual stress distribution, due to the way that it affects the thermal gradients during the welding process as well as due to its impact in the time for stress relaxation. They were also able to conclude that the tool transverse speed does not have a direct impact on the distribution of residual stresses in the transverse direction.

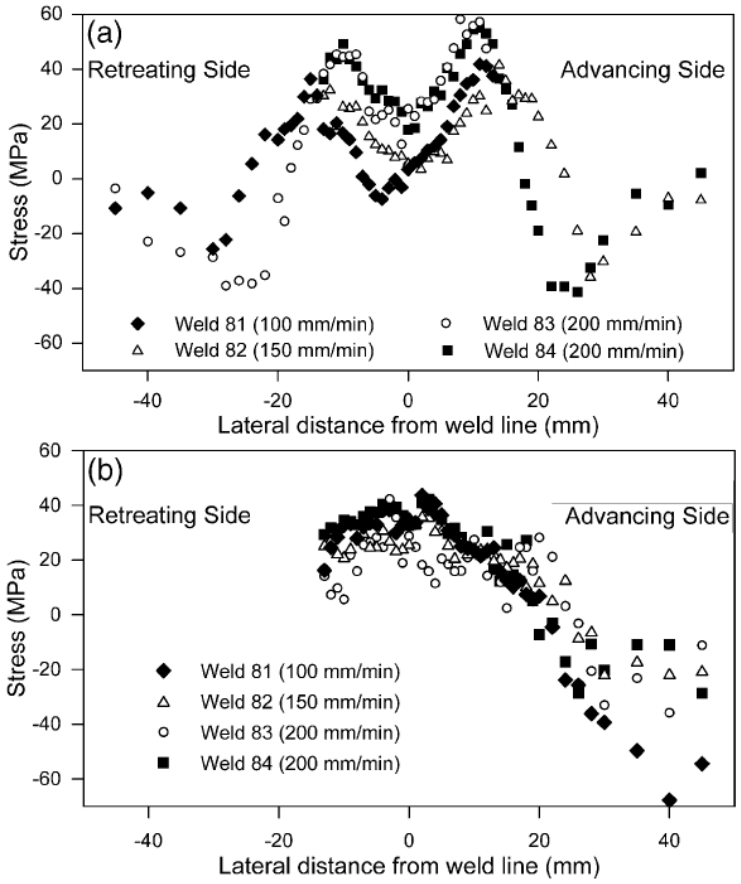

Figure 2.18- a) Longitudinal and b) transverse residual stresses distribution for AA5083 friction stir welds [45].

Zhou et al. [32] discovered that the fracture point (caused by the fatigue tests) of friction stir welds, made of AA5083, occurred in regions located near the advancing side. This was assumed to be due to the higher residual stresses encountered in this region, as explained and shown previously, as well as due to the fact of the region being characterized by a high stress concentration.

Residual stresses that result from the FSW operation are not definitive, as they can be reduced or even completely purged by other processes such as shot peening or by aging treatments.

- Stress Ratio

Li [46] observed the effect of different stress ratios over the fatigue crack growth rate of AA7075-T651 friction stir welds. The results obtained are shown in Figure 2.19. For the same stress intensity factor range, it is possible to see, in Figure 2.19, that higher stress ratios have a more detrimental effect over the fatigue life of the welds since higher stress ratios led to higher fatigue crack growth rates. From the experimental work that was developed it was also possible to see that this effect becomes less significant as the stress ratio value increases: the difference in the fatigue crack growth rate, for the same stress intensity factor range, is higher when comparing R= 0.1 and R= 0.3 than when comparing the values obtained for R= 0.3 and R= 0.5. This can be justified by the occurrence of the crack closure phenomenon.

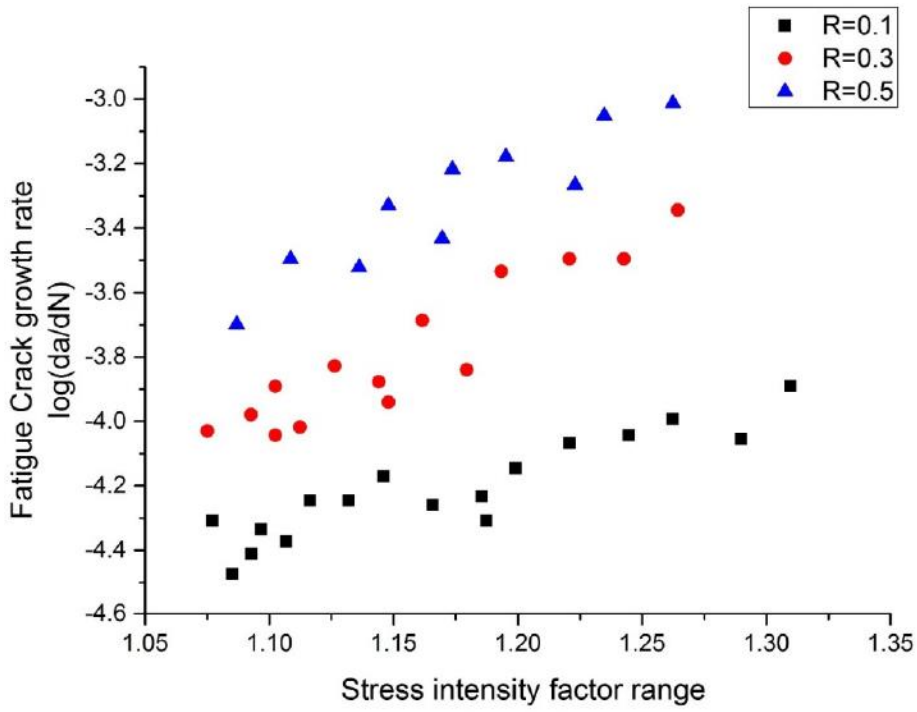

Figure 2.19- Stress ratio effect over the fatigue crack growth rate of AA7075-T651 friction stir welds [46].

Observations that are in line with the results obtained from the work developed by Li [46] were made by Pouget & Reynolds [47]. Their work focused on the analysis of the fatigue crack growth in AA2050 FSW joints. They verified that an increase in the stress ratio led to an increase in the fatigue crack growth rate. However, this trend was only verified for low stress ratios (up to 0.4). For higher stress ratios, the impact in the fatigue crack growth rate was negligible.

Lomolino et al. [48] observed, through the analysis of available literature, that the fatigue strength of welds obtained by FSW tested with a stress ratio of -1 was superior to the one displayed by welds tested with a stress ratio of 0.1, as a result of the fact that the stress was partially compressive when the former was applied.

- Loading Temperature

  Temperature also influences the fatigue behavior of welds obtained by FSW.

  Resan et al. [49] found that their fatigue life decreased with an increase in the temperature at which the fatigue tests were being performed. The research consisted in the investigation of the effect of both the loading temperature and tool rotational speed over the fatigue life of AA2024 friction stir welds. During the experiments, for the same tool rotational speed, the responses to increasing loading temperatures were registered. The procedure was repeated for different tool rotational speeds. It was possible to conclude that for the same rotational speed, increasing the fatigue testing temperature had a detrimental effect regarding the fatigue life of the welds.
  By their turn, Tra et al. [50] witnessed that the fatigue crack growth rates were sensible/influenced by the temperature at which the fatigue tests were carried out. A comparison was made between the rates obtained at room temperature and at 200 ºC. The results point out to the same conclusion obtained by Resan et al [49]. These experiments were performed in AA6063-T5 welds obtained by FSW.

- Surface Finish

  Bussu & Irving [51] reported that the surface finish also influences the fatigue resistance of welds obtained by FSW. Surface defects act as stress concentrators, which will enhance the process of crack initiation. By using processes that allow to remove layers of material (such as milling), the surface finish can be improved and as a result the fatigue resistance increased [52]. The same conclusion can be withdrawn from the work of Vidal et al. [53].

- FSW Defects

  Research has also been developed to evaluate the effect of the defects that may result from FSW, in the fatigue life of the welded joints.

James et al. [54] verified through their research on the fatigue life of AA5083-H321 friction stir welds that defects similar to the kissing bond defect (see Table 2.5), although not related to the fatigue crack initiation process, had an important role in what concerns the fatigue crack propagation process, since this type of defect had the capability to provide connecting paths among initiated cracks.

Regarding the effect of Kissing Bonds, Kadlec et al. [55], in their research, performed mechanical tests in order to evaluate the effect of the Kissing Bond area on the fatigue properties and found out that there was a size limit beneath which the defect had no impact over the fatigue life of AA7475 welds. Results that corroborate this conclusion were obtained by Dickerson & Przydatek [56]. The work developed aimed to evaluate the influence of root defects in fatigue properties of friction stir welds. Three type of specimens were tested: specimens made of AA5083-O, AA5083-H321 and AA6082-T6. The research showed that root defects under a certain limit do not have significant effect in the fatigue life of the alloys.

The effect of other type of defects has also been studied. For example, Kahl & Osikowicz [57] found that there was a decrease in 20% of the fatigue strength of AA6061-T6 welds, obtained by FSW, which contained small voids. By their turn, James et al. [54] concluded from their research that voids can act as stress concentrators thus lowering the fatigue life of AA5083-H321 fatigue specimens, comparatively to the tested specimens that had no voids.

Many studies, which have been carried out in order to access the fatigue properties of friction stir, point out that that these type of welds, generally, display lower fatigue strength when compared to the base material, meaning that they are sensitive to fatigue crack nucleation [28].

Studies also verified that the fatigue strength of friction stir welds was higher than the one exhibited by welds obtained through fusion welding processes such as MIG or Laser Welding (both fusion welding processes). Hori et al. [58] were able to obtain the S-N curves corresponding to the fatigue performance of AA6005-T5 welds obtained by means of different welding processes, such as FSW, MIG and Laser welding and their observations validate the conclusions aforementioned: friction stir welds have better fatigue properties than welds obtained by fusion welding processes but worse, generally, when compared to the ones presented by the base material. Zhou et al. [32] also reported AA5083 welds obtained by FSW had a fatigue life significantly superior (by a factor of 10) compared to the welds obtained through the use of the MIG process.

One of the reasons that justifies this dissimilar behavior of the welds obtained by fusion welding processes and FSW is related to the resulting microstructural properties of the welds, that benefit from the absence of melting of the base material during the FSW operation.

Chapter 3

Materials and Methods

The goal of the present chapter is to give a comprehensive insight into the experimental work that was developed within the scope of the thesis. This chapter is divided in seven main sections, through which a detailed analysis of the materials used and the experimental methods that were followed is presented.

3.1. Base Material Characterization

For the execution of the experimental work, AA7075 rolled plates in the T651 condition, with a thickness of 4 mm, were selected. The material is an alloy from the 7XXX series, which means that it is heat treatable (hardened by precipitation) and its main alloying element is Zinc, according to Table 2.1.

In order to obtain the T651 temper, the alloy undergoes a solution heat treatment and is then artificially aged (T6 treatment process, Table 2.4). Additionally, the alloy is stress relieved. The stress relieving is achieved by a stretching process.

The aluminum alloys from the 7XXX series have the highest strength (being, in some alloys, a match to some types of steel) comparatively to the aluminum alloys of any other series so, it does not come as a surprise that the AA7075 alloy is characterized by a high strength, exhibiting good ductility and excellent fatigue resistance, as well. Historically, this mechanical properties lead to the alloy being used in fighter planes (such as the Mitsubishi A6M Zero fighter) during World War II and nowadays, the AA7075 alloy is widely used in the manufacturing process of highly stressed structural parts (in which the resistance to high stresses is of the upmost importance) in the aircraft industry such as wing spars, gears and shafts. It is not suitable for applications that require an excellent corrosion resistance.

As mentioned in the previous chapter of this dissertation, some of its properties such as good corrosion resistance, excellent mechanical properties and lightness make the AA7075-T651 alloy highly used in the automotive and aerospace industries.

3.1.1. Chemical Composition and Mechanical Properties

In order to determine the chemical composition of the base material, a base material sample was examined in a Jeol-7001F Field Emission Gun Scanning Electron Microscope, which was

equipped with Energy Dispersive Spectroscopy (EDS) light elements detector (accelerating voltage of 25 kV and working distance of 35 mm) with the X-ray spectra being collected for approximately 40 live seconds. The results are summarized in Table 3.1 and are compared to its composition, available in the literature. As it can be seen through the analysis of Table 3.1, three alloying elements were identified by the EDS process: Magnesium (Mg), Copper (Cu) and Zinc (Zn), with the main alloying element being Zinc, as expected and previously mentioned.

Some of the alloy's more relevant mechanical properties, considering the work developed in this thesis, can be found in Table 3.2. The hardness value that is indicated corresponds to the average value, that was experimentally obtained for a base material sample.

Table 3.1- Comparison between the chemical composition (weight percentage) of the AA7075-T651 alloy obtained by EDS and the chemical composition available in the literature [7].

Element	Wt % (EDS)	Wt % (Literature)
Aluminum (Al)	87.04	Remaining
Magnesium (Mg)	4.52	$2.1 - 2.9$
Copper (Cu)	1.84	$1.2 - 2.0$
Zinc (Zn)	6.61	$5.1 - 6.1$
Iron (Fe)	0	0.5
Chromium (Cr)	0	$0.18 - 0.28$
Silicon (Si)	0	0.4
Manganese (Mn)	0	0.3
Titanium (Ti)	0	0.2
Other Elements	0	0.15

Table 3.2- AA7075-T651 Mechanical Properties [7], [59].

Mechanical Property	Value (Units)
Yield Strength	503 (MPa)
Ultimate Tensile Strength (UTS)	572 (MPa)
Poisson's Ratio	0.33
Modulus of Elasticity	72 (GPa)
Vickers Hardness	193 (HV)

3.1.2. Microstructure

To be able to conduct a metallographic analysis of the base material and characterizing its grain structure as well as identify the presence of any type of intermetallic component, a sample was cut out from the beforementioned plates, along their rolling direction. To cut out the sample, an ADIRA GHO-0420 hydraulic sheet metal guillotine was used. Posteriorly, the sample was milled in a CMC FU1S milling machine using a spindle speed of 710 rev/min. With the sample cut out and milled, it was then taken to the Materials' Characterization Laboratory at Instituto Superior Técnico (IST), where it was placed into epoxy resin, sanded and polished (using diamond suspensions of 1 and 3 μm as well as colloidal silica), with the last two mentioned processes

being performed in a Struers equipment (model LaboPol-1), operating at 350 rev/min. To complete the preparation of the sample, the next and final step was to etch it by using Keller's reagent, that was previously prepared, in the same laboratory, which had the following composition: HNO_3 (2.5 mL), HCl (1.5 mL), HF (1 mL) and H_2O (95 mL).

After the preparation of the sample, an Olympus CK40M Compact Inverted Metallurgical Microscope equipped with an Olympus C3040-ADL Digital Camera was used in order to obtain a micrograph that would allow the microstructure of the base material to be analyzed.

The result that was obtained is shown in Figure 3.1 and represents the microstructure along the X-Z plane (see axis of Figure 3.6).

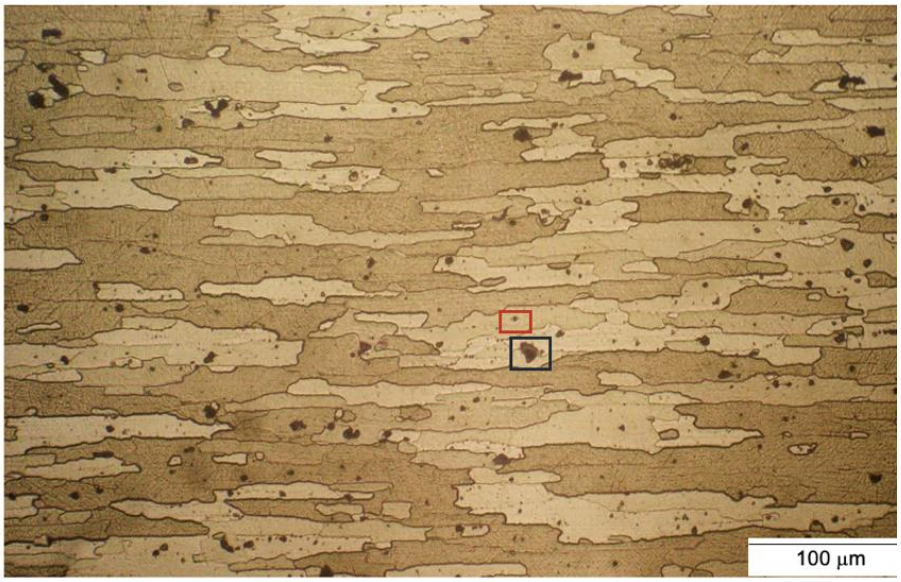

Figure 3.1- Micrograph obtained for a base material (AA7075-T651) sample.

As it can be seen by analyzing Figure 3.1, the base material presents elongated grains, oriented along the rolling direction, which was expected since the base material sample that was analyzed was, as mentioned previously, cut out along the rolling direction of the plates.

It is also possible to identify two distinct groups of precipitates taking into account their dimensions One of the finer precipitates is highlighted in red and an example of the coarser precipitates is highlighted in black. The micrograph shown in Figure 3.1 is not appropriate to measure the dimensions of the precipitates however, according to the literature, their sizes are expected to be comprehended between 10-50 nm and 50-100 nm respectively [60], [61]. There is no agreement in the literature as for their composition.

3.2. FSW Production

3.2.1. Equipment

All the friction stir welded joints produced within the scope of the thesis, were performed on an ESAB LEGIOTM FSW 3UL® numeric control machine, which is shown in Figure 3.2, that was available at the Manufacturing and Process Technology Laboratory at Instituto Superior Técnico.

As it can be seen by analyzing Figure 3.2, the machine contains built-in guidelines, a fixed framework with a worktable and a welding head capable of moving along the x, y and z axis.

The tilt angle can be manually set for any value ranging from 0 to 5 º by rotating the welding head. Some other welding parameters can be controlled by the machine by being set on the machine control panel. These welding parameters include the welding speed (which can go up onto 2 m/min), the dwell time (in seconds) and the plunge speed (in mm/s), both of which have been mentioned and described in the previous chapter of the dissertation, the tool force (axial force applied into the workpieces) and the tool rotational speed. In the production of the welds, a clockwise rotational speed was selected.

Concerning the welding process itself, the machine offers two possibilities: welding with position control (the machine regulates the applied force in order to ensure that the welding position, set by the operator on the control panel, remains the same throughout the welding process) and force control (the welding position is continuously being adjusted during the operation in order to guarantee that the applied axial force, set by the operator on the control panel, remains the same throughout the entire welding process).

The machine also includes an internal water refrigeration system, which is vital to avoid the equipment reaching high temperatures that can eventually jeopardize not only the tool service life but also, the quality of the welds.

The data acquisition system that is installed allows the operator to monitor in real time all the relevant process parameters, such as the torque, tool position (along the 3 axis) and welding speed, as well as recording these data for future analysis.

Figure 3.2- ESAB LEGIOTM 3UL- FSW equipment used in the development of the experimental work.

3.2.2. Clamping System

The clamping system is also an important part of the process as it is required to avoid warping of the workpieces. The clamping system that was used in the production of the welds, allows butt and lap joints to be welded, as long as the length of the workpieces is not superior to 350 mm and the width no longer than 200 mm. This clamping system (shown in Figure 3.3) is made of CK-45 carbon steel and has several clamping elements (including two bolted steel bars, one of them highlighted in Figure 3.3) that are connected to a base plate, machined in a way that allows all the necessary constraints to be applied to the workpieces.

Figure 3.3- Clamping system used in the production of the welds (one of the steel bars highlighted in red).

3.2.3. Tool Design

The tool design is one of the most important parameters in the friction stir welding process since it has a direct impact in both the material flow and resulting mechanical properties of the welds. In the production of the welds, the third version of the tool developed by Vilaça et al. [62]**,** at IST, designated iSTIRtool_v3, was used.

The tool is composed by 3 distinct parts: the tool body (responsible for supporting the mechanical stresses involved in the welding process and dissipating the resulting heat that is generated), the shoulder and the pin (which has a diameter of 5 mm).

The tool body is made of DIN Ck45 steel whereas both the shoulder and pin are made of AISI H13 tool steel. All the three aforementioned components are shown in Figure 3.4.

The aforementioned three module assembly design of the tool allows to easily obtain different geometrical combinations, efficiently replace the worn/damaged parts (instead of replacing the whole tool, the specific worn/damaged element can be replaced) and quickly set the appropriate pin offset length considering the material (and thickness) to be welded. The pin used to produce the welds had a conic shape, as shown in Figure 3.4 (the choice for such a type of pin was a result of the material being welded- AA7075-T651- as well as the plates thickness- 4 mm), and the pin offset length was set to 3.9 mm during the production of the welds, as this value allowed to have an optimized mixture of the SZ.

Figure 3.4- Tool (iSTIRtool_v3) used in the production of the welds: a) 3-part assembly; b) Conic Pin; c) Shoulder.

The pin offset length can easily be adjusted without the need of dismantling the tool from the FSW machine that is being used (which may lead to an increase in productivity), by unscrewing the shoulder fixation screws (Figure 3.5 b) (5)) and then screwing or unscrewing the shoulder in the tool body. Posteriorly, by aligning one of the various holes of the shoulder with one of the tool body's machined slots, the desired pin offset length can be set. This ability to adjust the pin offset length to the desired value results from the fact that the shoulder and pin are separately fastened to the tool body, with the rotation of the two joined elements being locked by the set of screws shown in Figure 3.5 b).

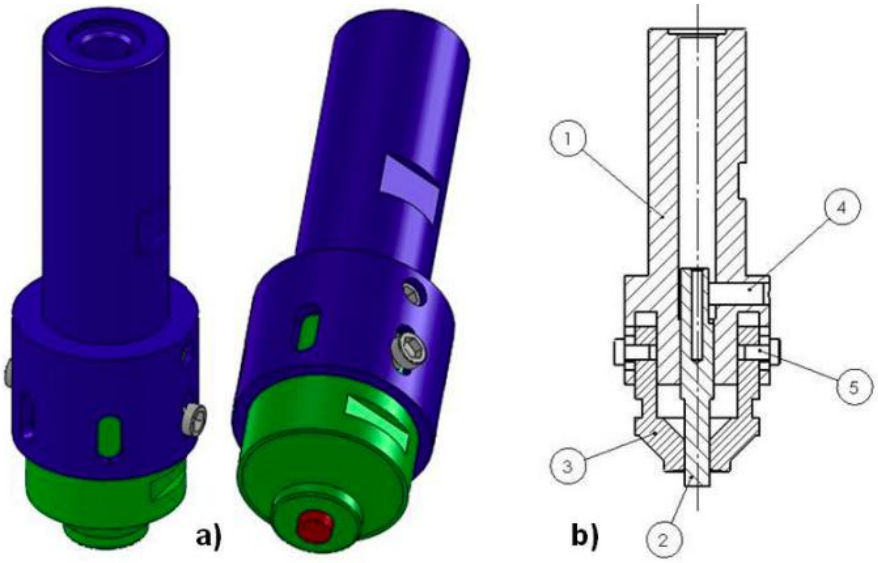

Figure 3.5- iSTIRtool_v3. A) 3D model view; b) cut view: (1) Tool body; (2) Pin; (3) Shoulder; (4) Pin Fixation Screw; (5) Shoulder Fixation Screw [62].

3.2.4. Welding Parameters

As previously mentioned, the main goal of the experimental work that was developed was to assess the mechanical behavior of friction stir butt welded joints, under different loading and temperatures conditions. To conduct this analysis, fatigue specimens needed to be manufactured.

For this purpose, a selection process that would allow to select an appropriate set, combination, of welding parameters was put into place. Considering the fact that obtaining the most optimal welding parameters for both the base material used (AA7075-T651) and the plate's thickness (4 mm) was not within the scope of thesis, the selection of an appropriate set of welding parameters was made through a trial-and-error process, which was divided in 3 phases. This selection process is thoroughly described next. The Taguchi Method is one of the optimization methods that should have been employed if the use of optimal welding parameters was strictly necessary.

Several welds were obtained, through the use of different sets of welding parameters and by the end of the selection process, one of them was considered to be the most appropriate. The range of welding parameters that were used in the production of those welds are listed in Table 3.3.

Table 3.3- Range of welding parameters used throughout the production of the welds.

Process Parameter	Range of Values (Units)
Initial Welding Position	$0.08 - 0.8\ (\mathrm{mm})$
Tool Force	$400 - 1000\ (\mathrm{kgf})$
Tool Rotational Speed	$800 - 2000\ (\mathrm{rev/min})$
Plunge Speed	$0.05 - 0.1\ (\mathrm{mm/s})$
Dwell Time	$3 - 10\ (\mathrm{s})$
Welding Speed	$4 - 15\ (\mathrm{cm/min})$
Tilt Angle	$1.5\ (°)$

- **Phase I**: **Visual Inspection-** Following the welding process, the welds were submitted to a visual inspection, during which their appearance was carefully observed. Although performing a visual inspection is not a reliable method to identify optimal or even appropriate welding parameters, since only a superficial evaluation of the weld is conducted, it allowed to immediately discard some combinations of welding parameters since some lead, for example, to excessive flash (the resulting heat inputs were too high) as shown and highlighted in Figure 3.6.

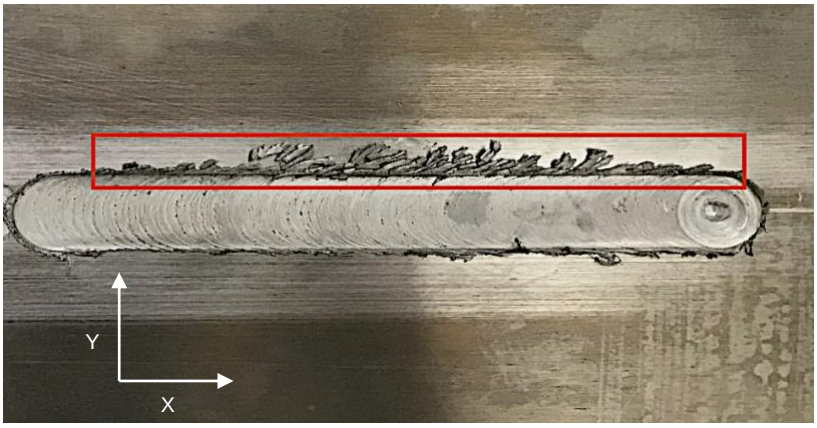

Figure 3.6- D5 weld, with its excessive flash highlighted.

- **Phase II: Preliminary Non-Destructive Testing-** From the initial set of welds, only a few passed the visual inspection stage and were therefore submitted to preliminary non-destructive tests (Eddy Current Testing) that were carried out at the Non-Destructive Testing Laboratory in the Nova School of Science and Technology.

With this inspection method, the electrical conductivity of the welds was analyzed in order to identify the presence of welding defects, since welding defects lead to a significant drop in the electrical conductivity of the welded joints. Therefore, whenever considerable reductions in this physical property were registered, it was possible to conclude that a certain weld contained a defect.

To illustrate the results obtained during the execution of these tests, the electrical conductivity profile registered at 4 and 10 mm from the start of a weld, designated D13, is shown in Figure 3.7. As it can be seen, at 4 mm from the start of the weld a considerable drop in the weld's electrical conductivity was recorded at the center of the weld (comparatively to the one registered in the same region at 10 mm from the start of the weld) which indicates the presence of a welding defect in this region. The X axis corresponds to the probe displacement along the Y axis of the setup used to carry out this tests (see Figure 3.9).

It is important to mention that in the analysis of the preliminary non-destructive testing results only the real component of the electrical impedance was taken into account, which corresponds to the relative variation of the electrical conductivity. More information regarding the equipment, process and testing parameters can be found under the next section of the current chapter: Eddy Current Testing (Non-Destructive Testing).

In conclusion, the results obtained during this phase allowed to identify and discard the sets of welding parameters that lead to welding defects which could not have been identified by visual inspection. Following this phase, 4 sets of welding parameters were still viable options to use in order to produce the fatigue specimens.

The electrical conductivity is a property that is inversely proportional to the hardness of the material, as found by Oliveira et al. [63] which work focused on establishing a correlation between this two properties. It can be seen, through the analysis of Figure 3.7, that the D13 sample possesses an electrical conductivity profile with an "inverted W-shape" distribution, which is in accordance with the W-shaped hardness profile of the sample (which is thoroughly analyzed in the next chapter of this dissertation).

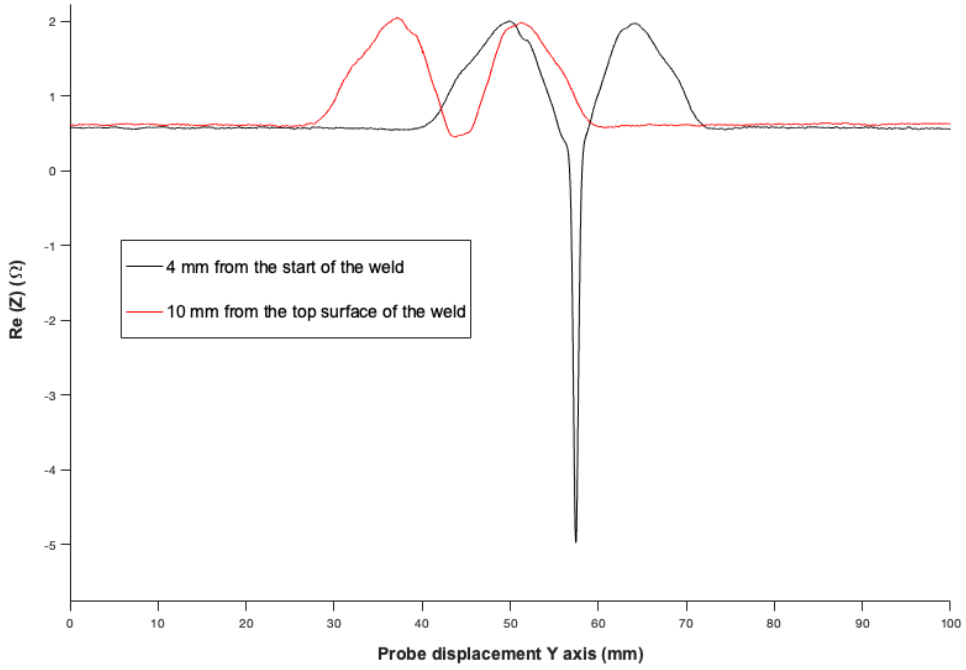

Figure 3.7- Electrical Conductivity profile of the D13 weld at 4 and 10 mm from the start of the weld.

- **Phase III: Preliminary Uniaxial Quasi-Static Tensile Tests-** The last stage of the selection process was performing preliminary uniaxial quasi-static tensile tests to determine the strength of the welds. From the 4 remaining welds, several tensile specimens were cut out, transversally to the welding direction, in order to carry out the aforementioned tests. Following the results, a set of welding parameters was selected, corresponding to a weld from now on designated as L1.

  In Figure 3.8, the L1 tensile specimens are shown. Since the goal of this preliminary tests was only to identify the weld with the highest strength, the geometry was not an important factor to take into account and therefore, the specimens' geometry is not up to the norms. By analyzing Figure 3.8, it is possible to see that the test specimens have a rectangular cross section, with equals gauging and griping areas. Regarding the obtained results, for the specimens shown in Figure 3.8, the average measured UTS was approximately 365 MPa (with a standard deviation of 14.8 MPa) which represents approximately 64% of the base material UTS (which is 572 MPa, according to Table 3.2).

  More information regarding the equipment and setup used to perform the tests is provided in a further section of the current chapter: Uniaxial Quasi-Static Tensile Testing.

The welding parameters used to produce the L1 weld are listed in Table 3.4. Different welds were posteriorly produced resorting to those welding parameter (those welds are designated as L2, L3, L4, L5, L6 L7 and L8).

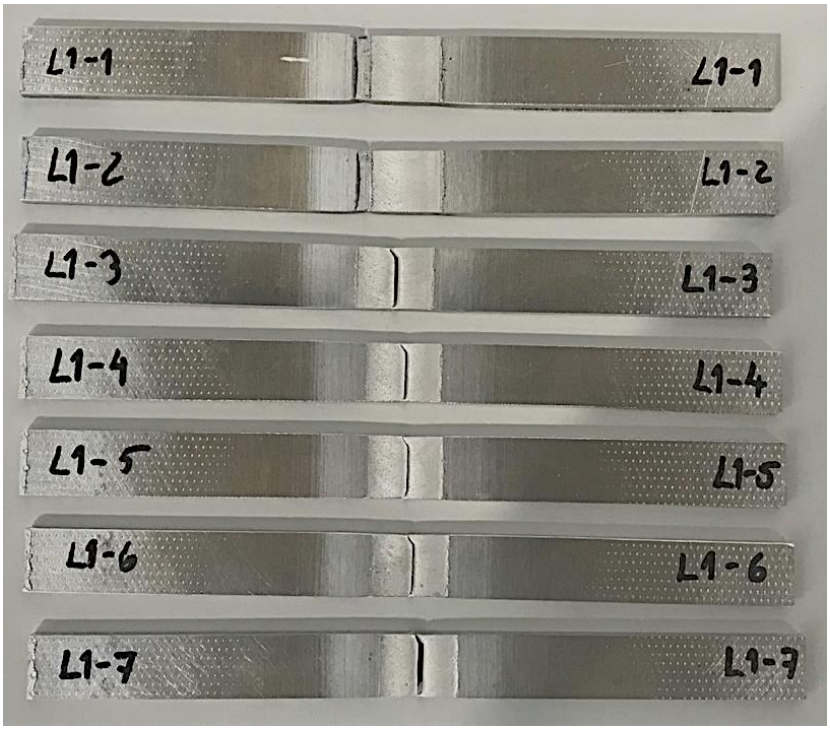

Figure 3.8- Tensile specimens obtained from the L1 weld, used in the preliminary uniaxial quasi-static tensile tests.

Table 3.4- Welding parameters used to produce the L1, L2, L3, L4, L5, L7, L7 and L8 welds.

Process Parameter	Value (Units)
Initial Welding Position	0.8 (mm)
Tool Force	950 (kgf)
Tool Rotational Speed	1000 (rev/min)
Plunge Speed	0.1 (mm/s)
Dwell Time	4 (s)
Welding Speed	8 (cm/min)
Tilt Angle	1.5 (°)

3.3. Eddy Current Testing (Non-Destructive Testing)

The welds from which fatigue specimens would be manufactured from, as well as the welds that passed the first phase of the selection process that was previously described, were taken to the Non-Destructive Testing Laboratory located in the Department of Mechanical and Industrial Engineering (DEMI) of the Nova School of Science and Technology, where they were submitted to non-destructive tests in order to assess the existence of welding defects.

As for the specific non-destructive inspection method, Eddy Current Testing was selected as it was suitable considering the material used in the experimental work: an aluminum alloy.

The Eddy Current Testing technique is based on the electromagnetic induction of the materials that constitute the specimens being analyzed (in this work, the welded plates). An alternating current flowing through the coil, located inside a probe leads to an alternating magnetic field. As the probe is brought closer to the plates, the alternating magnetic field, according to Lenz's Law, induces an Eddy Current into the material. By its turn, as the Eddy Current goes through the material, it generates a magnetic field, that will interact with the magnetic field that surrounds the coil, through mutual inductance.

Any material defect, irregularity or thickness change will affect the flow of Eddy Current resulting in a change of the magnetic field, thus causing a change in the electrical impedance of the coil. The impedance analyzer will then plot the impedance amplitude changes, which can then be analyzed in order to identify welding defects.

Although the specific type of welding defect cannot be identified through this inspection method, their existence can be determined by analyzing the changes in electrical conductivity along the welds (only the real component of the electrical impedance was taken into account, which corresponds to the relative variation of the electrical conductivity, as it occurred in the preliminary non-destructive tests).

As it was mentioned in the previous chapter, along the different metallographic regions of the welds there are some differences regarding the grain size. The grain size is one of the factors that influences the Eddy Current flow: the lower the grain size, the higher the amount of grain boundaries, which leads to a lower electrical conductivity. The contrary is also true, with higher grain size leading to an increase in the electrical conductivity of the weld as a result of the lower amount of grain boundaries.

Regarding the equipment, a probe, operating at 1.1 MHz, 6º and with a gain of 70 dB combined with a NORTEC 500C impedance analyzer, were used in the tests. The setup that was used to perform the Eddy Current tests is shown in Figure 3.9. These testing parameters were also employed in the preliminary tests that were performed. The probe had the capacity to move in two perpendicular directions: transversally to the welds, to evaluate the presence of defects along the different microstructural regions of the welds (X direction) and along the welding direction (Y

direction) in order to evaluate the presence of defects along the welded joint. The inspection depth was 0.1 mm, as a result of the testing frequency established.

Another important variable that need to be considered is related to the distance travelled by the probe from the weld center to the sides (Y direction) and between each probe pass (X axis). In the preliminary non-destructive tests, the distance between each probe pass was set to 1 mm and the distance travelled by the probe between each pass was adjusted to 50 mm (to both sides of the weld center, meaning that for each probe pass, the electrical conductivity was analyzed for a total of 100 mm). The only difference relatively to the tests performed on the welds obtained with the L1 weld welding parameters' was the distance set between each probe pass: it was set to 2 mm.

The same equipment and procedure was followed in order to carry out the preliminary non-destructive tests.

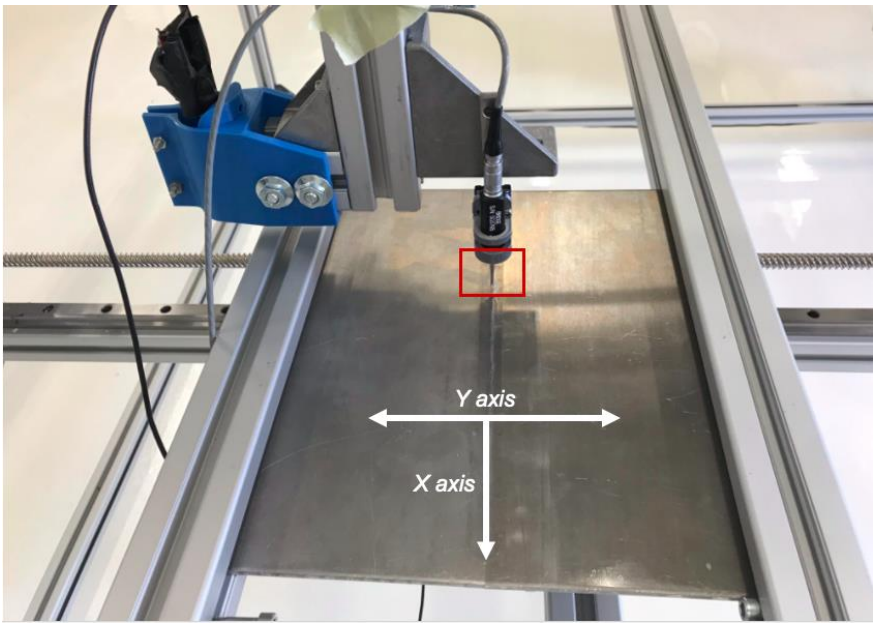

Figure 3.9- Eddy Current Testing setup with the testing probe highlighted in red.

As it can be seen by analyzing Figure 3.9, the welded plates were turned upside down with the lower surface of the welds being closer to the probe. This was done in order to identify root defects more easily, which are a very common type of welding defect.

3.4. Hardness Testing

The mechanical strength of a weld, which is a result of the thermal and mechanical changes that the material undergoes during the FSW process, can be assessed, in relative terms, through the execution of hardness tests. Therefore, in order to depict the mechanical and structural properties of the welded joints, Vickers hardness tests were performed.

Two samples were prepared, following the same procedure that was used in order to obtain the base material sample (see Section 3.1.2): one sample was obtained from the L1 weld and another one obtained from a weld (D13), for which welding defects were detected during the preliminary non-destructive tests that were carried out in the scope of the selection process that was previously described. The main goal was to study the impact caused by this welding defect over the hardness profile of the welds. For each one of the samples, indentations were made along 3 different straight lines: at 0.5 mm from the top surface of the weld, at the mid-thickness of the samples (2 mm from the top surface of the weld) and at 3.5 mm from the top surface of the weld, with a load of 2 kgf and an indentation time of 10 seconds.

Following the tests, the diagonals of each indentation was measured through the use of the machine´s guidelines with the Vickers hardness value being automatically calculated by the equipment and expressed in HV. All the hardness tests were performed following the ISO 6507-2 standard, in a Mitutoyo Hardness Tester (model AVK-C2), which is shown in Figure 3.10. Regarding the spacing between each indentation, from the weld center up to 2.5 mm, on both sides, the interval was set to 0.5 mm. From there, to the edge of the samples, the space between each indentation was set to 1 mm. The schematic representation of the indentations is shown in Figure 3.11.

Figure 3.10- Equipment used to perform the hardness tests (Mitutoyo AVK-C2 Hardness Tester).

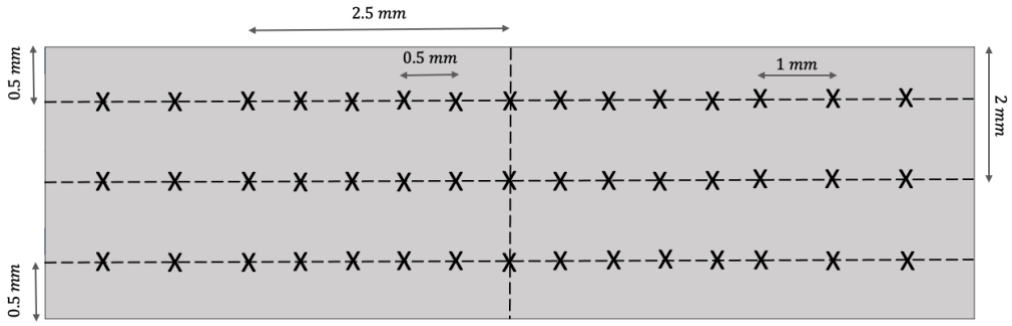

Figure 3.11- Schematic representation of the plan for the indentations, along the thickness of the samples, of the hardness tests (front view of the sample).

3.5. Uniaxial Quasi-Static Tensile Testing

Uniaxial quasi-static tensile tests were performed in order to assess the tensile properties of the welded joints. For this purpose, tensile specimens with a thickness of 4 mm and with the geometry shown in Figure 3.13 were produced. These specimens were manufactured at the Núcleo de Oficinas (NOF), located at IST, from the welded plates, transversally to the welding direction and were then taken to the Experimental Mechanics' Laboratory, at IST, in order to perform the aforementioned tests.

Unlike the tensile specimens used for the assessment of the most appropriate welding parameters, as it can be seen by analyzing Figure 3.12, the tensile specimens had a dog-bone shape with a gauging length of 80 mm, a gauging width of 9.5 mm as well as a gripping length of 40 mm (on both ends of the specimen) as well as a gripping width of 16 mm.

Concerning the designation of the tensile specimens, the designation includes the number of the weld from which it was manufactured as well as an indication regarding its location relatively to the start of the weld. For example, the specimen L4-1 was taken from the weld L4 close to the start of the weld whereas the specimen L4-10 was taken from the same weld, but closer to the end of the weld.

This designation system was put into place since the welding conditions at the beginning and at the end of a weld can be quite different, which has an impact in its mechanical strength. Therefore, the purpose was to be able to establish and evaluate the correlation between the tensile strength of a specimen and its location in regard to the start/end of the weld.

The uniaxial quasi-static tensile tests were carried out at room temperature with a displacement rate speed of 5 mm/min.

The equipment used for this purpose was an Instron model 3369, with a load cell of 50 kN.

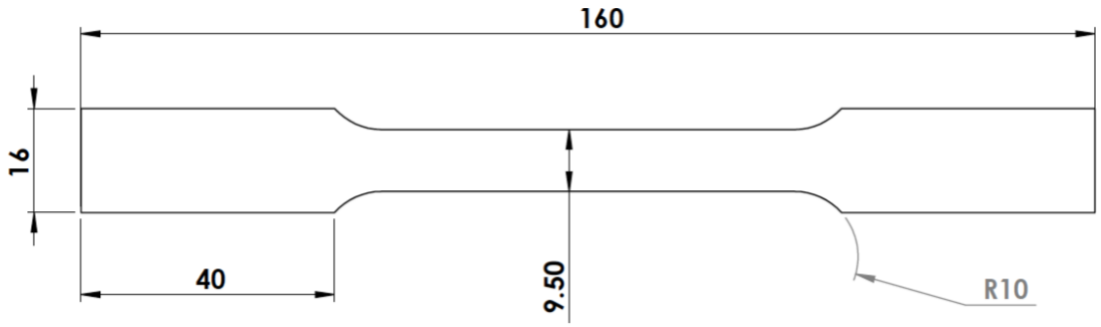

Figure 3.12- Geometry and dimensions of the uniaxial quasi-static tensile tests' specimens (all dimensions in millimeters).

3.6. Fatigue Testing

Fatigue Testing was carried out on a servo hydraulic Instron machine (model P8502, shown in Figure 3.14) equipped with a load cell of 10 kN. The specimens used for these tests were in all aspects equals to the ones used in the uniaxial quasi-static tensile tests (see Figure 3.13)

The tests were performed at two different temperatures: room temperature and 150 ºC. The use of the latter is related to the fact that at this temperature the strength of the material is significantly, lower relatively to the one exhibited at room temperature (as reported by Dalai et al. [64]). For those tests an Instron furnace equipped with a temperature controller was used in order to control the testing temperature and to ensure that the fatigue tests were performed, entirely, at the desired temperature.

The furnace and temperature controller mentioned can be seen in Figure 3.14, in which the setup used for the tests carried out at 150 ºC can be observed.

All the fatigue tests were carried out until the fatigue specimens fractured or until the run-out limit (established at $2x10^6$ cycles) was attained. In those situations, the tests were terminated, and a scenario of infinite life was considered.

The fatigue tests were executed under a constant amplitude loading regime, following a sinusoidal function, with frequencies of 8, 10 and 12 Hz, with the first two being used in tests carried out at high temperature (150 ºC) and the letter for the fatigue tests carried out at room temperature. Two stress ratios (0.5 and 0.05) were applied to the specimens.
Lastly, in order to wrap up the experimental work, following the fatigue tests, an examination of the fracture surface of some fatigue specimens was performed with the purpose of identifying and analyzing, in more detail, the fatigue crack initiation and propagation mechanisms as well as the failure modes that lead to the fracture of those specimens.
In order to accomplish the aforementioned analysis, the fractured specimens were taken to the SEM (Scanning Electron Microscope).

Figure 3.13- Fatigue equipment used in the execution of the fatigue tests (Instron 8502).

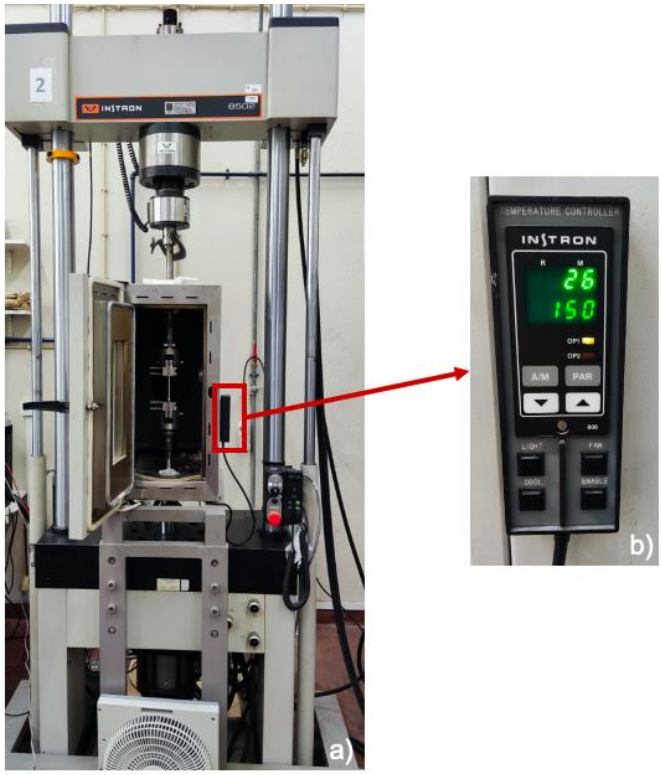

Figure 3.14- a) Setup used to perform the fatigue tests at 150 ºC; b) Temperature Controller.

Chapter 4

Results and Analysis

As the title of the chapter suggests, the results that were obtained during the experimental work that was developed within the scope of this thesis are hereby reported and analyzed thoroughly. As mentioned previously, the uniaxial quasi-static tensile and fatigue tests were conducted on specimens that were produced from friction stir welds obtained with the L1 welding parameters (see Table 3.4), since those were considered the most suitable following the selection process that was presented in the previous chapter. Taking that into account, the focus of the metallographic analysis and hardness tests was on a sample obtained from the L1 weld.

Nevertheless, throughout those first sections, a comparison was made with the results obtained for a sample of the D13 weld, since while executing non-destructive tests, a welding defect was detected in this weld. This work methodology was followed in order to assess the effect of both the use of different welding parameters and, more importantly, the presence of a welding defect over the hardness profile and microstructure of this type of welds.

When possible, and considered opportune, the obtained results are compared to the ones obtained by other researchers.

4.1. Metallographic Analysis of the Welds

In the current section of this chapter, two different types of metallographic analysis will be conducted, in the two aforementioned samples: a macrographic analysis, intended to identify the differences caused by the use of different welding parameters in the morphology of the joined area and identify, if they exist, macrostructural defects; and a micrographic analysis in order to try to identify and analyze, in more detail, the different welding regions (HAZ, TMAZ, SZ and base material, all of which have been previously described in the previous chapter).

The goal of the latter is also to observe the welding defect that was detected in the D13 weld.

In order to conduct the metallographic analysis that was proposed, samples from the L1 and D13 welds needed to be prepared. The experimental procedure followed was, in all aspects, identical to the one that was followed to obtain the base material sample and analyze its microstructure. This procedure can be consulted in the previous chapter under the section (3.1. Base Material Characterization).

Both samples were cut out at a distance of 4 mm from the start of the respective weld.

The macrographs obtained, by following the aforementioned procedure, for the L1 and D13 samples, are shown in Figure 4.1 a) and b) respectively, while in Figures 4.2 and 4.3 micrographs of certain regions of interest, from both samples, are presented.

Figure 4.1- Macrographs obtained for the a) L1 weld sample and b) D13 weld sample.

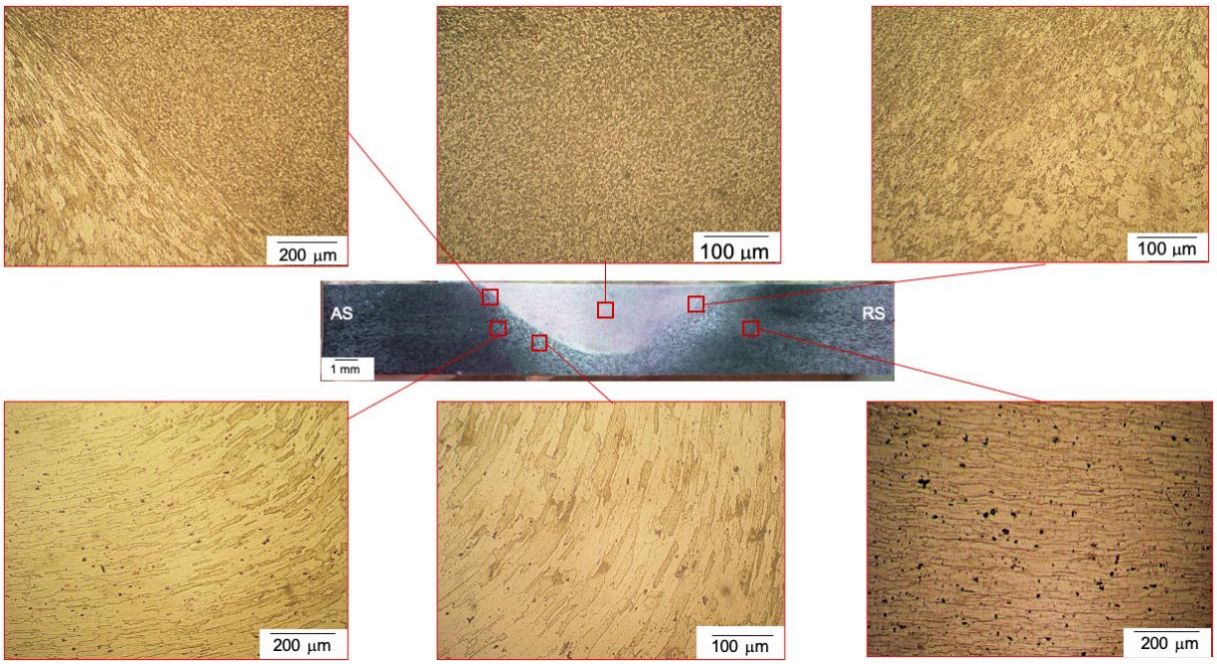

Figure 4.2- Macrograph and micrographs obtained for the L1 sample.

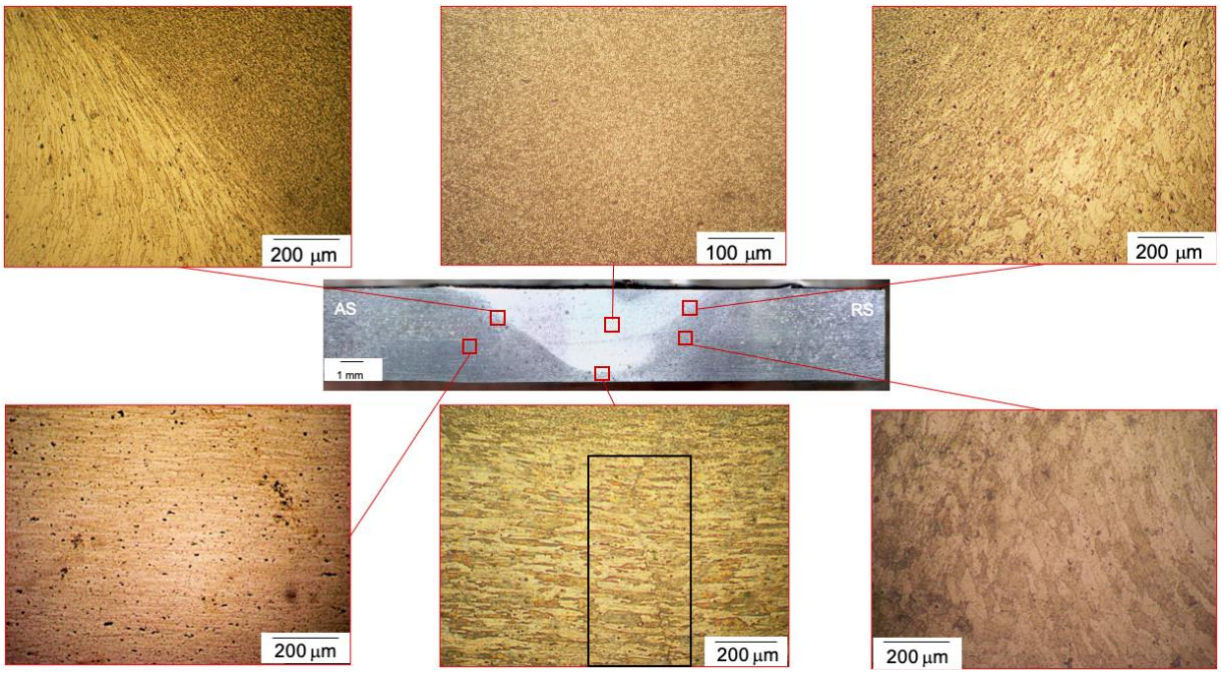

Figure 4.3- Macrograph and micrographs obtained for the D13 sample.

Through the analysis of Figure 4.2 and 4.3, in which the micrographs of both samples can be observed, it is possible to identify all the typical microstructural regions of welds obtained by FSW: SZ, TMAZ, HAZ and base material. This identification can also be done in Figure 4.1, by taking into account the different color tones and grain morphology that can be detected along the samples' macrographs. However, the transition from the HAZ to the base material is not easily recognizable trough the examination of Figure 4.1 a) and b) but is readily distinguished when comparing the micrographs obtained for both regions.

The SZ appears in the center of both macrographs in a clearer color tone (whitish). In this region, in both samples, a fine, homogeneous, equiaxed microstructure can be encountered as a result of the dynamic recrystallization that the material undergoes caused by the intense plastic deformation and high temperatures registered in this specific region. It is also possible to perceive that a significant dissolution of precipitates has occurred in the SZ comparatively to the HAZ and base material, which will negatively impact its hardness, as it will be possible to observe in the next section of this chapter.

When comparing the micrographs from both samples, obtained for this region, a difference in the SZ microstructure can be identified: the L1 sample has a lower grain size comparatively to the one presented by the D13 weld. This observation can be explained by the different heat inputs that were used in order to produce the welds: the L1 weld was obtained with a lower heat input, thus the grain size of the stir zone is lower and is in accordance with the work developed by Ahmed et al. [24], who found out that for the same tool rotational speed, higher welding speeds lead to lower grain sizes, in the SZ of AA7075 friction stir welds.

Additionally, through the analysis of the macrographs, it can be seen that the SZ in both samples are different: for the D13 sample, this regions extends until close to the root of the weld, whereas the SZ of the L1 sample is shorter. The fact that different welding parameters were used to produce the L1 and D13 weld, which led to different heat inputs and thus to a different flow of temperature in each weld, is a possible explanation for this observation.

Regarding the TMAZ, in both Figure 4.1 a) and b), it can be identified as being the closest region to the stir zone, with a slightly darker color tone and a different grain morphology. When observing the micrographs corresponding to the TMAZ, it is possible to identify the highly deformed grain structure that characterizes this region. This highly deformed microstructure is more evident in the interface between the TMAZ and the SZ.
Another important aspect worth mentioning is that the micrographs also allow to verify that the transition between the TMAZ and the SZ is smoother and harder to detect at the retreating side of the weld, which was also expected, as mentioned in the previous chapter of this dissertation, as a consequence of the less extreme material flow that occurs in that side of the weld, which is due to the opposite directions presented by the tool rotational and travel speed [65].

As for the HAZ, it can be identified as being the region with a darker color tone and different grain morphology comparatively to the one presented by the TMAZ, in both macrographs. Regarding its microstructure, the grain size is higher when compared to the one found in the aforementioned regions and more strengthening precipitates are encountered. An immediate similarity can be found between the grain structure of the HAZ and the one of the base material (see Figure 3.1): elongated grains, oriented along the rolling direction.

As it was mentioned in the introduction of the present chapter, one of the main purposes of conducting a metallographic analysis in a sample cut out from the D13 weld, was to perceive the differences in microstructure caused by the presence of its welding defect. By analyzing the macrographs that were obtained for the samples that were cut out transversally from the L1 and D13 welds (Figure 4.1), no macrostructural defects could be identified.

However, the defect becomes evident through the analysis of Figure 4.3. Regarding its classification, it is a root defect of the Kissing Bond type with visible traces of the two original aluminum plates that were used to obtain the D13 weld. More detailed information regarding this type of defect can be consulted in the second chapter (see Table 2.5).

Through the analysis of Figure 4.3, it can be seen that this defect is located at the root of the weld and then fades towards the stir zone. As the Kissing Bond evolves in the direction of the SZ, at first, a slight deviation towards the advancing side of the weld occurs, with this deviation posteriorly, closer to the SZ, inverting its direction towards the retreating side of the weld. Such a phenomenon is a result of the plastic deformation that the material undergoes in this region and has been reported by other authors [53].

4.2. Hardness Testing

Following the metallographic analysis, Vickers hardness tests were carried out in the L1 and D13 samples at 0.5, 2 and 3.5 mm from the upper surface of the welds, with the results obtained for both samples being presented in Figures 4.4, 4.5 and 4.6.

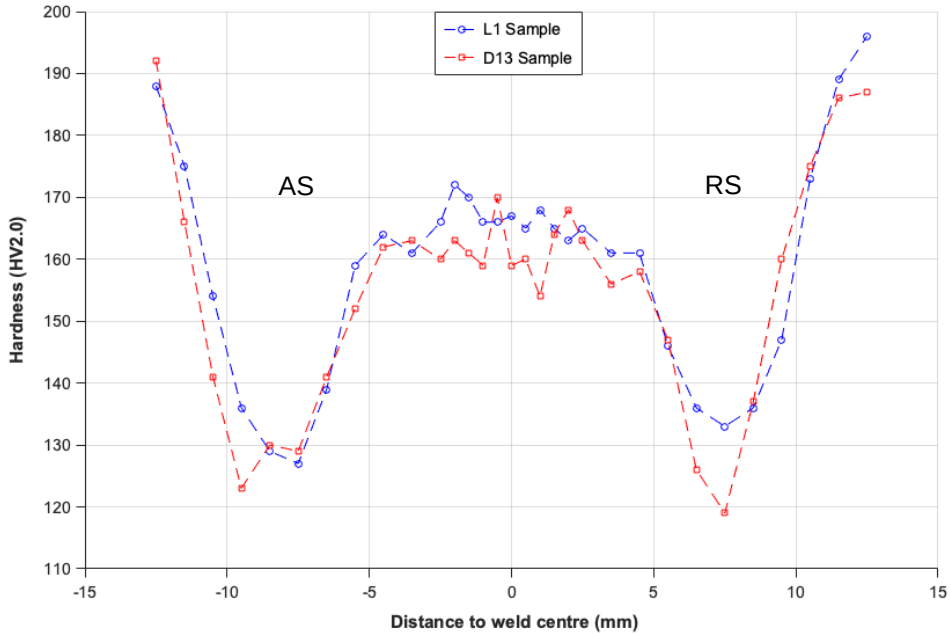

Figure 4.4- Hardness profiles at 0.5 mm from the top surface of the L1 and D13 samples.

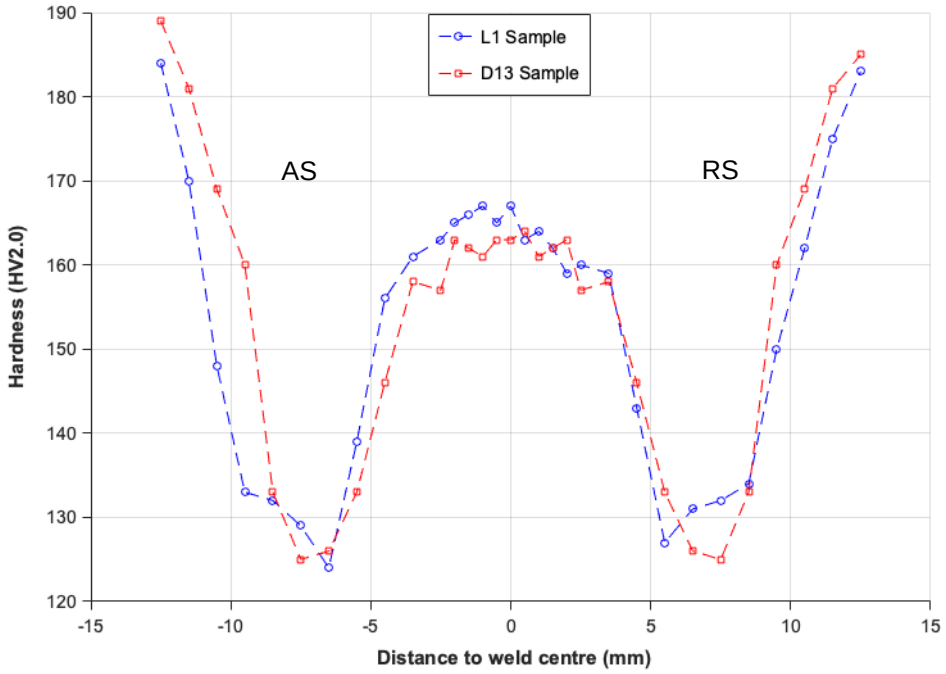

Figure 4.5- Hardness profiles at 2 mm from the top surface of the L1 and D13 samples.

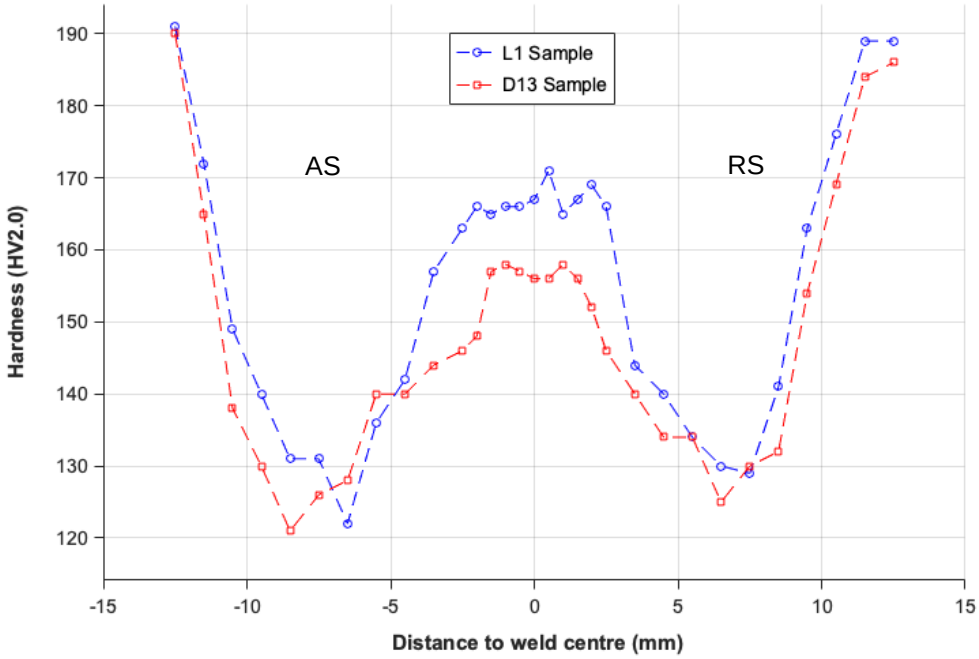

Figure 4.6- Hardness profiles at 3.5 mm from the top surface of the L1 and D13 samples.

For both samples, a “W-shaped” hardness profile can be identified for each testing depth, which goes along with the findings of Çevik et al. [66] and Sun et al. [3]. Such a hardness distribution was expected as a result of the base material being a heat treatable aluminum alloy. The hardness values are, in both samples, and along the 3 sets of measurements analyzed, inferior to the hardness of the base material which is reached at a distance of around 12 mm from the weld centre.

Through the analysis of the results that were obtained from the L1 sample, it is possible to identify a plateau surrounding the weld center, which extents up to approximately 4 mm, on both sides, where the hardness remains approximately constant (around 160 to 170 HV), with this value corresponding to 83-90 % of the base material hardness, which is in accordance with the findings of Ahmed et al. [24], who obtained similar results for AA7075 (in the T6 condition) friction stir welds.

This hardness uniformity is a result of the homogeneous microstructure found in the stir zone, which has been discussed previously. The same observations can be made from the results obtained from the D13 sample.

Although possessing a microstructure composed of fine grains, the fact that the dissolution of precipitates has occurred in the SZ, as verified in the previous section, justifies the lower hardness values obtained in this region comparatively to the base material.

By analyzing Figures 4.4, 4.5 and 4.6, it is possible to verify that, for both samples, the hardness values decrease progressively along the TMAZ (as the distance to the weld center increases) with the absolute minimum hardness values being registered, primarily, in the advancing side of

the weld and more specifically, at the interface between the HAZ and the TMAZ (for both sides of the weld, the lowest hardness values are found at this interface). Similar results were obtained by Balasubramanian et al. [61]. According to Pankade et al. [67], who analyzed the hardness profile obtained for AA7075-T6 friction stir welds and obtained identical results, such an observation can be explained by the precipitate over-aging and consequent coarsening that occurs in this region, as a result of the thermal cycle that the material undergoes.
Comparatively to the base material, this absolute minimum hardness value corresponds to a decrease of roughly 40 %, on average, which is once again, in line with the results obtained by Ahmed et al. [24].

Previous studies, as the ones developed by Selvarajan & Balasubramanian [68] and Tan et al. [69], which have focused on evaluating the causality between the hardness of friction stir welds of aluminum alloys and the resulting tensile fracture locations, found that the regions that presented lower hardness were more susceptible to those type of fractures.
Taking this into account, the fracture is expected to occur, during the execution of the uniaxial quasi-static tensile tests, in the absence of welding defects, in the TMAZ, more specifically at the interface between the HAZ and TMAZ.

As for the fatigue tests, no conclusion of the sorts can be withdrawn since other factors need to be considered.

Along the HAZ of both welds, the increase in distance to the weld centre is accompanied by a hardness increase since, gradually, lower temperatures and cooling rates are attained as the distance to the base material decreases.

As mentioned previously, in Figures 4.4, 4.5 and 4.6 the hardness profiles of the L1 and D13 welds are compared to each other and it can be noticed that the values registered for the D13 sample are, generally, lower, especially in the stir zone. Such trend can be explained by the lower grain size found at this region in the L1 sample, as discussed in the previous section of this chapter.

This trend becomes more evident near the bottom surface of the welds (testing depth of 3.5 mm- Figure 4.6) where the difference in hardness takes the highest values, with a maximum difference of approximately 15 HV being registered.
This major difference can be explained by the different temperature flow that are a result of the use of different heat inputs, as mentioned earlier on in this chapter.

The effect of the Kissing Bond defect that was detected in the D13 sample, over the hardness profile, was not noticeable. It was expected to lead to a punctual and significant decrease in the hardness of the sample, in the region where the defect was located. However, as it can be seen in Figure 4.6, the hardness registered in that region (root of the weld), in the D13 sample extends to all the stir zone, in the form of a plateau, which is not consistent with the presence of a welding defect.

4.3. Uniaxial Quasi-Static Tensile Testing

The next step of the experimental work that was developed was to perform uniaxial quasi-static tensile tests in the specimens that were manufactured from the L2, L3, L4, L5, L7 and L8 welds.

The specimens that were tested were selected randomly in order to have a representative sample with the weld they were manufactured from as well as their position relatively to the beginning/ending of the weld being disregarded during the selection process.

The Load-Displacement curves obtained for each tested specimen are shown in Figure 4.7 and the results of the uniaxial quasi-static tensile tests are summarized in Table 4.1. In this table the actual dimensions, the yield and ultimate tensile strength of each specimen are reported.

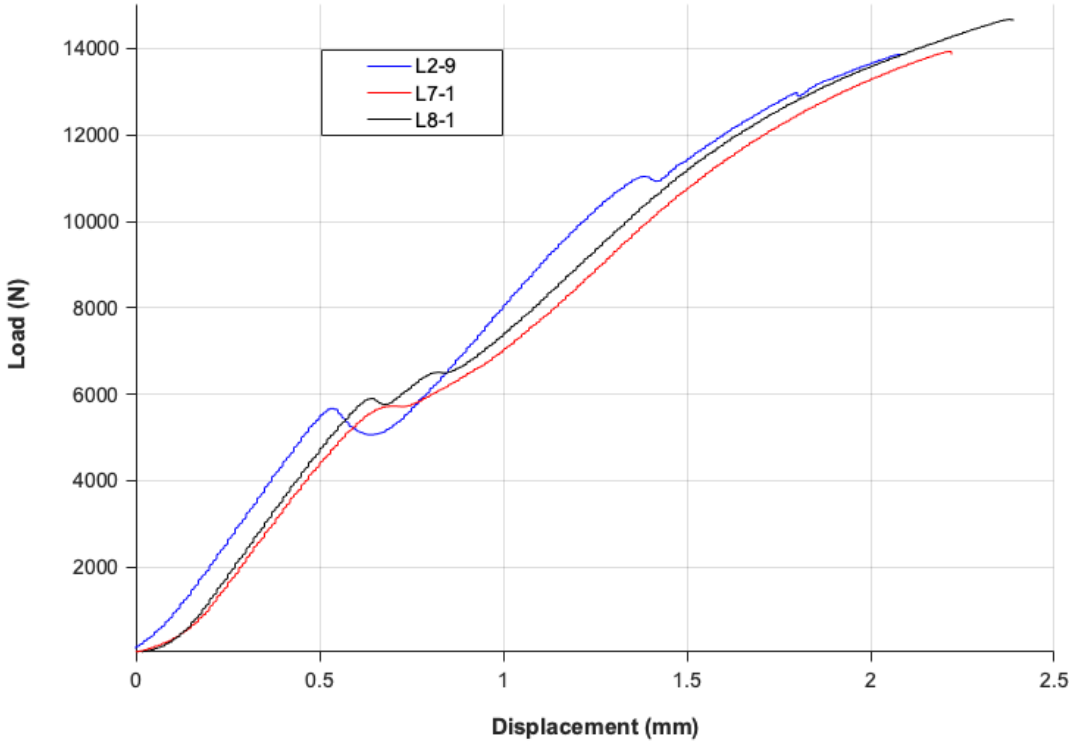

Figure 4.7- Load-Displacement curves obtained for the L2-9, L7-1 and L8-1 specimens.

Table 4.1- Uniaxial quasi-static tensile testing results.

Specimen	Width (mm)	Thickness (mm)	Yield Strength (MPa)	UTS (MPa)
L2 - 9	9.6	4.1	≈ 305	352.7
L7 - 1	9.6	4.1	≈ 305	353.8
L8 - 1	9.6	4.1	≈ 305	372.7
Standard Deviation (MPa)			0	11.3

For all the specimens, a plateau is visible in Figure 4.7, around 5000-6000 N, following which, the load value slightly decreases before continuing to increase, as expected in these type of tests. Such a phenomenon could be a result of the possible alignment of the specimens relatively to the fixture system at this load level, during the execution of the tests.

Through the analysis of Table 4.1, it is possible to see that the three tested specimens possess the same yield strength, around 305 MPa. Comparatively to the base material, which has a yield strength of 503 MPa, as listed in Table 3.2, this value corresponds to a decrease of approximately 39%. In order to obtain this value, 12 000 N was considered to be the load that resulted in the material yielding, since from that point onwards it is possible to perceive a change in the slope of the Load-Displacement curves presented in Figure 4.7.

The ultimate tensile strength (UTS) registered was very similar with an average of 360 MPa and a standard deviation of 11.3 MPa. Such a value corresponds to a joint efficiency of approximately 63%, meaning that the FSW process led to a decrease of 37% of the ultimate tensile strength of the base material (572 MPa).

Both observations (regarding the yield and UTS of the specimens) are in accordance with the work developed by several authors: Balasubramanian et al. [61], Çevik et al. [66] and Linton & Ripley [70], who obtained similar results in tensile tests carried out in AA7075-T651 specimens obtained from friction stir welds.

Through the analysis of the Load-Displacement curves presented in Figure 4.7, it is possible to observe that necking did not occur for any of the specimens and that they all present a very similar, ductile behavior.

4.4. Fracture Surface Analysis of Tensile Specimens

Table 4.2 provides detailed information regarding the location of the tensile fractures (initial location and development direction) as well as the type of fracture observed for each specimen. The fracture surfaces can be analyzed in Figure 4.8.

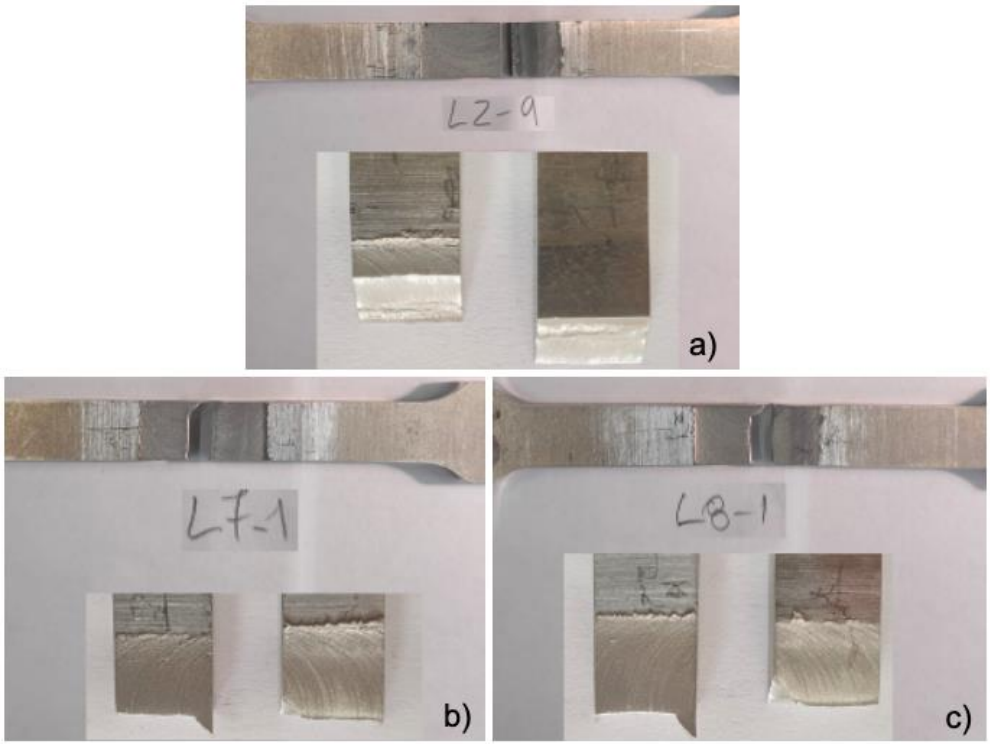

Figure 4.8- Fracture surface of the specimens used in the uniaxial quasi-static tensile tests.

Table 4.2- Tensile specimens' fracture location and correspondent type of fracture.

Specimen	Initial fracture location and development direction.	Type of Fracture
L2 - 9 (Figure. 4.8 a)	The fracture initiates at the bottom surface of the specimen, at the root of the weld, and posteriorly evolves towards the HAZ.	Ductile with the fracture occurring at 45º relatively to the applied stress.
L7 - 1, L8 -1 (Figure 4.8 b and c))	The fracture initiated at the bottom surface of the specimens, at the root of the weld, and then evolved towards its center, through the middle of the weld.	Ductile with the fracture occurring perpendicularly to the applied stress.

Concerning the tensile fractures, as it can be seen by analyzing Figure 4.8 and Table 4.2, for the L2-9 specimen, the fracture and correspondent propagation mechanism occurred according to a 45º plane and started at the root of the weld and then evolved towards the region where the lowest

hardness values were registered (TMAZ/HAZ interface), as predicted during the analysis of the hardness profiles.

For the L7-1 and L8-1 specimens, the tensile fracture occurred perpendicularly (according to a 90º plane) to the applied stress as suggested by Figure 4.8 b) and c) respectively, with this mechanism also starting at the root of the weld.

The fact that the fracture occurred from the root of the weld for all the specimens is not supported by the results obtained through the non-destructive tests that were executed.
A weaker zone, located at the root of the weld, resultant from an improper/insufficient material mixing during the welding process might be the reason behind this observation, with the extension of this area dictating the direction along which the fracture evolved along the specimens.

4.5. Fatigue Testing

The results obtained by executing all the fatigue tests are summarized in Table 4.4, where information regarding the maximum stress, stress range, testing frequency and the number of cycles of each test is presented.

Additionally, the results obtained from the tests carried out at 23 ºC are presented in the form of S-N curves in Figure 4.9 and Figure 4.10, while the results obtained for the tests carried out at 150 ºC are presented in the same format in Figure 4.11 and Figure 4.12.

In order to obtain the aforementioned curves, for each set of results, a logarithmic regression was formulated (since it was the one that best fitted the available points) with the purpose of correlating the results obtained in a range of stress values with the number of cycles registered until failure of the specimens occurred (or the run-out limit was attained). A logarithmic scale was employed in the representation of those curves, in order to facilitate their analysis.

The logarithmic regression that was considered is described by the following expression:

$$\mathrm{N} = \mathrm{m} \times \ln(\sigma) + \mathrm{K}_0 \tag{4.1}$$

where N represents the number of cycles, σ represents the maximum stress (for Figures 4.9 and 4.11) or the stress range (for Figures 4.10 and 4.12), while m and K_0 are constants that resulted from the fatigue tests that were carried out: the ordinate value at the origin and the slope of the logarithmic regression lines used in the S-N curves, respectively.
The values of m and K_0 obtained for each curve are listed in Table 4.3, with r^2 representing the correlation coefficient.

Table 4.3- K_0, m and r^2 values of the curves presented in Figures 4.9, 4.10, 4.11, 4.12.

	Temperature	Stress Ratio	m	$\mathbf{K_0}$	$\mathbf{r^2}$
σ_{max}	23 ºC (Figure 4.9)	0.05	−11.54	240.6	0.44
		0.5	−1.74	158.9	0.11
	150 ºC (Figure 4.11)	0.05	−12	251.2	0.95
		0.5	−2.8	156.9	0.007
$\Delta\sigma$	23 ºC (Figure 4.10)	0.05	−10.98	228.6	0.44
		0.5	−0.87	79.5	0.11
	150 ºC (Figure 4.12)	0.05	−11.4	238.7	0.95
		0.5	−1.4	78.5	0.007

Through the analysis of Table 4.3, it is possible to observe that the correlation coefficient could still be improved. This can be achieved by carrying out more fatigue tests.

Table 4.4- Fatigue testing results.

Specimen	σ_{max} (MPa)	Δσ (MPa)	Freq. (Hz)	R	Testing Temperature (ºC)	Nº of cycles	Observations
L5 - 4	200	190	12	0.05	Room Temperature (23)	1 336	Valid (Fracture)
L5 - 7	150	142.5		0.05		8 014	
L5 - 8	100	95		0.05		193 726	
L5 - 9	75	71.2		0.05		2 000 000	Valid (No fracture)
L5 - 10	100	95		0.05		116 916	Valid (Fracture)
L4 - 1	90	85.5		0.05		2 000 000	Valid (No fracture)
L4 - 2	125	118.8		0.05		33 367	Valid (Fracture)
L4 - 3	100	95		0.05		137 661	
L4 - 4	99.5	94.5		0.05		288 334	
L4 - 5	100	50		0.5		2 000 000	Valid (No fracture)
L4 - 8	125	62.5		0.5		2 000 000	
L4 - 9	140	70		0.5		122 652	Valid (Fracture)
L4 - 10	140	70		0.5		313 228	
L3 - 1	135	67.5		0.5		175 537	
L3 - 2	130	65		0.5		2 000 000	Valid (No fracture)
L3 - 3	135	67.5		0.5		404 080	Valid (Fracture)
L3 - 4	95	90.3		0.05		2 000 000	Valid (No Fracture)
L3 - 5	120	114		0.05		7 771	Valid (Fracture)
L3 - 6	100	95		0.5		24 533	
L3 - 7	95	90.2		0.5		8 713	
L2 - 2	150	75	8	0.5	High Temperature (150)	49 343	
L2 - 3	150	142.5		0.05		6 907	
L2 - 4	125	118.8		0.05		20 494	
L2 - 5	125	62.5		0.5		106 322	
L2 - 7	100	95		0.05		348 542	
L2 - 10	100	50		0.5		360 950	
L7 - 2	90	85	10	0.05		2 000 000	Valid (No Fracture)
L7 - 4	95	90.3		0.05		2 000 000	
L7 - 5	110	104.5	8	0.05		121 855	Valid (Fracture)
L7 - 6	110	55		0.5		393 172	

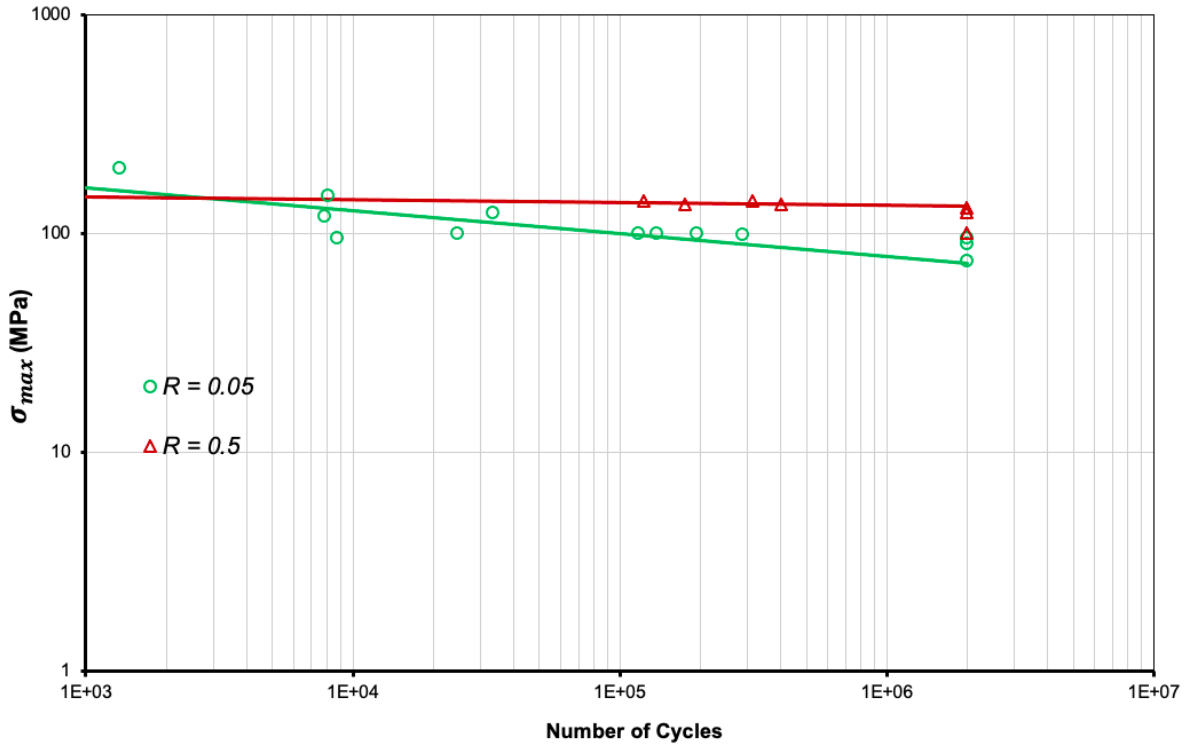

Figure 4.9- S-N curves obtained for the fatigue tests carried out at room temperature (23 ºC), considering the maximum stress applied during the fatigue tests.

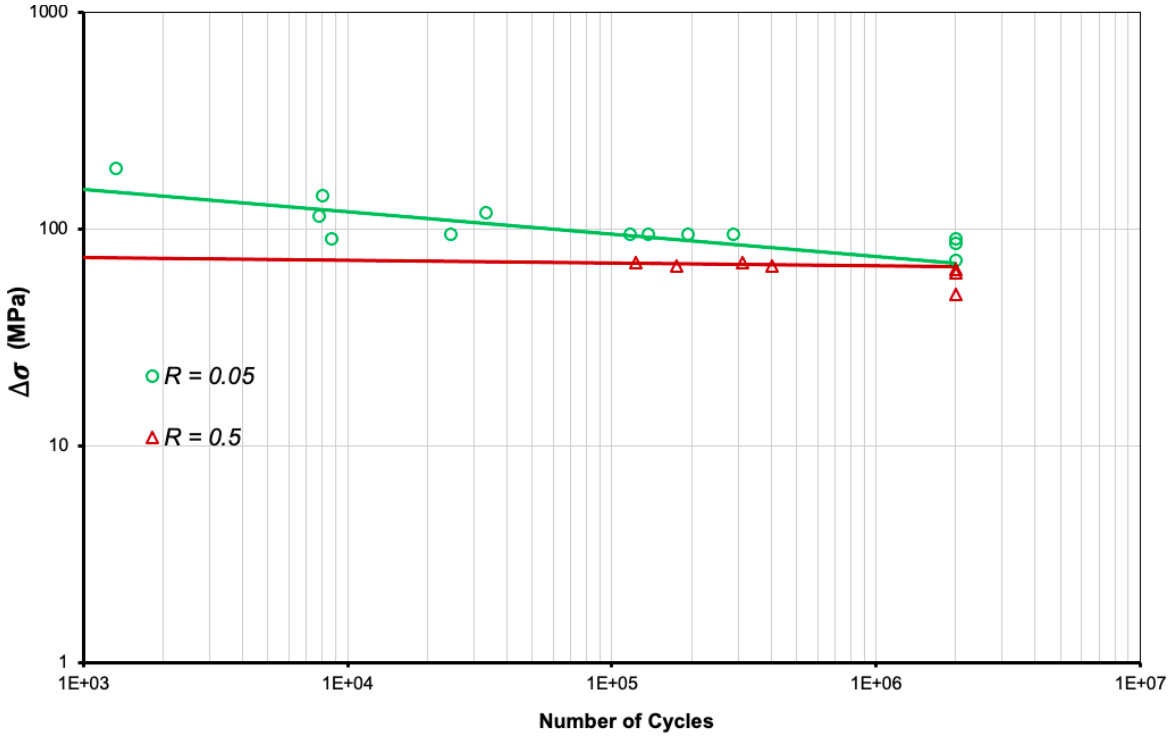

Figure 4.10- S-N curves obtained for the fatigue tests carried out at room temperature (23 ºC), considering the stress range applied during the fatigue tests.

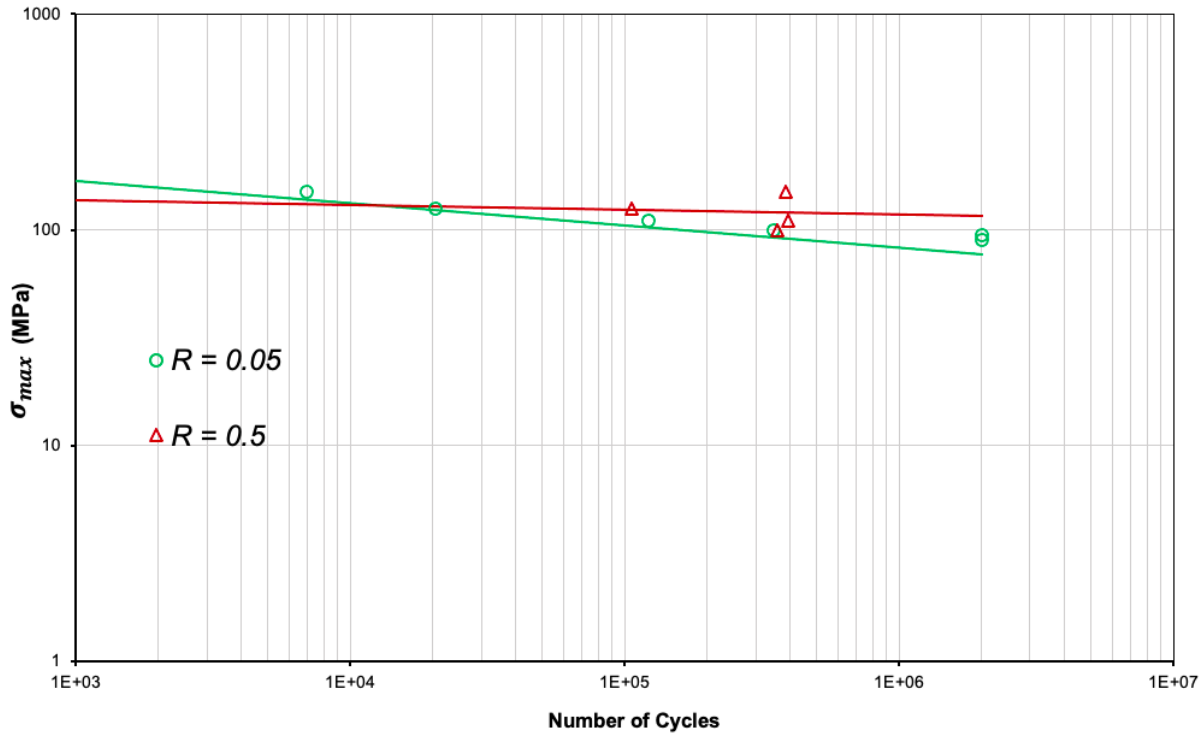

Figure 4.11- S-N curves obtained for the fatigue tests carried out at high temperature (150 ºC), considering the maximum stress applied during the fatigue tests.

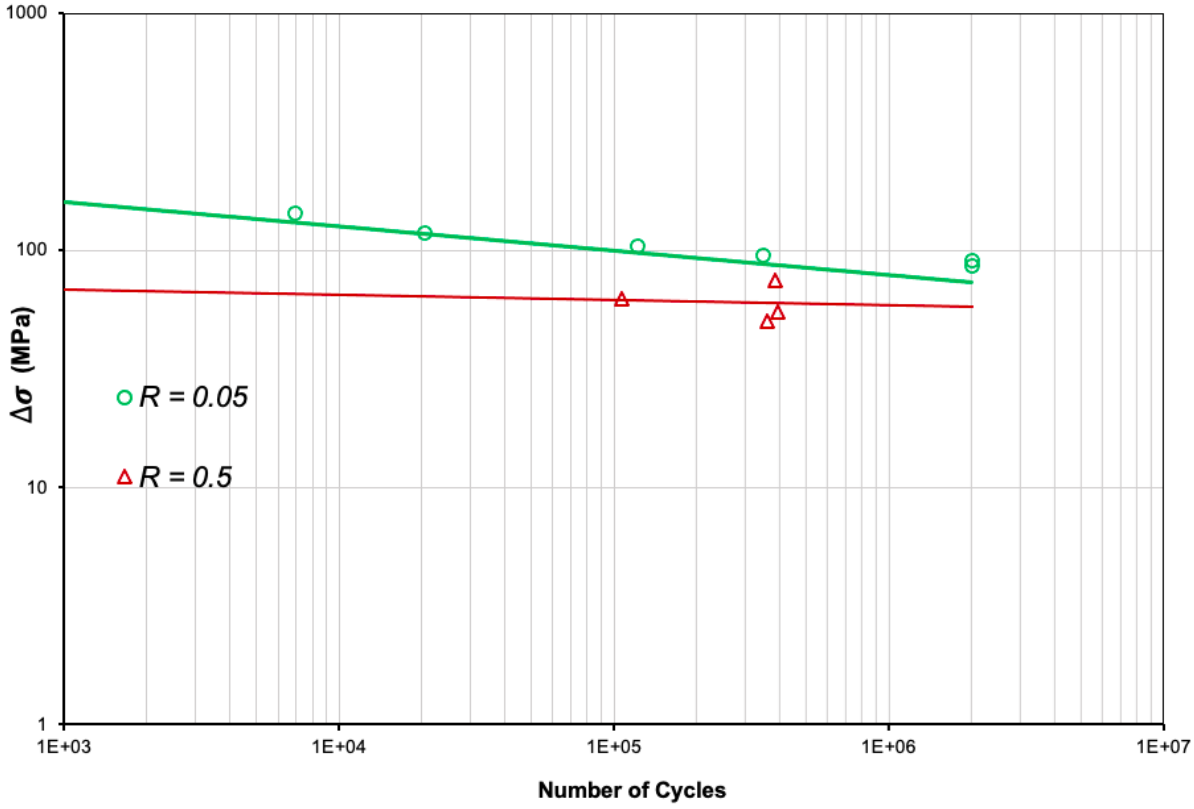

Figure 4.12- S-N curves obtained for the fatigue tests carried out at high temperature (150 ºC), considering the stress range applied during the fatigue tests.

Through the analysis of Table 4.4 and the S-N curves presented in Figures 4.9, 4.10, 4.11 and 4.12, it is possible to withdraw the following conclusions:

- When considering the maximum stress applied during the fatigue tests, the fatigue life of the specimens was found to be lower when the lowest stress ratio (R= 0.05) was applied. This means that for the same number of cycles, the maximum stress needed to cause failure in R= 0.05 conditions is lower comparatively to the one required for R= 0.5 conditions.

  Relatively to the stress range applied throughout the fatigue tests, the lowest stress ratio was found to result in a higher fatigue life of the specimens. This observation is in line with Figure 2.17, in which it is possible to see that for a certain stress amplitude, lower mean stresses require a higher number of cycles until failure.

  This trends were observed for both loading temperatures.

- Regarding the temperature effect over the fatigue life of the specimens, it is also easy to perceive the highly, negative impact of the use of 150 ºC as testing temperature, when the maximum stress applied during the tests was being considered.

  When the same stress ratio and maximum stress (or similar) were applied to the specimens at room temperature, fatigue failure occurred at a significantly higher number of cycles, comparatively to the ones obtained at 150 ºC.

  Such a trend was expected, taking into account the work developed by Resan et al. [49] and Tra et al. [50], whose works and results were discussed in the second chapter of this dissertation (see section 2.3.2. Fatigue Properties in FSW).

  As Tra et al. [50] reported, the fatigue crack growth rate increases as the fatigue testing temperature increases, resulting in a lower number of cycles required for failure to occur.

- The S-N curves that were obtained for the maximum stress applied in the execution of the fatigue tests are less spaced than the ones obtained when considering the stress range of those same tests. This means that the material was sensitive to the mean stress applied.

  This was observed for both loading temperatures.

4.6. Fatigue Fracture Surface Analysis

A visual analysis was conducted in the specimens that underwent fatigue testing and for which fracture occurred. This analysis was performed with the purpose of identifying the location, within the weld, where the fatigue crack nucleated, the type of fatigue crack present in each specimen and the direction along which the propagation process took place. These information is summarized in Table 4.7. Considering the number of specimens tested, this analysis is intended to be a representative one. Therefore, only one specimen from each different type of fracture surface observed is hereby presented, in Figure 4.13.

Table 4.5- Properties of the fatigue fracture surfaces obtained for the fatigue specimens.

Specimen	Fatigue fracture surface properties
L3 - 5, L3 - 6, L3 - 7, L4 - 3, L4 - 4, L4 - 9, L4 -10, L5 - 4, L5 - 8	Fracture occurred according to a 45º plane, relatively to the applied stress. Through type of crack with the nucleation process starting at the bottom surface of the specimen, at the root of the weld. For the L5-8 and L3-5 specimens, secondary cracking was observed.
L3 - 1, L4 - 2, L5 - 7, L2 - 2, L2 - 3, L2 - 4, L2 - 5, L2 - 10, L2 - 7, L7 - 2, L7 - 4, L7 - 5, L7 - 6	Fracture occurred according to a 90º plane, relatively to the applied stress. Semi-elliptical type of crack that nucleated at the bottom surface of the specimen, at the root of the weld. The crack then propagated to near the top surface of the weld.
L3 - 3	Fracture occurred according to a 90º plane, relatively to the applied stress. Corner type of crack that nucleated at the bottom surface of the specimen, at the root of the weld. The crack propagated to near the top surface of the weld.
L5 - 10	Fracture occurred according to a 45º and to a 90º plane, relatively to the applied stress. Semi-elliptical type of crack that nucleated at the bottom surface of the specimen, at the root of the weld. Secondary cracking was observed.

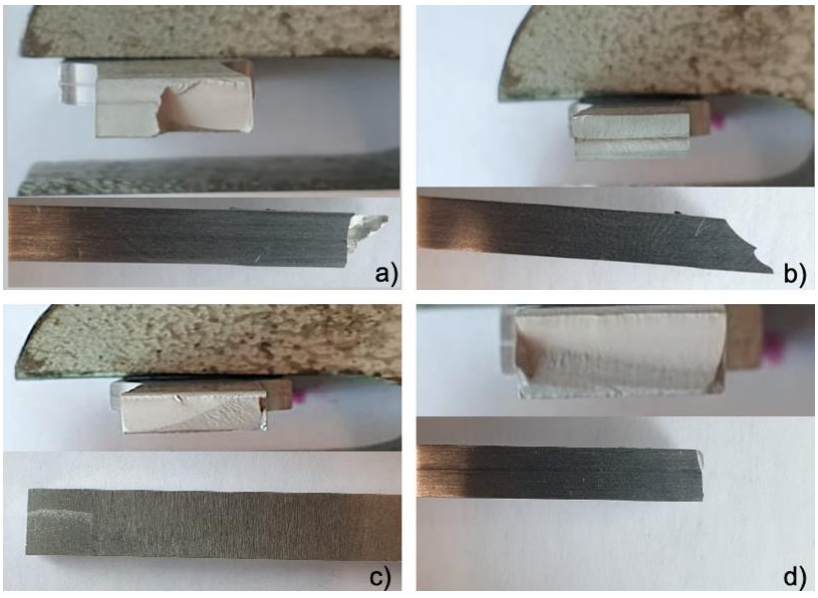

Figure 4.13- Fatigue fracture surface of the: a) L5-10, b) L3-5, c) L3-3, d) L3-1 specimen.

4.7. Fatigue Fracture Surface Characterization by SEM

The fatigue specimens that are presented in Figure 4.13 were posteriorly taken to the SEM with the purpose of identifying in more detail the morphology of the fatigue crack nucleation and propagation mechanism. The results obtained are shown trough Figure 4.14 to Figure 4.17.

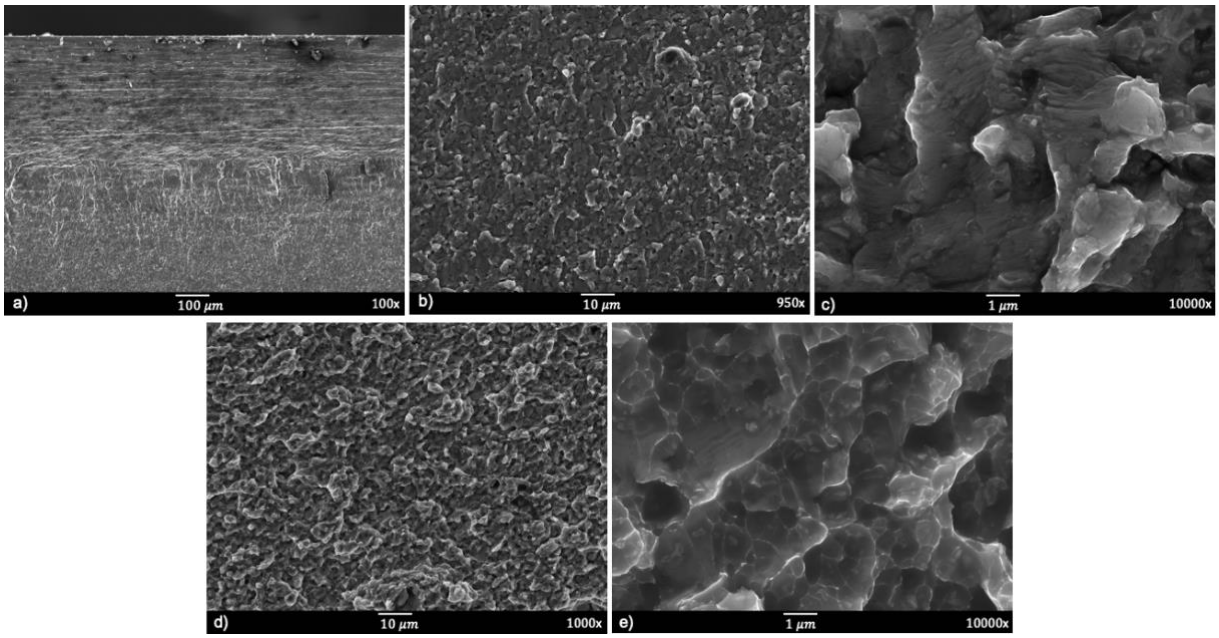

Figure 4.14- L3-1 fractographies: a) crack initiation region, b) crack propagation region, c) fatigue striations, d) final fracture region with visible dimples, e) detail of d).

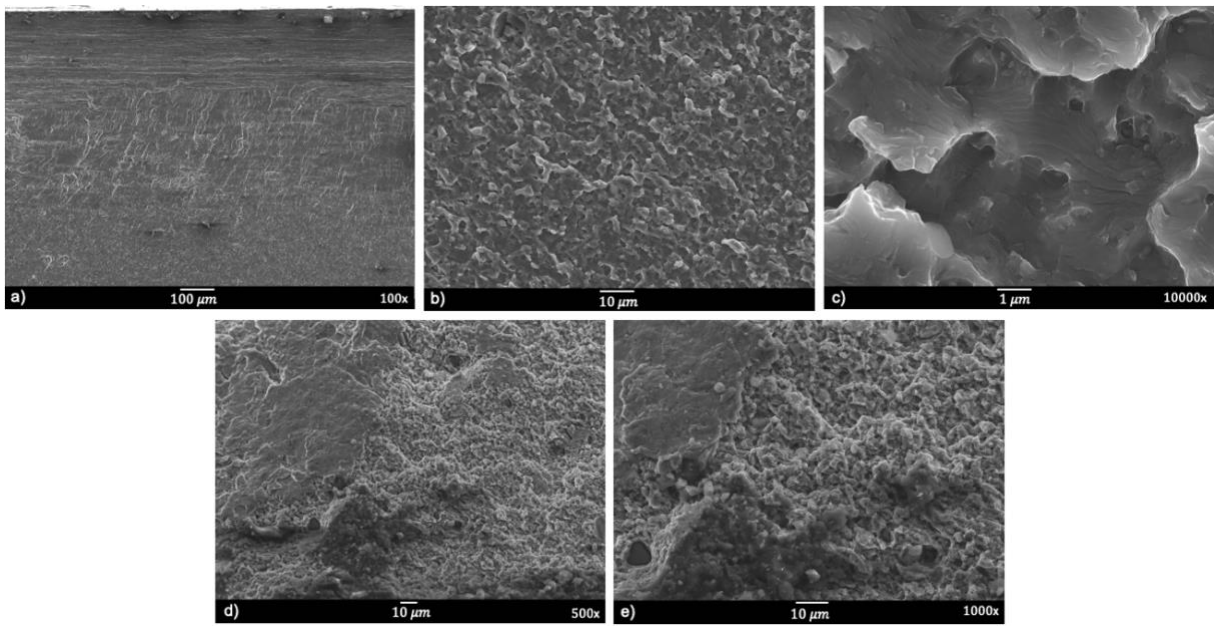

Figure 4.15- L3-3 fractographies. a) crack initiation region, b) crack propagation region, c) fatigue striations, d) final fracture region, e) detail of d).

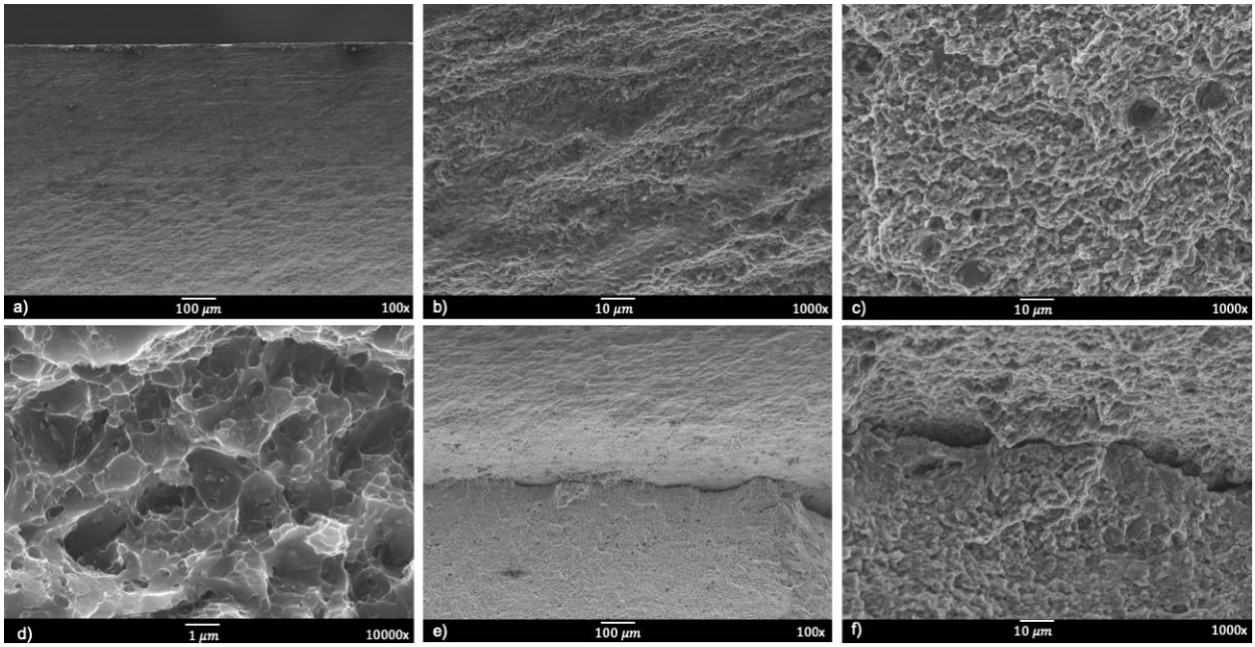

Figure 4.16- L3-5 fractographies. a) crack initiation region, b) final fracture region, c) final fracture regions showing dimples, d) detail of c), e) secondary cracking, f) detail of e).

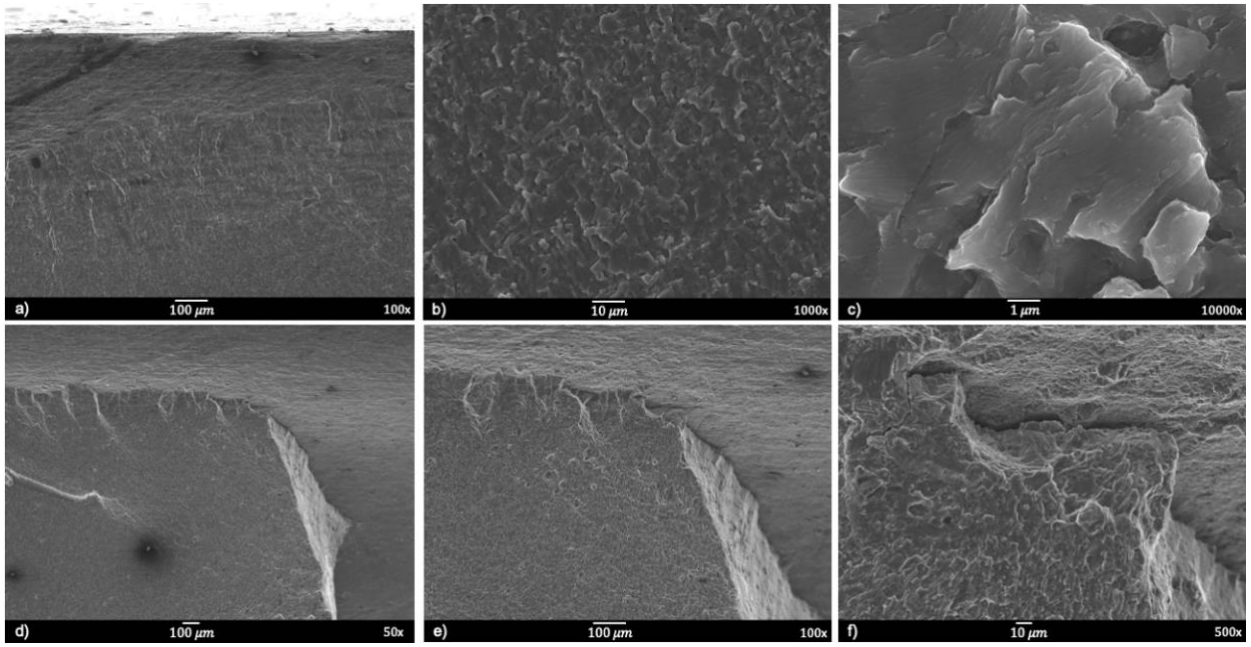

Figure 4.17- Figure 4.19- L5-10 fractographies: a) crack initiation region, b) crack propagation region, c) fatigue striations, d) secondary cracking), e) detail of d), f) detail of e).

From the results obtained by the analysis that was performed over the fatigue fracture surfaces, it is possible to see that the fatigue process took place in three distinct regions, with each region resulting from a different fatigue stage: i) crack initiation region, ii) crack propagation region,

illustrated by the presence of fatigue striations and iii) final fracture region, illustrated by the presence of dimples.

Crack initiation occurs, for all specimens, at the root of the weld. According to the work developed by other authors, in friction stir welds that are free of defects, the crack initiation process usually starts off at the top surface of the weld, from surface irregularities that could be a result of marks left by the FSW tool [48], [71]. Since, according to the non-destructive tests that were carried out, no welding defects were detected in the welds from which the fatigue specimens were manufactured from, a weaker zone at the root of the weld, that could have resulted from an improper/insufficient material mixing, could be the reason behind such an observation.

Although the fatigue crack nucleated at the root of the weld in all specimens, its propagation was found to occur along two possible directions (for the specimens tested at room temperature): according to a 45º or 90º plane, relatively to the applied stress. The latter was expected [41] and an effort was made in order to correlate the direction of the crack propagation and the stress range used during the fatigue tests.

From the analysis of Table 4.4, it is possible to conclude that, generally, lower stress ranges resulted in the fatigue crack propagating at 45º, which can be a result of the machine's lower clamp rotation combined with a possible misalignment of the fatigue specimens. This could also be the reason why for the L5-10 specimen, fracture occurred according to both a 45º and 90º plane relatively to the applied stress.

In order to avoid obtaining similar results for the fatigue tests carried out at high temperature, the fatigue testing equipment was slightly changed, with different clamps being used. The new clamps are shown in more detail in Figure 4.18.

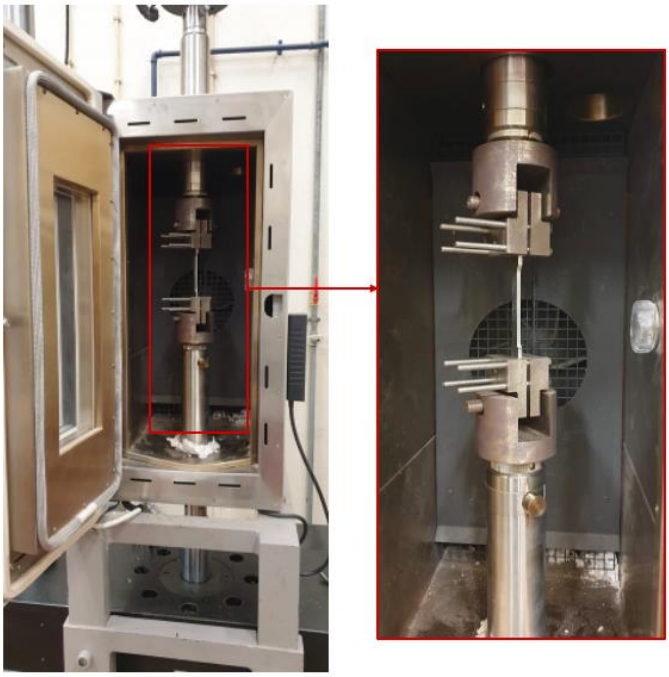

Figure 4.18- Setup used to perform the fatigue tests at 150 ºC.

The hydraulic clamps that were used in the fatigue tests carried out at room temperature were replaced by manual clamps. All specimens tested at high temperature fractured according to a 90º plane, relatively to the applied stress.

The process of secondary cracking was observed in 3 specimens: L3-5, L5-8 and L5-10 and is possible to visualize in the fractographies presented in Figure 4.16 and Figure 4.17.

The crack propagation process takes place after the crack attains a certain dimension (usually in the order of some grains size). The region through each the crack propagates was easily identified while analyzing the surfaces' fractographies, due to the presence of its most characteristic feature: striations. Fatigue striations are a result of the crack tip deformation during a complete load cycle. In fact, each striation results from a load cycle and marks the successive position of the front of the crack in the moment that the striation was formed. The spacing between each one of them corresponds to the crack growth during each load cycle. Striations are usually aligned perpendicularly to the crack propagation direction and invariably bowed towards that direction as well, since their growth is facilitated closer to the crack tip comparatively to the borders, where their growth is restrained (for example by grain boundaries).

The crack initiation and propagation regions combine to make up a smooth region in the fracture surface that has a silky and shiny appearance (easily perceived in Figure 4.13 c) and d)). Such an appearance is a result of the rubbing of the crack surfaces during its propagation process. As for the final region of the fracture surfaces, where the final fracture took place, it is characterized by a darker region with a more coarse and irregular appearance. This final fracture takes place when that region, the remaining cross-sectional area of the specimen, is not capable of withstanding the stress that is being applied. In this region, the mechanisms that led to the crack propagation are progressively replaced by static fracture mechanisms. In this stage of the fatigue process, the crack growth rate increases exponentially, and the specimen's fracture becomes unpredictable.

As a result of both the microstructure of the specimens and the alternated stress applied to them during fatigue testing, a final ductile fracture is obtained.
Such a type of fracture is revealed by the existence of small voids, depressions - dimples - that are easily depicted through the analysis of the fractographies obtained by the SEM**.**

Chapter 5

Conclusions

Along the current chapter of the dissertation, the main conclusions that can be gathered from the work that was carried out within the scope of this dissertation are presented and possible future investigations and developments are outlined.

5.1. Achievements

The conclusions that arose from the work that was developed are hereby presented, according to the different topics covered.

Hardness testing

- Both samples (taken from the L1 and D13 weld) presented a W-shaped hardness profile, which is characteristic of friction stir welds of this type of aluminum alloys, with values that were inferior to the one presented by the base material, which was also determined during the hardness testing procedure (approximately 193 HV).
- The SZ region presents a plateau along which the hardness values remain more or less constant, which is a result of the homogeneous microstructure found in this region, that was by its turn observed during the metallographic characterization of the welds.
- For both the samples that were analyzed, the lowest hardness values were registered at the interface between the TMAZ and HAZ, in most of the cases at the advancing side of the weld, with the lowest value observed being in the D13 sample: 119 HV.
- The effect of the Kissing Bond defect, that was identified in the D13 weld, over the hardness profile, was not perceptible.

Uniaxial quasi-static tensile testing

- Three specimens were selected to undergo uniaxial quasi-static tensile tests. Regarding their yield strength, it was assumed to be around 305 MPa taking into account that from that point onwards a change in the slope of the Load-Displacement curves was observed. This value corresponds to a decrease of approximately 39% comparatively to the yield strength of the base material (503 MPa).

- As for the UTS, similar values were obtained for the 3 specimens, with an average of 365 MPa (standard deviation of 11.3 MPa), which corresponds to a joint efficiency of 63%.
- One specimen fractured according to a 45º plane and the other two according to a 90º plane, with the fracture initiating, in all of them, at the root of the weld. Such an observation was attributed to the possible presence of a weaker zone in this region of the weld, with its extension dictating the direction along which the fracture evolved along the specimens.

Fatigue testing

- When considering the maximum stress applied, the fatigue life of the AA7075-T651 friction stir welds was found be lower when the lowest stress ratio was applied (R= 0.05) for both loading temperatures. For the stress range, the contrary was also found to be true: R= 0.5 resulted in a lower fatigue life of the specimens.
- When considering the maximum stress applied during the fatigue tests, it was possible to verify that the fatigue life of the specimens tested at the higher loading temperature (150 ºC) was significantly lower when compared to fatigue tests conducted at a similar maximum stress, at the same stress ratio, at room temperature (23 ºC).
  Such a phenomenon was attributed to an increase in the fatigue crack growth rate induced by the higher loading temperature.
- The material was found to be sensitive to the mean stress applied during the fatigue tests.
- Through the analysis of the fatigue fracture surfaces it was possible to observe that for all the specimens, fatigue failure occurred along 3 different regions: initiation, propagation and final fracture region.
- For all the specimens, the fatigue crack initiation process took place at the root of the weld with most of them presenting a through type of crack.
- Secondary cracking was observed for 3 specimens.
- It was observed that the fatigue crack propagated according to a 45º plane or to a 90º plane, relatively to the applied stress, in the specimens tested at room temperature (for one specimen, L5-10, the crack propagated in both directions).
  This was attributed to a possible movement of the fatigue machine's lower clamp combined with a possible misalignment of the fatigue specimens.
  Therefore, for the fatigue tests carried out at high temperature, different clamps were used, and all the specimens fractured at 90º.

5.2. Future Developments

Some future work proposals, that will enhance the work that was developed and presented throughout the previous chapters of this dissertation, are hereby presented:

- A preliminary step would be employing the Taguchi method to ensure that optimal welding parameters are being used in order to produce the welds from which tensile and fatigue specimens are manufactured from, considering both the material used, AA7075-T61, and the plates thickness: 4 mm.
- Measure the temperature distribution along the different regions of the weld and correlate the results obtained with the resultant microstructure of the welds.
- Evaluate the presence and degree of residual stresses in the welds and correlate the results obtained through the execution of the mechanical tests with the residual stresses measured.
- The non-destructive tests should be carried out in a more parameterized manner, using different inspection depths, in order to assess the most appropriate one, considering both the material used and the thickness of the welded plates.
  In this way, it could be possible to further support the observations resulting from the diverse mechanical tests to be carried out.
- Perform tensile tests under different loading temperatures.
- More fatigue tests should be carried out in order to confirm the results obtained in the experimental work developed for this thesis. This would also allow to obtain S-N curves with a better correlation coefficient relatively to the points of the S-N diagram.
- Carry out fatigue tests under different loading and temperature conditions than the ones used throughout this thesis.
- Evaluate the effect that post-welding treatments would have in the mechanical properties that were analyzed throughout this thesis.

References

[1] European Commission, “The European Green Deal, COM/2019/640,” Brussels, 2019.

[2] European Comission, “Horizon Europe,” [Online]. Available: https://ec.europa.eu/info/research-and-innovation/funding/fundingopportunities/funding-programmes-and-open-calls/horizon-europe_en. [Accessed October 2021].

[3] G.-Q. Sun, X. Wei, D.-G. Shang, S. Chen, L.-C. Long e X. Han, “Tensile and Fatigue Analysis Based on Microstructure and Strain Distribution for 7075 Aluminum FSW Joints,” *Metals,* vol. 10, nº 12, 2021.

[4] S. Epstein, “Human exposure to aluminum,” *Environmental Geochemistry and Health,* vol. 12, pp. 65-70, 1990.

[5] H. Kvande, “Two hundred years of aluminum ... or is it aluminium?,” *JOM: The journal of the Minerals, Metals & Materials Society,* vol. 60, nº 8, pp. 23-24, 2008.

[6] N. N. Gow e G. P. Lozej, “Bauxite,” *Geoscience Canada,* vol. 20, nº 1, 1993.

[7] J. R. Davis, Ed., ASM Specialty Handbook: Aluminum and Aluminum Alloys, Materials Park, OH: ASM International, 1993.

[8] R. H. G. Silva, J. C. Dutra e R. Gohr Jr, “Scientific and technological fundamentals for the development of the controlled short circuiting MIG/MAG welding process (CCC)-A literature review. Part 1 of 3: History and wire-electrode melting aspects,” *Welding International,* vol. 22, nº 12, pp. 847-852, 2008.

[9] S. A. Akinlabi e E. T. Akinlabi, “Friction Stir Welding Process: A Green Technology,” *World Academy of Science, Engineering and Technology,* vol. 6, nº 11, pp. 2514 - 2516, 2012.

[10] F. Hussain, S. Abdullah e M. Z. Nuawi, “Effect of temperature on fatigue life behaviour of aluminium alloy AA6061 using analytical approach,” *Journal of Mechanical Engineering and Sciences,* vol. 10, nº 3, 2016.

[11] J. D. Backer, “Feedback Control of Robotic Friction Stir Welding, PhD Dissertation,” University West, Trollhättan, 2014.

[12] R. S. Mishra e Z. Y. Ma, “Friction stir welding and processing,” *Materials Science and Engineering: R: Reports,* vol. 50, nº 1-2, pp. 1-78, 2005.

[13] S. Verma, Meenu e J. P. Misra, “Study on temperature distribution during Friction Stir Welding of 6082 aluminum alloy,” *Materials Today: Proceedings,* vol. 4, nº 2, pp. 1350-1356, 2017.

[14] W. Tang, X. Guo, J. C. McClure e L. E. Murr, “Heat Input and Temperature Distribution in Friction Stir Welding,” *Journal of Materials Processing & Manufacturing Science,* vol. 7, nº 2, pp. 163-172, 1998.

[15] T. Sakthivel, G. S. Sengar e J. Mukhopadhyay, “Effect of welding speed on micro structure and mechanical properties of friction stir welded aluminium,” *International journal of Advanced Manufacturing Technology,* vol. 43, 2009.

[16] M. Ericsson, e R. Sandström, “Influence of welding speed on the fatigue of friction stir welds, and comparison with MIG and TIG,” *International Journal of Fatigue,* vol. 25, 2003.

[17] M. A. Pasha, R. R. Pinninti, I. A. Khan e P. Laxminarayana, “Influence of process and tool parameters on Friction Stir Welding,” *International Journal of Applied Engineering and Technology,* vol. 4, nº 3, pp. 54-69, 2014.

[18] P. M. Mashinini, “Process window for friction stir welding of 3 mm titanium (Ti-6AI-4V),” MSc Dissertation, 2010.

[19] A. Garg e M. Raturi, “Influence of additional heating in friction stir welding of dissimilar aluminum alloys with different tool pin profiles,” *The International Journal of Advanced Manufacturing,* vol. 105, 2019.

[20] N. Dialami, M. Cervera e M. Chiumenti, “Effect of the Tool Tilt Angle on the Heat Generation and the Material Flow in Friction Stir Welding,” *Metals - Open Access Metallurgy Journal,* vol. 9, nº 28, 2018.

[21] L. Dumpala e D. Lokanadham, “Low Cost Friction Stir Welding of Aluminium Nanocomposite – A Review,” *Procedia Materials Science,* vol. 6, pp. 1761-1769, 2014.

[22] K. N. Krishnan, “On the formation of onion rings in friction stir welds,” *Materials Science and Engineering: A,* vol. 327, nº 2, pp. 246-251, 2002.

[23] O. S. Salih, D. G. McCartney e H. Ou, “A review of friction stir welding of aluminium matrix composites,” *Materials & Design,* vol. 86, pp. 61-71, 2015.

[24] E. Ahmed, H. Ammar, M. E.-S. Seleman, S. Ataya e M. Ahmed, “Friction stir welding of similar and dissimilar AA7075 and AA5083,” *Journal of Materials Processing Technology,* vol. 242, pp. 77-91, 2017.

[25] P. Vilaça, “Fundamentos do processo de soldadura por fricção linear, análise experimental e modelação analítica,,” PhD Dissertation, IST, Lisbon, 2003.

[26] J. S. Leon, G. Bharathiraja e V. Jayakumar, “A review on Friction Stir Welding in Aluminium Alloys,” em *IOP Conference Series: Materials Science and Engineering*, 2020, Tamilnadu.

[27] H. Taheri, M. Kilpatrick, M. Norvalls, W. J. Harper, L. W. Koester, T. Bigelow e L. J. Bond, “Investigation of Nondestructive Testing Methods for Friction Stir Welding,” *Metals,* vol. 9, nº 6, 2019.

[28] M. M. Shahri, “Fatigue Assessment of Friction Stir Welded Joints in Aluminium Profiles,” PhD Thesis, KTH, Stockholm, 2010.

[29] N. Z. Khan, Z. A. Khan, A. N. Siddiquee, A. M. Al-Ahmari e M. H. Abidi, “Analysis of defects in clean fabrication process of friction stir welding,” *Transactions of Nonferrous Metals Society of China,* vol. 27, nº 7, pp. 1507-1516, 2018.

[30] M. Ericsson, “Fatigue Strength of Friction Stir Welded Joints in Aluminium,” PhD Dissertation, KTH, Stockholm, 2005.

[31] A. J. Leonard e S. A. Lockyer, “Flaws in friction stir welds,” em *4th International Symposium on Friction Stir Welding*, Park City, Utah, 2003.

[32] C. Zhou, X. Yang e G. Luan, “Fatigue properties of friction stir welds in Al 5083 alloy,” *Scripta Materialia,* vol. 53, nº 10, pp. 1187-1191, 2005.

[33] P. Podržaj e D. Klobčar , “Welding defects at friction stir welding,” *Metalurgija -Sisak then Zagreb- (METALURGIJA),* vol. 54, nº 2, pp. 387-389, 2015.

[34] M. S. Sidhu e . S. S. Chatha, “Friction Stir Welding – Process and its Variables: A Review,” *International Journal of Emerging Technology and Advanced Engineering,* vol. 2, nº 12, 2012.

[35] SpaceX, "Falcon User's Guide," Space X, September 2021. [Online]. Available: https://www.spacex.com/media/falcon-users-guide-2021-09.pdf. [Accessed October 2021].

[36] S. Kallee, “FSW and FSSW in the Automotive Industry,” AluStir, February 2013. [Online]. Available: https://www.alustir.com/english/fsw-automotive-industry/. [Accessed February 2021].

[37] *Soudage et Techniques Connexes,* vol. 67, nº 05/06, pp. 12-14, May/June 2013.

[38] R. Shimpi, P. K. Loharkar e R. A. Gite, “Friction stir welding parameters and application: A review,” *Materials Today: Proceedings,* vol. 19, pp. 361-365, 2019.

[39] R. Jain, K. Kumari, R. K. Kesharwani, S. Kumar, S. K. Pa, S. B. Singh, S. K. Panda e A. K. Samantaray, Modern Manufacturing Engineering, J. Davim, Ed., Springer, Cham, 2015, pp. 179-229.

[40] T. Tinga, Principle of Loads af Failure Mechanisms: Application in Maintenance, Reliability and Design, Springer, 2013.

[41] R. Budynas e K. Nisbett , Shigley's Mechanical Engineering Design, 10th edition, McGraw-Hill Education, 2014.

[42] G. Lesiuk, “Application of a New, Energy-Based ΔS* Crack Driving Force for Fatigue Crack Growth Rate Description,” *Materials,* vol. 9, nº 3, 2019.

[43] K. A. Zakaria, S. Abdullah e M. Ghazali, “A Review of the Loading Sequence Effects on the Fatigue Life Behaviour of Metallic Materials,” *Journal of Engineering Science and Technology Review,* vol. 9, nº 5, pp. 189-200, 2016.

[44] R. John, K. Jata e K. Sadananda, “Residual stress effects on near-threshold fatigue crack growth in friction stir welds in aerospace alloys,” *International Journal of Fatigue,* vol. 25, nº 9-11, pp. 939-948, 2003.

[45] M. Peel, A. Steuwer, M. Preuss e P. J. Withers, “Microstructure, mechanical properties and residual stresses as a function of welding speed in aluminium AA5083 friction stir welds,” *Acta Materialia,* vol. 51, nº 16, pp. 4791-4801, 2003.

[46] S. Li, “Aluminum Friction Stir Welding Head Fatigue Craek Growth Rate PILOT Study,” Lanzhou University of Technology, Lanzhou, 2008.

[47] G. Pouget e A. Reynolds, “Residual stress and microstructure effects on fatigue crack growth in AA2050 friction stir welds,” *International Journal of Fatigue,* vol. 30, nº 3, pp. 463-472, 2008.

[48] S. Lomolino, R. Tovo e J. d. Santos, “On the fatigue behaviour and design curves of friction stir butt-welded Al alloys,” *International Journal of Fatigue,* vol. 27, nº 3, pp. 305-316, 2005.

[49] K. Resan, M. Al-Waily, A. A. Alasadi e M. J. Jweeg, “Influence of Temperature on Fatigue Life for Friction Stir Welding of Aluminum Alloy Materials,” *International Journal of Mechanical & Mechatronics Engineering,* vol. 18, 2018.

[50] T. H. Tra, M. Okazaki e K. Suzuki, “Fatigue crack propagation behavior in friction stir welding of AA6063-T5: Roles of residual stress and microstructure,” *International Journal of Fatigue,* vol. 43, pp. 23-29, 2012.

[51] G. Bussu e P. Irving, “Proceedings of the First International Symposium on Friction Stir Welding,” Thousand Oaks, CA, USA, June 14-16, 1999.

[52] L. Magnusson e L. Kallman, “Proceedings of the Second International Symposium on Friction Stir Welding,” Gothenburg, Sweden, 2000.

[53] C. I. S. Vidal, “Assessment of Improvement Techniques Effect on Fatigue Behaviour of Friction Stir Welded Aerospace Aluminium Alloys,” MSc Thesis, Lisbon, 2009.

[54] M. N. James, D. G. Hattingh e G. R. Bradley, “Weld tool travel speed effects on fatigue life of friction stir welds in 5083 aluminium,” *International Journal of Fatigue,* vol. 25, 2003.

[55] M. Kadlec, R. Ruzek e L. Novakova, “Mechanical behaviour of AA 7475 friction stir welds with the kissing bond defect,” *International Journal of Fatigue,* vol. 74, pp. 7-19, 2015.

[56] T. L. Dickerson e J. Przydatek, “Fatigue of friction stir welds in aluminium alloys that contain root flaws,” *International Journal of Fatigue,* vol. 25, nº 12, pp. 1399-1409, 2003.

[57] S. Kahl e W. Osikowicz , “Composite Aluminum-Copper Sheet Material by Friction Stir Welding and Cold Rolling,” *Journal of Materials Engineering and Performance,* vol. 22, 2013.

[58] H. Hori, S. Makita e H. Hino, “Proceedings of the First International Symposium on Friction Stir Welding,” Thousand Oaks, CA, USA, June 14-16, 1999.

[59] MatWeb, "Aluminum 7075-T6; 7075-T651," [Online]. Available: http://www.matweb.com/search/DataSheet.aspx?MatGUID=4f19a42be94546b686bbf43f79c51b7d&ckck=1. [Accessed October 2021].

[60] S. R. Tadivaka, G. M. Reddy e S. R. K. Rao, “Microstructure and mechanical properties of friction stir welded AA7075-T651 aluminum alloy thick plates,” *Transactions of Nonferrous Metals Society of China,* vol. 25, nº 6, pp. 1770-1778, 2015.

[61] V. Balasubramanian, D. Kanagarajan e P. Sivaraj, “Effect of post weld heat treatment on tensile properties and microstructure characteristics of friction stir welded armour grade AA7075-T651 aluminium alloy,” *Defence Technology,* vol. 10, nº 1, pp. 1-8, 2014.

[62] P. Vilaça e T. Santos, “Ferramenta Não Consumível Modular Ajustável e Refrigerável para Soldadura e Processamento por Fricção Linear”. Portugal Patente 104072, 26 May 2008.

[63] G. L. Sorger, J. P. Oliveira, P. L. Inácio, N. Enzinger, P. Vilaça, T. G. Santos e R. M. Miranda, “Non-destructive microstructural analysis by electrical conductivity: Comparison with hardness measurements in different materials,” *Journal of Materials Science & Technology,* vol. 35, nº 3, pp. 360-368, 2019.

[64] B. Dalai, M. A. Moretti, P. Åkerström, C. Arvieu, D. Jacquin e L.-E. Lindgren, “Mechanical behavior and microstructure evolution during deformation of AA7075-T651,” *Materials Science & Engineering A,* vol. 822, 2021.

[65] S. A. Khodir, T. Shibayanagi e M. Naka, “Microstructure and Mechanical Properties of Friction Stir Welded AA2024-T3 Aluminum Alloy,” *Materials Transactions,* vol. 47, nº 1, pp. 185-193, 2006.

[66] B. Çevik, Y. Ozcatalbas e B. Gülenç, “Friction Stir Welding of 7075-T651 Aluminium Alloy,” *Praktische Metallographie,* vol. 53, nº 1, pp. 6-23, 2016.

[67] S. B. Pankade, P. M. Ambad, R. Wahane e C. L. Gogte, “Effect of the Post-weld Heat Treatments on Mechanical and Corrosion Properties of Friction Stir-Welded AA 7075-T6 Aluminium Alloy,” em *Strengthening and Joining by Plastic Deformation*, Springer Singapore, 2019.

[68] R. Selvarajan e V. Balasubramanian , “Correlation between weld nugget grain size, weld nugget hardness and tensile strength of friction stir welded commercial grade aluminium alloy joints,” *Materials and Design (MATER DESIGN),* nº 34, pp. 242-251, 2012.

[69] Y. Tan, M. Ma, S. Xiang, R. Fu, W. C. Liu, J. X. Zhang e X. M. Wang, “A study on microstructure and mechanical properties of AA 3003 aluminum alloy joints by underwater friction stir welding,” *Materials Characterization (MATER CHARACT),* nº 127, pp. 41-52, 2017.

[70] V. M. Linton e M. I. Ripley, “Influence of time on residual stresses in friction stir welds in agehardenable 7xxx aluminium alloys,” *Acta Materialia,* vol. 56, nº 16, pp. 4319-4327, 2008.

[71] H. Li, J. Gao e Q. Li , “Fatigue of Friction Stir Welded Aluminum Alloy Joints: A Review,” *Applied Sciences,* vol. 8, nº 12, 2018.

[72] J. P. Oliveira, P. L. Inácio, N. Enzinger, P. Vilaça, R. M. M. Miranda e T. J. G. dos Santos, “Non-destructive microstructural analysis by electrical conductivity: Comparison with hardness measurements in different materials,” *Journal of Materials Science and Technology,* vol. 35, nº 3, pp. 360-368, 2019.